Spatially and temporally resolved spectro-electrochemical analysis of electrochromic WO$_3$ electrodes

Contents

Acknowledgement

Mein besonderer Dank gilt

- meinem Doktorvater, Prof. Dr. Peter J. Klar. Für die Bereitschaft mich als Teilchenphysikerin in seine Arbeitsgruppe *Mikro- und Nanostrukturphysik* aufzunehmen. Und für die sehr gute und instensive Betreuung. Danke, dass du dir für deine Doktorkinder stets Zeit nimmst, selbst wenn du selbst bis zum Hals in Arbeit steckst.

- Prof. Dr. Jürgen Janek für die Bereitstellung seiner sehr gut ausgestatteten Labore, ohne die ein Großteil meiner Arbeit nicht möglich gewesen wäre. Für die produktiven Diskussionen, die uns Physikern die Elektrochemie immer ein Stück näher brachte. Und für die Erstellung des Zweitgutachtens.

- meinen Eltern, Nermin und Antonius, für die emotionale und finanzielle Unterstützung meines Studiums. Für die Unterstützung etlicher Praktika und Auslandsaufenthalte. Ihr habt mich stets ermutigt und nie zurückgehalten.

- meinem liebsten Pascal, dafür dass du immer für mich da bist. Für die inspirierenden chemisch-physikalischen Diskussionen und das Korrekturlesen meiner Arbeit.

- Matthias T. Elm für die inspirierenden Diskussionen.

- Thomas Leichtweiss, Sebastian Wenzel und Dominik Krüger für die Durchführung der XPS Messungen und Auswertungen

- Dominik Weber für die Dürchführung der XRD Messungen und Verfeinerung

- meinem sehr guten Freund, Julian Benz. Bei Problemen bist du für alle aus der Arbeitsgruppe die erste Anlaufstelle, weil du einfach alles kannst und auch immer bereit bist zu helfen. Durch dich hatte ich während meiner Doktorandenzeit stets einen Freund an meiner Seite.

- Simon Burkhardt, dessen Betreuung mir große Freude bereitet hat und im Endeffekt nicht nur mehr Arbeit bedeutete, sondern auch Unterstützung im Labor. Für die Weiterführung meines Forschungsthemas und die Erarbeitung einer Analysemethode zur Bestimmung von Diffusionskoeffizienten in kristallinem WO_3.

Abstract

An experimental setup is presented, which provides the opportunity to perform optical transmission analysis during electrochemical ion insertion into electrochromic materials, such as WO_3, with a time resolution on the second scale and local information on the micrometer scale. To conduct the experiments, WO_3 thin film electrodes were synthesized by various methods and lithographically micro structured. WO_3 was analyzed with respect of two main types of electrochemical experiments: (1) time resolved in situ transmission experiments during electrochemical ion insertion/extraction and (2) spatially and time resolved transmission experiments for the visualization and quantification of diffusion in WO_3.

(1) The correlation between the oxidation states of tungsten and the coloration efficiency of nanocrystalline WO_3 was analyzed and a two-step mechanism for the coloration process is proposed. For this the lithium inserted WO_3 electrodes were additionally investigated by XRD and XPS. During coloration tungsten is electrochemically reduced, and the formation of W^{5+} was found in the first step. However, only the formation of W^{4+}, which takes place in the second step (at lower electrode potentials), comes along with the main coloration. XRD results show that after the formation of W^{4+}, Li_xWO_3 exhibits a cubic crystal structure instead of the initial tetragonal structure.

(2) By patterning a transparent layer deposited on top of the WO_3 thin film, local insertion of hydrogen into the thin film could be achieved and ion transport in the plane of the WO_3 film could be visualized. The obtained temporal and spatial dependence of the observed coloration of WO_3 was described by a simple 1D diffusion model. A diffusion coefficient for hydrogen in amorphous WO_3 thin films was determined with a value of $D = 1.3 \cdot 10^{-10}\,\mathrm{cm^2/s}$.

Es wird ein experimenteller Aufbau vorgestellt, welcher Transmissionsuntersuchungen während elektrochemischer Ioneninsertion in elektrochrome Materialien, wie WO_3, mit einer Zeitauflösung im Sekunden-Bereich und einer Ortsauflösung im Mikrometer-Bereich zulässt. Um die Experimente durchführen zu können, wurden WO_3 Dünnfilmelektroden mittels verschiedener Methoden hergestellt und lithografisch mikrostrukturiert. Diese Dünnfilm-Elektroden wurden in Hinblick auf zwei Hauptexperimente untersucht: (1) zeitaufgelöste in situ Transmissionsexperimente während Ioneninsertion bzw. -extraktion und (2) orts- und zeitaufgelöste Transmissionsexperimente für die Visualisierung und Quantifizierung der Diffusion in WO_3.

(1) Die Korrelation zwischen den Oxidationszuständen von Wolfram und der Verfärbungseffizienz von nanokristallinem WO_3 wurde untersucht und ergab, dass der Verfärbungsprozess einem zweistufigem Mechanismus unterliegt. Dazu wurden die insertierten WO_3 Proben zusätzlich mittels XRD und XPS untersucht. Während der Verfärbung wird Wolfram W^{6+} elektrochemisch reduziert und die Bildung von W^{5+} konnte der ersten Stufe zugeordnet werden. Jedoch trägt die Bildung von W^{4+}, welches während der zweiten Stufe beobachtet wird (bei niedrigeren Elektrodenpotenzialen), zur Hauptverfärbung von WO_3 bei. XRD Messungen ergaben zudem, dass Li_xWO_3 nach der Bildung von W^{4+} eine kubische statt der ursprünglichen tetragonalen Struktur aufzeigt.

(2) Durch das Strukturieren einer durchsichtigen, auf dem WO_3 Dünnfilm aufgebrachten, teilweise ionenblockierende Schicht konnte der Ionentranport der insertierten Spezies in der Ebene des Dünnfilms visualisiert werden. Die somit ermittelte zeit- und ortsabhängige Verfärbung von WO_3 wurde mit einem einfachen 1D Modell beschrieben. Und es wurde ein Diffusionskoeffizient von Wasserstoff in amorphem WO_3 von $D = 1.3 \cdot 10^{-10}\,\mathrm{cm^2/s}$ ermittelt.

Introduction

Electrochromism is the property of a material/compound to reversibly change its color by electrochemical reduction or oxidation [1, 2, 3]. Studies of electrochromic materials were first published by Deb in 1969 [4] and reports on their application as energy efficient fenestration, often referred to as "smart windows", for buildings followed in 1984 [5, 6]. Since then electrochromism has been intensively investigated [2, 7, 8].

Electrochromic materials are promising for a wide spectrum of applications, such as information displays, mirrors with variable specular reflectance, smart windows and variable emittance surfaces [9]. Tungsten trioxide (WO_3) in particular is studied in more detail than any other chromogenic material for several reasons: it exhibits thermochromic, photochromic, gasochromic as well as electrochromic characteristics and is thus the most relevant material for chromogenic devices [10, 11, 12]. Other chromogenic oxides, such as MoO_3, are similar in their properties, so that WO_3 represents an adequate model system [2]. Due to the variety of its chromogenic properties, WO_3 is ideal for examining the coloration processes. However, details of the coloration mechanisms are still controversially discussed and a unified model is not established yet.

When studying literature of electrochromic WO_3 one notices that there are only a few publications that consider both, the physical and electrochemical properties of the system, equally. Either a physical experiment, i.e. analyzing the optical properties, is presented, and the electrochemical aspects are neglected, or electrochemical measurements are conducted, considering mainly the ion insertion/extraction and the electric response, while disregarding changes in the material's physical (optical, electronic, structural) properties. Usually only the final state, after complete coloration or bleaching, is studied in detail yielding information about transmission or electrode potential of the thin film. Hence, in situ experiments of the coloration and bleaching process itself, yielding information about the variation of the physical and the electrochemical properties are desirable and will yield additional insight into the microscopic coloration mechanism of WO_3 thin films.

The aim of this Ph.D. project was to design and build an experimental setup, which is suitable for in situ transmission experiments and allows one to address electrochemical and physical aspects simultaneously. It should provide the opportunity to perform optical transmission analysis during electrochemical ion insertion

into WO_3, with a time resolution of seconds. In addition, spatial information on the micrometer scale should be also obtainable. Studying the coloration and bleaching of WO_3 locally, allows one, for instance, to design diffusion experiments in which ions move from areas of high coloration into those of lower. Furthermore, the transmission experiments should be conductable spectrally resolved.

To conduct the experiments, WO_3 thin film electrodes suitable for the constructed setup were synthesized and micro structured. The experimental goal of this thesis was to analyze WO_3 by two main types of experiments, (1) time resolved in situ transmission experiments during electrochemical ion insertion/extraction and (2) spatially and temporally resolved transmission experiments during ion diffusion.

The thesis is subdivided into the following chapters:
The first chapter, *fundamentals*, gives information about the material system studied, WO_3, and about basic principles of ion diffusion inside a solid as well as electrochemical methods including the determination of the diffusion coefficient.
The chapter *experimental setup and sample preparation* presents the spectro-electrochemical microscope system and introduces methods used for preparing WO_3 thin films.
The chapter *results and discussion* is divided into three parts. The first part demonstrates by proof of principle the functionality of the presented setup and gives an overview of possible operation modes for conducting the optical experiments. The second part discusses the results of time resolved in situ transmission experiments of WO_3 thin films during hydrogen and lithium insertion and extraction. The third part presents imaging of the ion diffusion of hydrogen inside WO_3.
The thesis is concluded by *conclusions and outlook* which summarizes the results of this work and suggests experimental approaches that may be considered in the future.

1 Fundamentals

1.1 Crystal structure of tungsten trioxide

Depending on the temperature solid tungsten trioxide (WO_3) exhibits different polymorphs which are determined by different spatial arrangements of the WO_6 octahedra. Below -40 °C a monoclinic phase is found [13, 14]. Between -40 °C and 17 °C, a triclinic crystal structure is evident and in the temperature range of 17 °C and 330 °C another monoclinic phase exists [13, 15]. Beyond 330 °C the material crystalizes in an orthorombic lattice and, finally, beyond 740 °C a tetragonal phase exists [16, 17]. Basically, the crystal structure of monoclinic WO_3 at room temperature can be derived from the cubic ReO_3 structure (figure 1.1 (b)) (adapted from [18]), which has rhenium cations at the corners of a simple cubic lattice and oxygen anions centered on every edge. This arrangement can also be described as a *defect Perovskite structure*, as will be shown in the following.

(a)   (b)
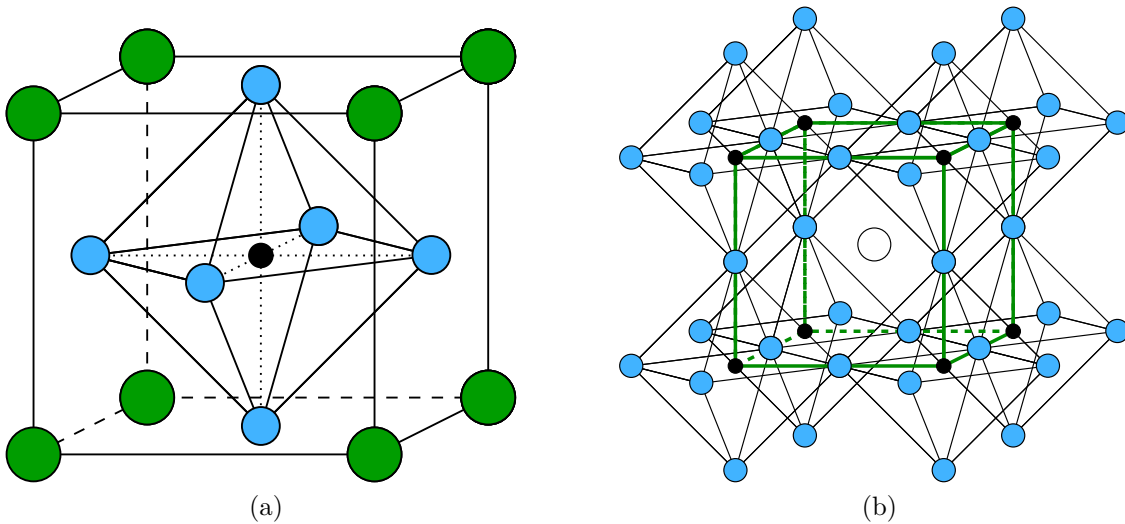
Figure 1.1: (a) Unit cell of the Perovskite structure. Cation A: green, cation B: blue.
(b) ReO_3 or cubic defect Perovskite structure formed by eight corner-sharing octahedra and one vacancy in the center of the primitive cubic cell. Cation B: black, anion: blue, vacancy: transparent. Adapted from [18].

The Perovskite structure is found for ABO_3 compounds for which the sum of charge of cations equals 6 and one of the cations exhibits a size comparable to that of the O^{2-}-ion. Figure 1.1 (a) (adapted from [18]) shows the unit cell of the *Perovskite* structure. Cation species A, depicted in green and the oxygen anions, depicted in blue, form a face centered cubic lattice. Cation species B is located at the center of the octahedron. Removing the large cation, A, yields the defect Perovskite structure. The corner-shared octahedral structure made up of cation species B and the remaining oxygen ions. Lattice sites, which were occupied by cation species A in the Perovskite structure are vacant in this case. Due to these large unoccupied interstitial sites, impurities can easily be inserted into the structure. Crystallographically, the cubic defect Perovskite structure is formed by eight corner-sharing octahedra and one vacancy in the center of the primitive cubic cell (fig. 1.1b). In WO_3, this structural motif is found in a slightly distorted lattice of corner-sharing WO_6 octahedra. Figure 1.2 shows the crystal structure of monoclinic WO_3 with coordination polyhedra, based on the structural model by Tanisaki et al. [13] visualized with the software *Diamond*. Tungsten atoms are depicted in black, oxygen atoms in blue. For better visibility the surface planes of the WO_6 octahedra are marked in green. The formation of channels in the underlying defect Perovskite structure is visible. The monoclinic symmetry arises from the orientation of the WO_6 octahedra relative to each other.
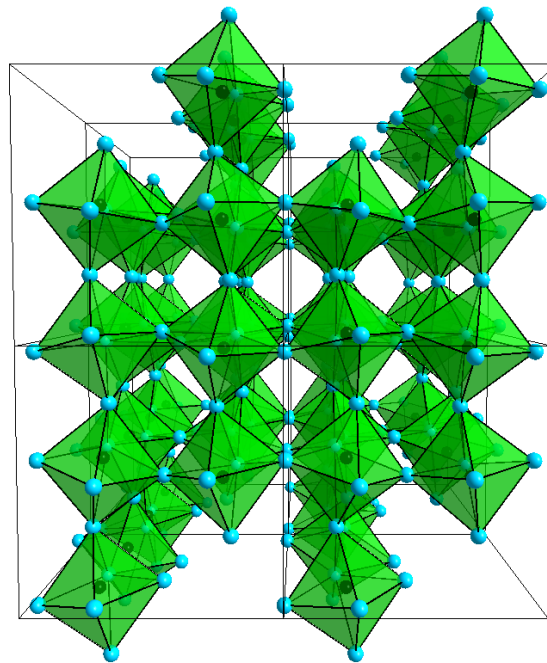
Figure 1.2: Crystal structure of monoclinic WO_3 with coordination polyhedra. W: black, O: blue. From [13] visualized with the software *Diamond*.

Ions can move along these channels of interstitial sites during insertion. Point defects will be discussed in more detail in the context of diffusion mechanisms in section 1.4.3. In the course of ion insertion the crystal structure can be altered. Zhong et al. performed electrochemical lithium insertion into monoclinic (M) tungsten trioxide. For different degrees of charge insertion, x. X-ray diffractograms were recorded and showed phase transitions to a tetragonal (T) and eventually a cubic (C) crystal lattice. The relationships between the tetragonal and cubic unit cells and the monoclinic unit cell is depicted in figure 1.3 (a) [19].

(a)   (b)
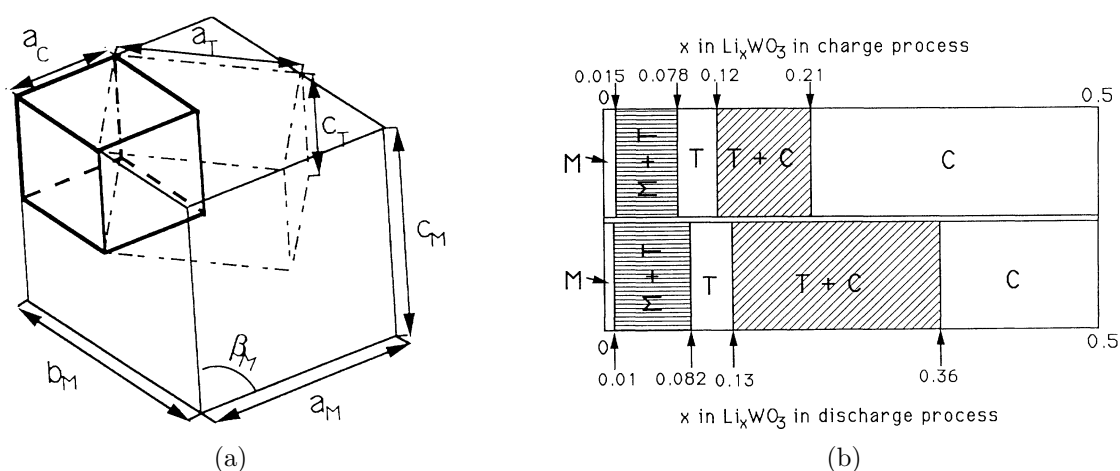
Figure 1.3: (a) Relationships between the tetragonal and cubic unit cells and the monoclinic unit cell of Li_xWO_3. (b) Phase diagram for electrochemically formed Li_xWO_3 at room temperature for the discharge/charge process as a function of inserted charge, x (Copyright (1992) by The American Physical Society [19]).

Compared to a monoclinic structure, the unit cell volume is reduced by a factor of 4 in the tetragonal system and by a factor of 8 in the cubic system. The initial monoclinic WO_3 undergoes a phase transition and a two phase region (M+T) exists for values of $0.01 \leq x \leq 0.082$ in lithium inserted tungsten trioxide, Li_xWO_3. A single tetragonal phase exists for $0.082 \leq x \leq 0.13$. Another two phase region (T+C) occurs in the range of $0.13 \leq x \leq 0.36$ transforming into a single cubic structure for $0.036 \leq x \leq 0.5$. Zhong et al. summarized their findings in a phase diagram depicted in figure 1.3 (b). It shows the phases observed for electrochemically formed Li_xWO_3 at room temperature for the discharge (lithium insertion) and charge (lithium extraction) process as a function of inserted charge, x. Unit cell dimensions

obtained by Zhong et al. are [19]:

$$a_{\mathrm{M}} = 7.310\,\text{Å},$$
$$b_{\mathrm{M}} = 7.540\,\text{Å},$$
$$c_{\mathrm{M}} = 7.695\,\text{Å}, \tag{1.1}$$
$$\beta = 90.89°,$$
$$V_{\mathrm{M}} = 424.1\,(\text{Å})^3,$$

$$a_{\mathrm{T}} = 5.203\,\text{Å},$$
$$c_{\mathrm{T}} = 3.844\,\text{Å}, \tag{1.2}$$
$$V_{\mathrm{T}} = 104.3\,(\text{Å})^3,$$

$$a_{\mathrm{C}} = 3.729\,\text{Å},$$
$$V_{\mathrm{C}} = 51.73\,(\text{Å})^3 \tag{1.3}$$
$$(\text{for } \mathrm{Li_{0.37}WO_3}).$$

The experimental observation of phase transitions during an electrochromic experiment will be discussed in more detail in chapter 3.

1.2 Electrochemical cells

In the following the fundamentals of electrochemical cells are summarized (using [20, 21, 22]). Further details can be found in standard text books. An electrochemical half cell is an arrangement of an electric conducting electrode in contact with an ion conducting phase, called electrolyte. Since only differences of potentials can be measured in experiments, at least two half cells are combined to form an *electrochemical cell*. At the interface of electrode and electrolyte, electrochemical reactions take place. Meaning that by transfer of electrons towards the electrode the species is oxidized. And by electron transfer from the electrode the species is reduced:

$$\mathrm{Ox} + \mathrm{e}^- \longleftrightarrow \mathrm{Red}. \tag{1.4}$$

A simple example are the reactions of a lithium electrode in contact with a lithium ion conducting electrolyte. Both, electrode and electrolyte can be either solid or liquid, depending on their composition and temperature. In this half cell, lithium atoms from the electrode can go into the electrolyte as ions, leaving electronic charge at the electrode (oxidation of lithium). Or lithium ions from the electrolyte are deposited as lithium metal on the electrode surface (reduction of lithium):

$$\mathrm{Li}^+ + \mathrm{e}^- \longleftrightarrow \mathrm{Li} \tag{1.5}$$

The equilibrium potential of this half cell is given by the *Nernst equation*:

$$E_0 = E_{00} + \frac{RT}{zF} \cdot \ln(a_{\mathrm{Me}^{z+}})$$ (1.6)

where E_{00} is the standard equilibrium electrode potential (tabulated values for respective electrodes), R: universal gas constant, T: absolute temperature, z: ionic valence, F: Faraday constant and $a_{\mathrm{Me}^{z+}}$: the chemical activity, which is related to the concentration via the activity coefficient γ, which itself is a function of concentration: $a = \gamma c$.

The lithium-iodine battery, invented by Schneider and Moser in 1972, is a simple lithium based electrochemical cell [22]. Today it is used to supply pacemakers. The cell comprises a lithium electrode, a solid lithium ion electrolyte and a second electrode containing iodine, I_2. The arrangement is equivalent to that of an electrochromic tungsten trioxide cell, depicted in figure 1.5. The electrode reaction of the lithium half cell is described by equation 1.5 and the electrode reaction for the iodine half cell is given by:

$$I_2 + 2\mathrm{Li}^+ + 2\mathrm{e}^- \longleftrightarrow 2\mathrm{LiI}$$ (1.7)

The cell voltage, at zero current, ΔE_0, is often called *open circuit potential* (OCP), and is given by the difference of both half potentials. If both electrodes are connected by an electric resistance, i.e. creating a galvanic cell, electrons from the lithium electrode move to the iodine electrode. Lithium is oxidized and thus the potential of the lithium electrode is shifted toward higher potentials, see equation 1.5. At the same time, the potential of the iodine electrode is shifted towards lower potentials by the reduction of iodine, yielding the overall cell reaction:

$$\mathrm{Li} + \frac{1}{2} \cdot I_2 \longrightarrow \mathrm{LiI}.$$ (1.8)

It is worth mentioning that from a thermodynamic point of view the standard potential of the electrochemical cell, ΔE_{00}, is directly proportional to the standard free enthalpy for the cell reaction ($\Delta_{\mathrm{r}} G^\circ$), meaning that the higher the voltage (OCP), the higher the chemical driving force for that reaction.

1.2.1 Reference electrodes

Usually only one electrode of an electrochemical cell is of interest and that is the so called *working electrode*. For instance, if the potential of the iodine electrode during current flow is of interest, a measurement against the lithium electrode of the battery is not helpful since its potential also shifts due to current flow and therefore is not suitable as potential reference point. This second electrode is called *counter electrode* or *auxiliary electrode*. In order to reliably measure the working electrode's

potential, a third electrode, which, at a constant temperature, has a thermodynamically fixed potential and which is not affected by electric currents, is needed. That kind of electrode is called *reference electrode* and must allow a quick and repeatable setting of the electrode equilibrium potential. For aqueous electrolytes typical reference electrodes are the saturated calomel electrode or the Ag/AgCl electrode. The Ag/AgCl electrode, or more precisely half cell, consists of silver covered with solid AgCl and is immersed in a solution of known KCl concentration. The electrode reaction is given by:

$$\text{Ag} \longleftrightarrow \text{Ag}^+ + \text{e}^- \tag{1.9}$$

The equilibrium potential E_0 for a metal ion electrode is defined by equation 1.6. Applying the Nernst equation to the Ag/AgCl electrode yields:

$$E_0^{\text{Ag/Ag}^+} = E_{00}^{\text{Ag/Ag}^+} + \frac{RT}{F} \cdot \ln(a_{\text{Ag}^+}) \tag{1.10}$$

The only variables determining the potential of the electrode in this equation are temperature and activity of silver ions in the electrolyte. To achieve a constant potential, it is necessary to fix both variables. For the silver ions this is done by the use of silver chloride, which has a very low solubility in water. The equilibrium concentration of silver in the solution is given by the solubility product of AgCl, given by equation 1.11, and hence by the concentration/activity of chlorine ions in solution:

$$a_{\text{Ag}^+} = \frac{K_a^{\text{AgCl}}}{a_{\text{Cl}^-}} \tag{1.11}$$

with K_a^{AgCl}: solubility product, forming:

$$E_0^{\text{Ag/AgCl/Cl}^-} = E_{00}^{\text{Ag/Ag}^+} + \frac{RT}{F} \cdot \ln(K_a^{\text{AgCl}}) - \frac{RT}{F} \cdot \ln(a_{\text{Cl}^-}). \tag{1.12}$$

The standard potential for a Ag/AgCl electrode is defined by:

$$E_{00}^{\text{Ag/AgCl/Cl}^-} = E_{00}^{\text{Ag/Ag}^+} + \frac{RT}{F} \cdot \ln(K_a^{\text{AgCl}}) \tag{1.13}$$

yielding the equilibrium potential of the Ag/AgCl electrode:

$$E_0^{\text{Ag/AgCl/Cl}^-} = E_{00}^{\text{Ag/AgCl/Cl}^-} - \frac{RT}{F} \cdot \ln(a_{\text{Cl}^-}), \tag{1.14}$$

which consist only of a_{Cl^-} and the temperature as variable. This is an important fact as chlorine does not participate in the electrochemical reaction of the electrode. The most important feature of a reference electrode is a constant equilibrium electrode potential. Due to leakage currents, however, a_{Cl^-} can vary and thus the equilibrium potential would not be constant. In order to compensate for these fluctuations, a

freely soluble salt containing the same anion can be added to the system. In the case of a Ag/AgCl electrode a 1 - 3 mol/L KCl solution surrounding the electrode provides a large number of chloride ions so that the fluctuation of chlorine concentration at the electrode is infinitesimal compared to the total number of chlorine anions of the system. This arrangement is usually inside a glass tube with a frit at its end in order to measure the potential of the working electrode. For a 1 mol/L KCl-solution the standard potential is [20]:

$$E_{00}^{\mathrm{Ag/AgCl/Cl^-}} = +0.2368 \text{ V vs. SHE (standard hydrogen electrode)}.$$

For nonaqueous experiments containing a lithium electrolyte, lithium metal is often employed as reference electrode. The lithium reaction is again given by equation 1.5. Yielding the half cell potential:

$$E_0^{\mathrm{Li/Li^+}} = E_{00}^{\mathrm{Li/Li^+}} + \frac{RT}{F} \cdot \ln(a_{\mathrm{Li^+}}). \tag{1.15}$$

However, lithium metal can only be employed as a reference electrode if lithium is involved in the redox reaction at the working electrode. A high concentration of lithium ions inside the electrolyte solution can then compensate for fluctuations of the lithium ion concentration at the reference electrode due to leakage currents. In experiments, problems may arise when electrolyte species are decomposed due to the highly reactive lithium electrode.

1.2.2 Three-electrode cells

A typical cell arrangement for fundamental electrochemical studies of electrode reactions is the so-called three-electrode cell, consisting of a working, a reference and a counter electrode.
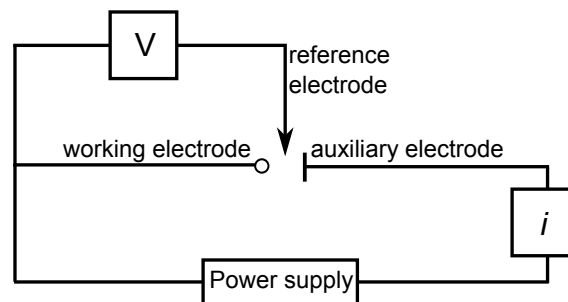
Figure 1.4: Three-electrode cell consisting of working, counter and reference electrode. A potentiostat measures the current and potential of the working electrode (adapted from [21]).

The current is passed between counter and working electrode. The reference electrode is brought close to the working electrode in order to reduce the iR drop (voltage

drop due to the resistance of the electrolyte). The potential difference between both electrodes is measured by the potentiostat using a high impedance voltmeter, so that only an insignificantly small current is drawn through the reference electrode. Figure 1.4 depicts the circuit diagram of a three-electrode cell arrangement and the potentiostat. The potentiostat can be used to measure or control the current between counter and working electrode or the potential between reference and working electrode.

1.2.3 Electrochromic WO_3 cell

As introduced above, electrochemical ion and electron insertion can be realized by two electrodes, in contact with the ion conducting electrolyte. In an electrochromic device at least one component, the electrode or the electrolyte, contains an electrochromic material. In the following only WO_3 is considered as electrochromic material. Figure 1.5 shows a scheme of such an electrochemical cell arrangement.
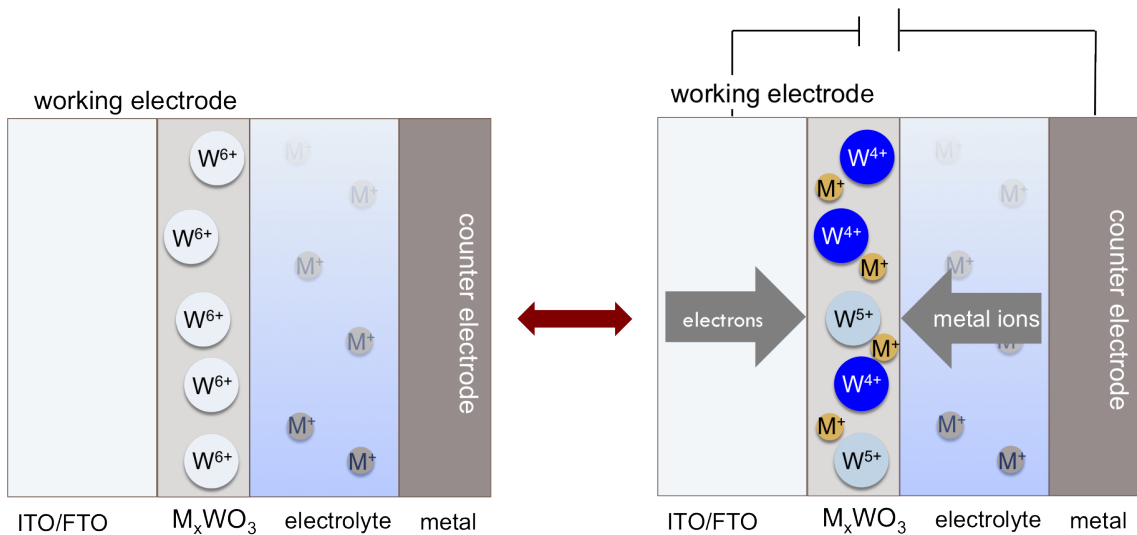
Figure 1.5: Schematic illustration of the electrochromic coloration process. Ions from the electrolyte are inserted into the WO_3 thin film. Due to reduction of tungsten atoms the absorption is changed.

In this work the working electrode comprises a transparent conductive substrate (TCO), for example glass coated with indium tin oxide (ITO) or fluorine doped tin oxide (FTO), on which a thin ($< 1\,\mu m$) WO_3 film, crystalline or amorphous, is deposited. The working electrode is connected by an external circuit to a second, mostly metallic, electrode. Both electrodes are immersed in a liquid electrolyte solution. By driving an electrical current between both electrodes, ions from the solution are inserted into or extracted from the electrochromic thin film, depending on the polarity of the potential. During the ion insertion process charge compensating

electrons from the external electric circuit cause chemical reduction of the tungsten atoms yielding W^{5+} and W^{4+} states generating a blue coloration of the thin film. Depending on the counter electrode, the reduction and coloration of WO_3 by insertion of e.g. hydrogen or lithium is either a spontaneous or a non-spontaneous reaction, which means that either electric energy is released from or needs to be applied to the cell. For instance in the case of a WO_3 electrode and a lithium counter electrode, the coloration is spontaneous, and the cell works as a battery during discharge. The cell reactions for counter and working electrode can be described as follows.

For hydrogen insertion from acidic electrolyte solutions:

$$\begin{aligned} \text{Counter electrode: } & H_2O \rightarrow \frac{1}{2}O_2 + 2H^+ + 2e^- \\ \text{Working electrode: } & WO_3 + xH^+ + xe^- \rightarrow H_xWO_3 \end{aligned} \tag{1.16}$$
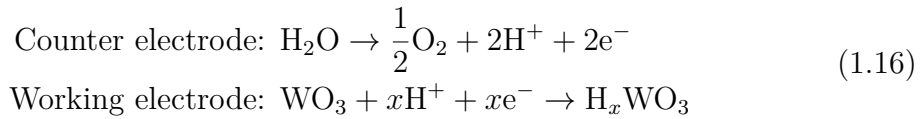
For lithium insertion from non-aqueous electrolyte solutions:

$$\begin{aligned} \text{Counter electrode: } & Li \rightarrow Li^+ + e^- \\ \text{Working electrode: } & WO_3 + xLi^+ + xe^- \rightarrow Li_xWO_3 \end{aligned} \tag{1.17}$$
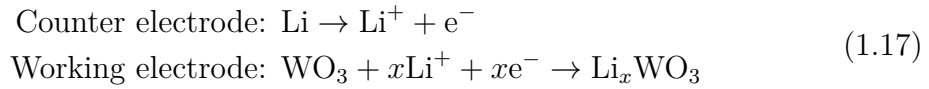
1.3 Electrochromism

Chromogenism is the property of a material to reversibly change its optical properties as a function of an externally controllable parameter. For example, thermochromic layers change their optical properties when heating or cooling the material and photochromic thin films change their optical properties upon irradiation. An important field of chromogenism is electrochromism, which was defined by Monk et al. as "electrochemical generation of color in accompaniment with an electron transfer reaction" [23]. Electrochromism is probably the best investigated field of chromogenism and the most promising candidate for a wide range of applications, such as intelligent fenestration (regulation of energy throughput), automotive rear-view mirrors (variable reflectance), diplays, road signs etc. [2]. Electrochromic displays (ECD) were first suggested in 1969 by Deb [4], his electrochromic thin films were made of tungsten trioxide WO_3. The thin film was deposited on a conductive substrate which was immersed in a dilute acid. As introduced above a simplified reaction for coloration/bleaching of the electrode can be written as [9]:

$$xM^+ + xe^- + \overset{transparent}{WO_3} \longleftrightarrow \overset{colored}{M_xWO_3} \tag{1.18}$$

where $M^+ = H^+, Li^+$, etc. and x: number of inserted ions/electrons. By applying an external potential a dissolved proton is inserted into the thin film at the acid/thin film interface, accompanied by an electron from the external circuit. The

overall process is an electrochemical reduction of tungsten trioxide that in its reduced form absorbs light. However, in reality the processes during optical switching are more complex. The coloration of WO_3 involves several processes, for instance changes in material composition, structure and chemical potential, electronic and ionic transport, formation of polarons and color centers that are all interconnected [2]. This makes mechanistic studies laborious and, although the phenomenon was discovered over 50 years ago, the microscopic mechanisms are not entirely understood and therefore part of current research activities and this thesis. For the study of coloration mechanisms in chromogenic thin films, tungsten trioxide is an ideal model system for several reasons [2]:

- it exhibits different types of chromogenism (thermochromism, photochromism, electrochromism)

- structural and electrical properties have been studied in much detail

- it has been the most relevant optically functioning layer in most ECDs so far

- the physics and chemistry of many other chromogenic oxides, such as MoO_3, are similar.

The microscopic mechanism of the coloration and bleaching are difficult to describe in a single-particle model, i.e. coupling of the carriers to the lattice as well as electron-electron interactions need to be accounted for at least to some degree for an appropriate theoretical description. Therefore, details of the mechanisms are still controversially discussed and a unified model is not established yet. In the following the current views are summarized.

1.3.1 Models for electrochromic coloration in WO_3

A widely accepted coloration mechanism for **amorphous** ion inserted tungsten trioxide, M_xWO_3 (M=H, Li, etc.), is based on polaron formation [24, 25]. Schirmer et al. proposed that inserted electrons are localized at reduced tungsten sites, W^{5+}, and polarize their surrounding lattice and thus form small polarons. Incident light is absorbed and causes hopping of these small polarons from one tungsten site (1) to another (2) according to the following equations [25]:

$$h\nu + W^{5+}(1) + W^{6+}(2) \longrightarrow W^{6+}(1) + W^{5+}(2) \qquad (1.19)$$
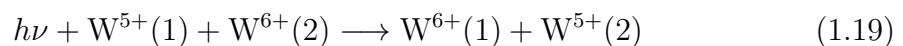
The coloration mechanism of **crystalline** ion inserted WO_3 has hardly been studied but is thought to be based on large polarons and free electron effects [26, 27]. The few suggested models claim that coloration may then either be explained by Drude theory [28], where ion inserted WO_3 is viewed as tungsten bronze [26]; or by the theory of heavily doped semiconductors [9, 29, 30], but a detailed and quantitative

model, which describes the origin of the blue coloration has not been established so far.

The detailed coloration mechanisms are strongly debated: Zhang et al. [31] object to the small polaron model introduced by equation 1.19 as several experimental results cannot be explained by this model [31]. For example, depending on the deposition technique for tungsten trioxide thin films, the oxygen deficiency, y, in as-deposited films, M_xWO_{3-y}, varies in the range of $0 \leq y \leq 0.3$ depending on the environmental conditions. Those films, however, are transparent. This cannot be explained if W^{5+} is assumed to be the main low-valence tungsten ion for the hopping mechanism represented by equation 1.19. Due to the formation of an oxygen vacancy two electrons are left in the crystal that are assumed to be located on tungsten sites, meaning that for each oxygen vacancy the formation of two W^{5+} sites is assumed. For this reason Zhang et al. introduced a modified model indicating that as-deposited tungsten trioxide thin films include mainly W^{6+} and W^{4+} states and can be expressed as $W^{6+}_{1-y}W^{4+}_yO_{3-y} \cdot nH_2O$. Then the pristine films mentioned above are transparent since there is no polaron available. In this model, when tungsten is reduced during the insertion process ($W^{6+} \longrightarrow W^{5+}$), instead of transitions between W^{6+} and W^{5+}, coloration is due to small polaron hopping between W^{5+} and W^{4+} states according to [31]:

$$h\nu + W^{5+}(1) + W^{4+}(2) \longrightarrow W^{4+}(1) + W^{5+}(2) \tag{1.20}$$
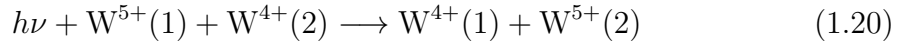
According to Schirmer et al. bipolaronic transitions in amorphous and crystalline WO_3 are more likely than single polaronic transitions (equations 1.20 and 1.21) [32]:

$$h\nu + W^{4+}(1) + W^{6+}(2) \longrightarrow W^{6+}(1) + W^{4+}(2) \tag{1.21}$$
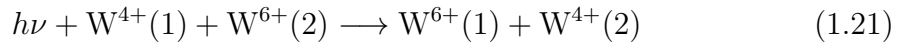
Broklawik et al. suggest to combine features of the coloration mechanisms in amorphous and crystalline tungsten trioxide [33]. Both approaches represent limiting cases, i.e. short range order for amorphous films (localization at a single tungsten site) and long range order for crystalline films (delocalized states of the crystal). A model that suggests a collection of clusters, containing several octahedral structural units of the WO_3 lattice, was introduced to bridge the gap between both approaches. Due to small structural units of the WO_3 lattice, quantum mechanical calculations, such as time-dependent density functional theory calculations can be employed. In a perfect crystal, states of the conduction band would be gradually filled by the inserted electrons. However, there are many defects in a thin film and these give rise to a distribution of energy levels. By insertion of electrons, consecutive levels of this distribution are gradually filled from the lowest to higher energies. This leads to an upward shift of the fundamental absorption edge. In this regard the limiting cases of short and long range order lead to the same conclusion.

Limaye et al. recently published results on in situ extended X-ray absorption fine structure (EXAFS) measurements of WO_3 during coloration/bleaching [34]. Their findings indicate that electrochromic coloration and bleaching can be explained in terms of changes in the electronic states due to filling and unfilling of the $W\,5d{-}O\,2p$ hybridized conduction band states. For coloration lithium ions were inserted into the thin film. According to their model the accompanying charge compensating electrons are transferred into the conduction band and thus cause optical absorption. When the ions are extracted due to reversed polarity of the external electric field, the conduction band is emptied. Limaye et al. also showed that the nearest-neighbor W-O bond distances in the samples do not change upon coloration. This result contradicts models claiming intervalence transitions between W^{6+} and W^{5+} sites or polaron formation being responsible for electrochromic coloration.

According to Larsson et al. the coloration of crystalline WO_3 can be explained by large polaron theory [27]. In contrast to small polarons, a large polaron is not connected to a single tungsten site, i. e. it polarizes several tungsten atoms in its environment resulting in a potential well that localizes or binds it further. With increasing density of inserted ions the polarons start interacting with each other up to a critical density of insertion, where the binding vanishes. Further insertion would then lead to free electron effects described by Drude theory.

As described above Zhong et al. observed phase transitions of crystalline tungsten trioxide upon lithium insertion [19]. The pristine film undergoes a quick transition from an initial monoclinic to a tetragonal lattice for small amounts of inserted charge. Upon further insertion a transition from a tetragonal to cubic structure occurs. For this reason, they object to utilizing the rigid band model for explaining the coloration mechanism because it neglects changes of the crystal structure upon ion insertion. In principle calculations for each crystal structure and also mixed phases would be necessary for a proper description. In general it is difficult to describe the coloration process of WO_3 by the rigid band model, in which it is assumed that the density of states of an alloy can be inferred from that of the host [35]. As shown by Limaye et al., during coloration/bleaching of WO_3 the hybridized $W\,5d{-}O\,2p$ conduction band is filled/unfilled. In order to obtain information about the band structure of inserted tungsten trioxide, the many-body problem should be approached by theoretical calculations. In a recent study Chen et al. published their results on non-rigid band model behavior of sodium inserted tungsten trioxide [36]. Based on their findings, they employed density functional theory, which also considers the hybridization, to calculate the band structure of Na_xWO_3. However, Chen et al. do not take into account that due to the filling of the $W\,5d$ state, at least when tungsten is reduced to W^{4+} and two electrons are inserted into the $W\,5d$ conduction band, the energy levels change.

1.4 Diffusion in solids

Diffusion experiments of ions inside a tungsten trioxide thin film will be presented in chapter 3. Therefore, in the following, fundamentals of diffusion theory and mechanisms are summarized (using [37, 38]). Diffusion describes the way in which particles are transported from one point in space to another as a result of thermal motion. This Brownian motion leads to a distribution of mobile particles in space or the complete mixing of substances when brought into contact. This process is visualized in figure 1.6 (adapted from [37]). The interdiffusion of atoms of two different crystalline materials with a planar interface (e.g. alloying of two metals) is shown. In time the primary sharp interface blends due to diffusion of atoms.
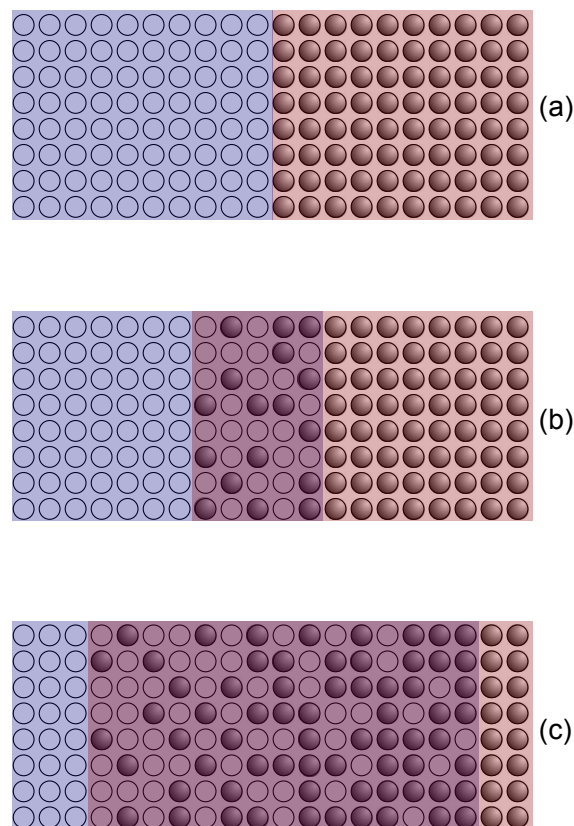
Figure 1.6: Interdiffusion of atoms of two different crystalline materials with a planar boundary. (a) initial sharp interface, (b) early diffusion state of particles and (c) advanced stage of diffusion (adapted from[37]).

Diffusion occurs in all aggregate states and is with a rate of centimeters per second quickest in gases. Diffusion in liquid takes place with rates of the order of millimeters per seconds, and it is slowest in solids exhibiting rates in the realm of nanometers per second, depending on the surrounding conditions, e.g. temperature and pressure.

Science of diffusion is based on the following foundations:

- the *continuum theory of diffusion* by Adolf Fick, known as *Ficks's laws*

- the *Brownian motion* discovered by Robert Brown and interpreted as *random walk* by Albert Einstein

- and in case of solid state diffusion on the formation and movement of point defects as introduced by Max von Laue, Jakov Frenkel and Walter Schottky. Here, point defects play an important role.

1.4.1 Fick's laws and random walk

Fick's laws are phenomenological continuum descriptions, however, since Fick's first publication in 1855 [39] his work has been confirmed by many experiments [38]. The diffusion flux of particles in one dimension in a concentration gradient, as depicted in figure 1.7 (adapted from [38]), for an isotropic medium can be expressed by *Fick's first law*:

$$J_x = -D\frac{\partial c}{\partial x}, \tag{1.22}$$

with J_x: diffusion flux of particles in x-direction and c: particle concentration. Diffusion flux and gradient have opposite directions and the proportionality factor, D, describes the *diffusivity* or *diffusion coefficient* of the considered species. This equation is time-independent.
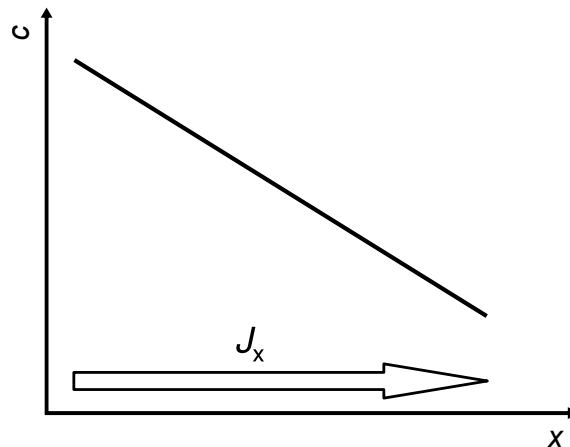
Figure 1.7: Diffusion flux J_x for particles in x-direction in a concentration gradient (adapted from[38]).

It is worth mentioning that D is not a constant but a function of, for instance pressure or temperature and concentration, with temperature being important especially in the condensed state.

Considering time and space dependent concentration changes results in *Fick's second law*:

$$\frac{\partial c}{\partial t} = \frac{\partial}{\partial x}\left(D\frac{\partial c}{\partial x}\right). \tag{1.23}$$

Fick's second law is often referred to as *diffusion equation*, it is a second order differential equation, which is non-linear for concentration dependent diffusion coefficients.

Besides *Brownian motion*, movements of particles can be described as *random walk*, which is a mathematical model for stochastic movements. It can be applied for describing diffusion of atoms inside a solid. The particles are assumed to move by successive random jumps generated by their thermal energy. In a one dimensional case the probability for a particle to jump to the right or to the left is the same. It results in the expression:

$$<x^2>= na^2 = \Gamma ta^2, \tag{1.24}$$

with $<x^2>$: average square of distances that each of the diffusing particles reaches after carrying out n jumps during the time t, a: jump distance, equal for each step of the random walk, Γ: frequency with which each particle jumps to the next position. By applying Fick's first law, the diffusion coefficient can be defined as follows:

$$<x^2>= 2D_\Gamma t, \tag{1.25}$$

where D_Γ is the random walk diffusion coefficient. Transforming this expression leads to the penetration depth, also called diffusion length, for one dimensional diffusion:

$$x_p = \sqrt{2D_\Gamma t}, \tag{1.26}$$

The random walk diffusion model can be employed for deriving a distribution of the particle distances from the starting point after n steps for each particle as a function of time:

$$N(x) = \frac{2N}{\sqrt{2\pi n}} \cdot \exp\left(\frac{-x^2}{4D_\Gamma t}\right), \tag{1.27}$$

with N: number of particles taking part in the random walk and n: number of steps in each random walk. This expression corresponds to a Gaussian distribution; a smoothed distribution for the final position reached by $10\,000$ particles after each has completed a one dimensional walk of 400 steps can be simulated and is depicted in figure 1.8 (adapted from [37]).

1.4.2 One dimensional non-steady state solution for a thin film geometry

For specified boundary and initial conditions of a diffusion problem, solutions for concentration as a function of time and space are usually calculated numerically

Number of particles
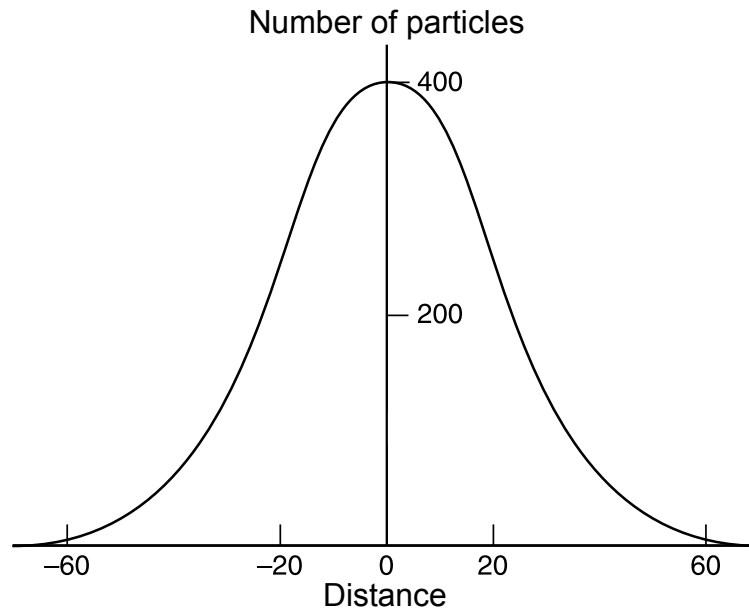
Figure 1.8: Distribution for the final position reached by 10 000 particles after each has completed a one dimensional walk of 400 steps (adapted from [37]).

using Fick's second law. For highly symmetric geometry, solutions can be obtained analytically. Typically, those analytical solutions are given by Gaussians (equation 1.27, figure 1.8), error functions or similar integrals, or Fourier series. A thin film geometry with a line of diffusants at $t = 0$ is one of these highly symmetric geometries and is schematically depicted in figure 1.9 (a). It corresponds to the one dimensional problem with δ-function like distribution of diffusants at $t = 0$. In the case of non-steady-state diffusion in one dimension, where the diffusing species are deposited at $t = 0$ at the plane $x = 0$, the diffusant spreads for $t > 0$. The initial concentration distribution is described by a *Dirac delta function*:

$$c(x, 0) = N\delta(x), \tag{1.28}$$

where N denotes the amount of diffusing particles per unit area. For $t > 0$ the diffusant spreads into the half-space of positive x and the solution is given by a Gaussian:

$$c(x, t) = \frac{N}{\sqrt{\pi D t}} \exp\left(-\frac{x^2}{4Dt}\right), \tag{1.29}$$

Figure 1.9 (a) shows schematic illustrations for the quasi one dimensional non steady-state diffusion for $t = 0$, with a concentration distribution of a Dirac δ-function, and for $t = \infty$, when the diffusant is distributed homogeneously. Figure 1.9 (b) shows the solution for the concentration as a function of spatial coordinate x. The concentration profile is depicted for different times or diffusion lengths, $\sqrt{2Dt}$. The
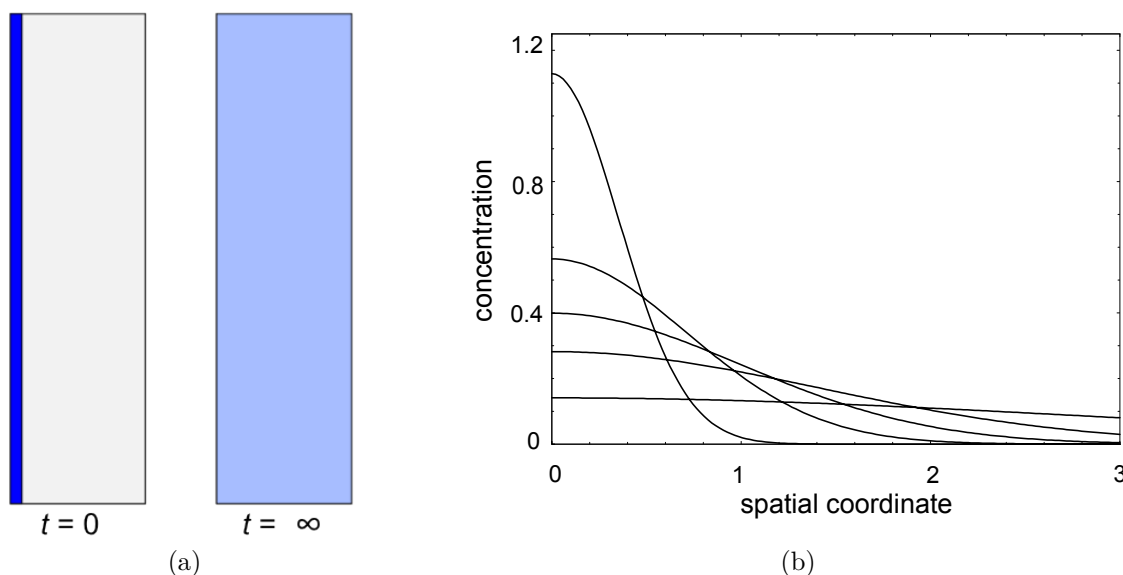
Figure 1.9: (a) Schematic illustration for a one dimensional non steady-state diffusion for $t = 0$ and for $t = \infty$ (homogeneous distribution of the diffusant). (b) Gaussian solution of a non-steady state diffusion equation for a 1D thin film geometry for different diffusion lengths (adapted from [38]).

original sharp concentration gradient flattens with progressing time and eventually approaches a constant value zero. In a real experiment, however, simultaneous measurement of concentration as a function of time **and** space is rather complicated. Therefore most electrochemical experiments for determining diffusion coefficients are indirect methods as, for example, electrochemical impedance spectroscopy or galvanostatic intermittent titration, which will be introduced in section 1.4.4. An approach for measuring the diffusion directly and simultaneously as a function of time and spatial coordinate was developed in the framework of this thesis and will be introduced in chapter 2.1.1.

If a tungsten trioxide thin film is electrochromically colored for a short period of time by, for example, a potential or current pulse, diffusion may in principle be described by the above model in a thin film geometry. However, in an experiment different phenomena, such as self-bleaching, which will be more thoroughly discussed in chapter 3, will affect the process in a complicated manner and hence may cause deviations from the simple diffusion description.

1.4.3 Point defects

For the mechanism of diffusion in a solid, the structure of the matrix inside which diffusion occurs and the presence of defects need to be considered. In a crystal, a

species moves from an energetically favorable position, i.e. a regular lattice site, via a less stable position to another stable position. In a perfect crystal such a movement is improbable and the velocity of diffusion depends on the number of defects.

In a solid, a point defect is an irregularity in a periodic lattice. A point defect characterized by a missing atom is called *vacancy*. If an atom creates a vacancy by moving to an interstitial site of the lattice, it is called a *self-interstitial*, those are typical for single element metals or semiconductors. *Substitutional defects* are impurities that occupy a normal position in the crystal, for example silicon doped with boron or nitrogen.

Self-interstitials, *Frenkel* and *Schottky* defects are called intrinsic. Their formation is favorable from a thermodynamical point of view (increase of entropy) and hence are always present in a crystal at $T > 0\,\mathrm{K}$. If in a lattice of a compound, e.g. MX, an ion is missing in its cation (M) or anion (X) sublattice, the compound will have a nonzero net charge. In order to preserve electrical neutrality the anion and cation sublattices must be balanced out. Vacancies of balanced population of anion and cation vacancies are called Schottky defects (figure 1.10 (a)). If an atom or ion moves from its sublattice to an interstitial site, a vacancy and an interstitial are created. This defect pair is called Frenkel defect (figure 1.10 (b)).
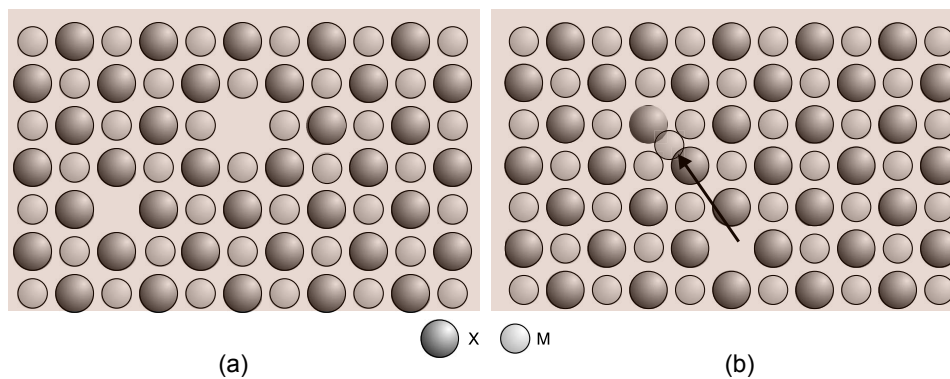
Figure 1.10: (a) Schottky and (b) Frenkel defect in an ionic crystal of formula MX (adpated from [37]).

By jumps of an atom from an occupied lattice site to a neighboring vacancy the atom may diffuse within the crystal. After each jump the atom leaves a vacancy behind, thus in practice this indirect diffusion mechanism is often referred to as *vacancy diffusion*. In most pure metals vacancy diffusion is the most common diffusion mechanism.

Another indirect diffusion mechanism is the *interstitial diffusion*, here an interstitial may jump to a neighboring unoccupied interstitial site. Another mechanism for interstitial diffusion is the *interstitialcy diffusion*. An atom jumps to an occupied

position and causes a displacement of the atom that formerly occupied that position into a neighboring interstitial site.

If an impurity jumps to a site of a normal atom a substitutional defect is created, the former occupant is displaced to an interstitial site, which is then called *self-interstitial*. This process is also called *kick-off mechanism* [37]. In WO_3 hydrogen or lithium diffusion can take place via the large vacant interstitial sites of the defect perovskite related structure (see figure 1.2).

1.4.4 Determination of lithium diffusion coefficients in literature

In many applications the magnitude of diffusion coefficients is of high importance. In the case of WO_3 it is one of the factors limiting the switching speed between transparent and colored states. This section introduces electrochemical methods that are commonly used for indirectly determining diffusion coefficients of ions inside a solid. *Electrochemical impedance spectroscopy* (EIS) and *galvanostatic intermittent titration* (GITT) are such electrochemical methods. Furthermore a spectroelectrochemical approach for the measurement of the diffusion coefficient in lithium cobalt oxide (LCO) by Berkemeier et al. is discussed.

Electrochemical impedance spectroscopy (EIS)

Mattson et al. determined lithium diffusion coefficients by EIS and GITT and compared their findings with literature values, both are tabulated in table 1.14. The two methods will be introduced in the following [40]. During impedance spectroscopy the response of an electrochemical cell to the perturbation by an ac voltage (optionally) superimposed on a dc bias is measured. The ratio of applied ac voltage and measured current yields the complex impedance of the system, which is usually modeled by an electric equivalent circuit. A *Randles circuit* is often employed for describing the response of an insertion electrode system. This model of an equivalent circuit is shown in figure 1.11.
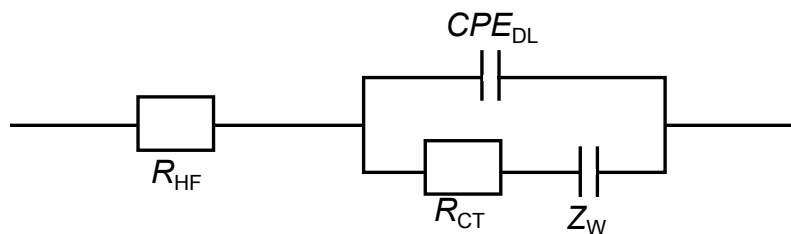
Figure 1.11: Randles circuit of an equivalent circuit (adapted from [40]).

R_{CT} describes the charge-transfer resistance across the electrolyte/sample interface, which is connected in parallel with a double layer distributed capacitance, the so-called constant phase element, CPE_{DL} [40]. A double layer of electric charges is present at each electrode/electrolyte interface [20].

The *Warburg diffusion element*, Z_W, describes the diffusion of inserted species inside the sample [41]; two cases are distinguished:

- semi-infinite length (Z_{SIW}): infinite width of insertion host

- finite length (Z_{FLW}): finite width of insertion host.

The diffusion coefficient of the inserted species can be determined by fitting the experimentally obtained impedance response to the simulation of an equivalent Randles circuit using one of the Warburg impedances.

Figure 1.12 shows the results of Mattsson et al. for impedance response of crystalline and amorphous WO_3 in 1 M $LiClO_4$ in PC at 2.9 V vs. Li. This method yields a value of order 10^{-11} cm^2/s.
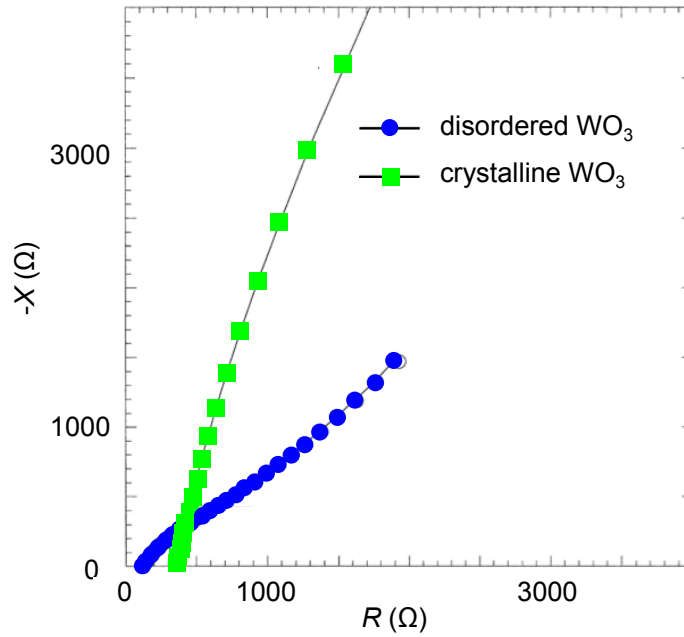
Figure 1.12: Impedance response of crystalline and amorphous tungsten trioxide in 1 M $LiClO_4$ in PC at 2.9 V vs. Li (adapted from [40]).

Galvanostatic intermittent titration

Another established electrochemical method for determining diffusion coefficients in solid electrodes is the galvanostatic intermittent titration (GITT). Ions are inserted by application of a constant current for a small time period τ. Then the system is given time to relax to its equilibrium potential. This procedure is repeated until the insertion range of interest is covered. The diffusion coefficient can then be determined by the following equation:

$$\tilde{D} = \frac{4w^2}{\pi\tau} \left(\frac{\Delta U_\mathrm{s}}{\Delta U_\mathrm{t}} \right)^2 , \qquad (1.30)$$

where ΔU_s is the change in open circuit potential and ΔU_t denotes the total change of voltage during the chronopotentiometric (constant current) phase. Equation 1.30 is valid for the limiting case [42]:

$$\tau \ll \frac{w^2}{\tilde{D}} \qquad (1.31)$$

For a GITT experiment where $\tau > w^2/\tilde{D}$, $\tilde{D}$ can be determined from the slope of U vs. $\mathrm{d}U/\mathrm{d}x$ [43]. Figure 1.13 shows a typical course of relaxed open circuit potential as function of Li/W ratio for amorphous and crystalline WO_3. This method yields a diffusion coefficient of order $10^{-12}\,\mathrm{cm}^2/\mathrm{s}$, one order of magnitude smaller than values obtained by the EIS method. An overview of diffusion coefficients found in literature for lithium in WO_3 gained by different methods is given in table 1.14 [40]. Reported values for the diffusion coefficient of Li in WO_3 are in the range of $10^{-13}\,\mathrm{cm}^2/\mathrm{s}$ to $10^{-9}\,\mathrm{cm}^2/\mathrm{s}$. Diffusion coefficients of hydrogen in WO_3 are in the order of $10^{-10}\,\mathrm{cm}^2/\mathrm{s}$ to $10^{-8}\,\mathrm{cm}^2/\mathrm{s}$ [44, 45, 46].

The drawback of these electrochemical methods is the fact that diffusion properties are indirectly derived from the measurement of an electric response, i.e. impedance or potential relaxation. At no time there is direct proof for diffusion profiles, e.g. concentration of diffusant as function of time and spatial coordinate.
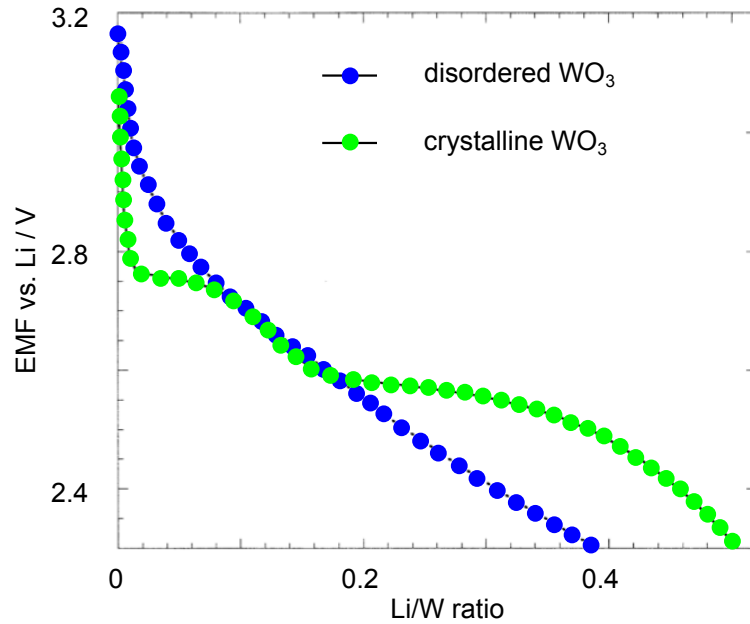
Figure 1.13: Course of relaxed open circuit potential during a GITT experiment as a function of Li/W ratio for amorphous and crystalline tungsten trioxide (adapted from[40]).

$\tilde{D}$ (cm^2/s)	Li/W ratio x	Method	Film preparation, etc.
2.13×10^{-11}	~0	GITT[a]	Thermal evaporation (amorphous, density: 5.8 g/cm^3)
1.5×10^{-10}	0.0011		
4.5×10^{-11}	0.0032		Powder pressing
1.1×10^{-9}	0.12	GITT[b]	(Poly-crystalline: monoclinic)
2.4×10^{-12}	0.097		Thermal evaporation (crystalline:
2.8×10^{-11}	0.26	EIS[c]	tetragonal, density: 5.2 g/cm^3)
1×10^{-12}	0.1		Sol-gel (crystalline:
3×10^{-12}	0.3	EIS[d]	orthorhombic)
2×10^{-12}	–	Potentiostatic erase technique[e]	Rf sputtering (some crystallinity)
1.15×10^{-11}	0.0001	Chrono-	
4.8×10^{-13}	0.001–0.01	potentiometry[f]	Sol-gel (density: 5.0 g/cm^3)

[a] From J.-G. Zhang, C.E. Tracy, D.K. Benson, S.K. Deb, J. Mater. Res. 8 (1993) 2649.
[b] From J. Molenda, A. Kubik, Solid State Ionics 117 (1999) 57.
[c] From C. Ho, I.D. Raistrick, R.A. Huggins, J. Electrochem. Soc. 127 (1980) 343.
[d] From P. Judeinstein, J. Livage, J. Chim. Phys. 90 (1993) 1137.
[e] From M. Green, W.C. Smith, J.A. Weiner, Thin Solid Films 38 (1976) 89.
[f] From G. Xu, L. Chen, Solid State Ionics 28–30 (1988) 315.

Figure 1.14: Diffusion coefficients found in literature for lithium in WO$_3$ obtained by different methods (adapted from [40]).

Spectro-electrochemical measurement of diffusion coefficients

Berkemeier et al. recently published an elegant way to determine diffusion coefficients using a spectro-electrochemical setup [47]. Lithium cobalt oxide (LCO) was deposited on an ITO coated glass substrate and served as working electrode, graphite served as counter electrode. Both electrodes were immersed in a $1\,M$ $LiClO_4$ in a mixture of 1:1 dimethyl carbonate and ethylene carbonate. A schematic image of the setup is given in figure 1.15.
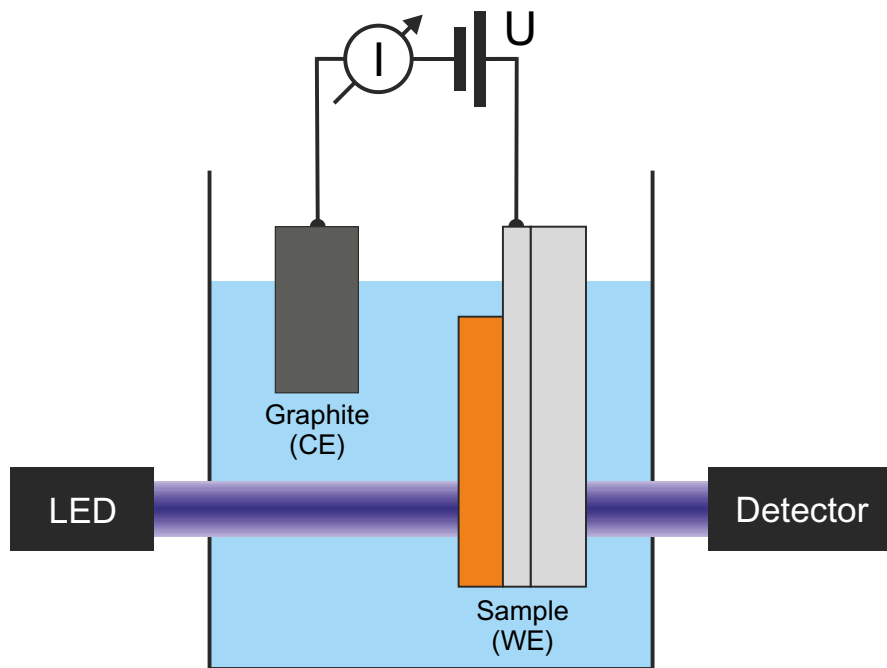
Figure 1.15: Spectro-electrochemical setup for determination of the diffusion coefficient of lithium in LCO [47].

LCO exhibits electrochromic properties thus during lithium insertion and extraction the change of optical absorption of the sample was detected. Experimental data was fitted to a solution of Fick's law and yielded the diffusion coefficient of lithium in LCO with a value of $1.04 \cdot 10^{-13}\,cm^2/s$.

Similar experiments on WO_3 will be presented in chapter 3 including the extension of such a setup to perform spatially resolved measurements. In the present work the absorption is measured as a function of space and time, whereas Berkemeier et al. measured the absorption with temporal resolution only.

1.5 Electrochemical analysis methods

In this work lithium and hydrogen insertion/extraction was carried out in both cyclic voltammetry and constant current potentiometry and in the following the brief fundamentals of both methods will be introduced.

1.5.1 Cyclic voltammetry

Cyclic voltammetry in principle may yield fundamental information on the thermodynamics and kinetics of electrochemical reactions such as reaction rates or standard electrode potentials [48]. In a three-electrode cell a triangular voltage is applied to the working electrode while the responding current is recorded. Figure 1.16 (a) shows the prescribed electrode potential for 3 cycles. Starting at an arbitrary potential (E_{start}), often the OCP is used, the potential is reduced with a constant rate until the scan direction is reversed at $E_{\lambda 1}$. After a second potential, $E_{\lambda 2}$, is reached the scan direction again is reversed and the first cycle is completed when the electrode potential reaches the initial value E_{start}. The current response curve shows three specific regions, highlighted in color, which will be discussed in the following.

A more conventional method for presenting the potential and current data is by plotting E as a function of I, this is possible since E depends linearly on t. The resulting graph is called *cyclic voltammogram* (CV). Figure 1.16 (b) shows a CV for a reversible process, which was simulated by the software *EC-Lab®* by the company *BioLogic, Science Instruments*. The CV is mainly characterized by the following features: Two current peaks at $E = E_{red}$ and $E = E_{ox}$, respectively. The peaks are 58 mV apart and the standard potential, E_{00}, is in between both peak positions. The origin of the CV curve is described as follows, for a simple electrochemical reaction: A redox active substance *ox* in the electrolyte is reduced via single electron transfer at the electrode surface to form a soluble species *red* (see equation 1.4). By reduction of the potential, starting at E_{start}, the *ox* species is reduced at the electrode surface to form *red*. The concentrations of *red* and *ox* are, at the beginning of the process, given by the Nernst equation:

$$\frac{c_{ox}(x=0)}{c_{red}(x=0)} = \exp\left[\frac{zF}{RT}(E - E^0)\right]. \tag{1.32}$$

With decreasing E the absolute value of the current increases, meaning that the rate of *ox* consumption and *red* production increases. This exponential current increase is marked red in the simulated CV. The depletion of *ox* at the electrode surface leads to a concentration gradient within the electrolyte. The concentration gradient increases ($t > t_2$) and is maximal for $t = t_3$. At this point the maximum current is limited by diffusion. The corresponding concentration profile is depicted in figure 1.17 (a). The electrode/electrolyte interface is set to $x = 0$, the electrode's concentration, c, is 1 for $t = t_1 = 0$. The thickness of the diffusion layer for a corresponding time is
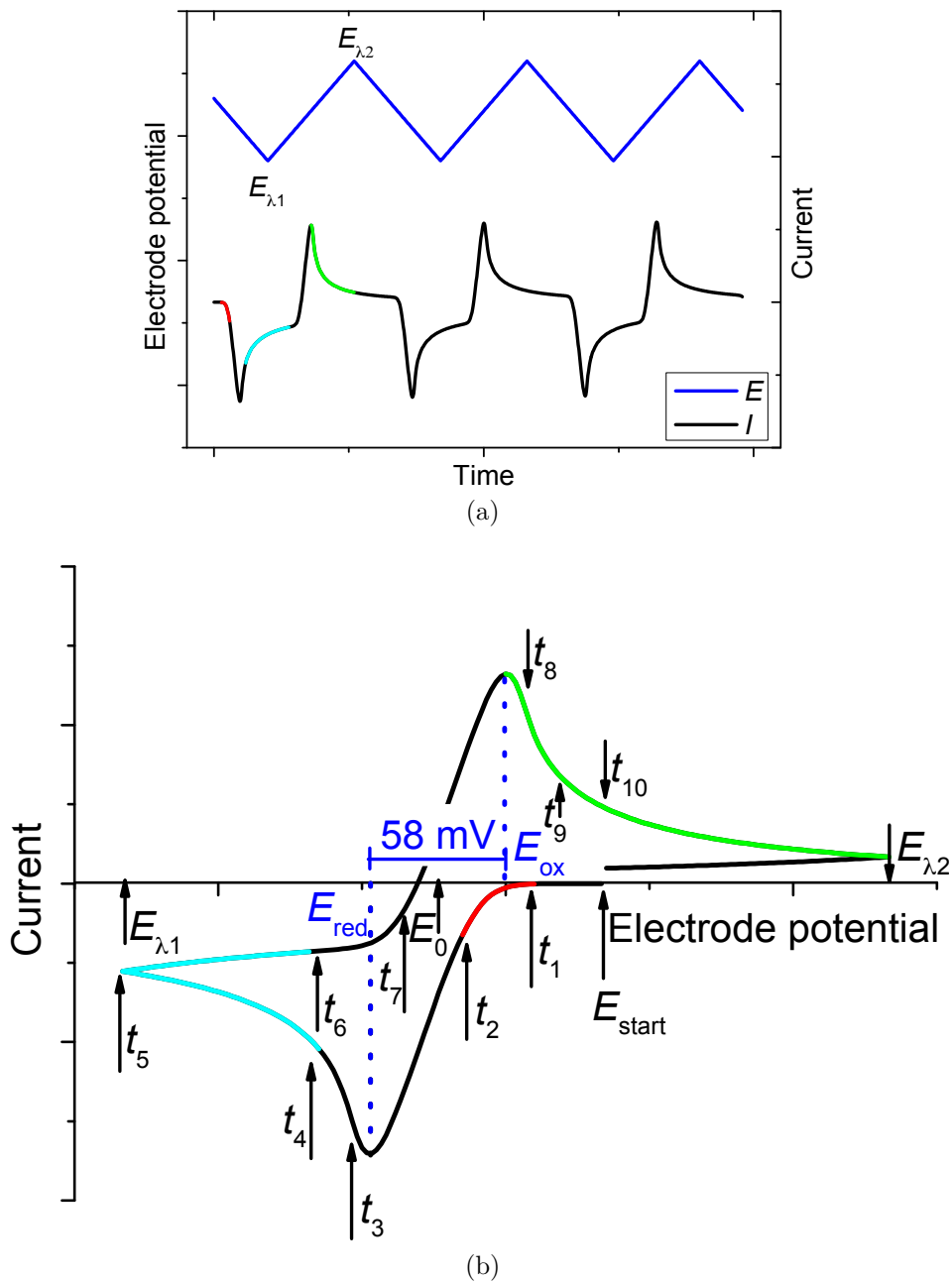
Figure 1.16: (a) Electrode potential for three cycles in a CV experiment and the simulated current response. (b) Cyclic voltammogram, current response as a function of electrode potential. Simulation with the software *EC-Lab®* by the company *BioLogic, Science Instruments* (annotation adapted from [48]).

marked by δ_x. It should be mentioned that similarly a diffusion of *red* takes place but in the opposite direction. The thickness of the diffusion layer, δ, is not constant in time, but it increases with $\sqrt{t}$. This counteracts the increase of concentration gradient and leads to a decrease in absolute current value. The current decays with $\sqrt{t}$; this is marked turquoise between t_4 and t_6 in the CV. For t_5 an educt concentration of zero is given. When the scan direction of the potential is reversed
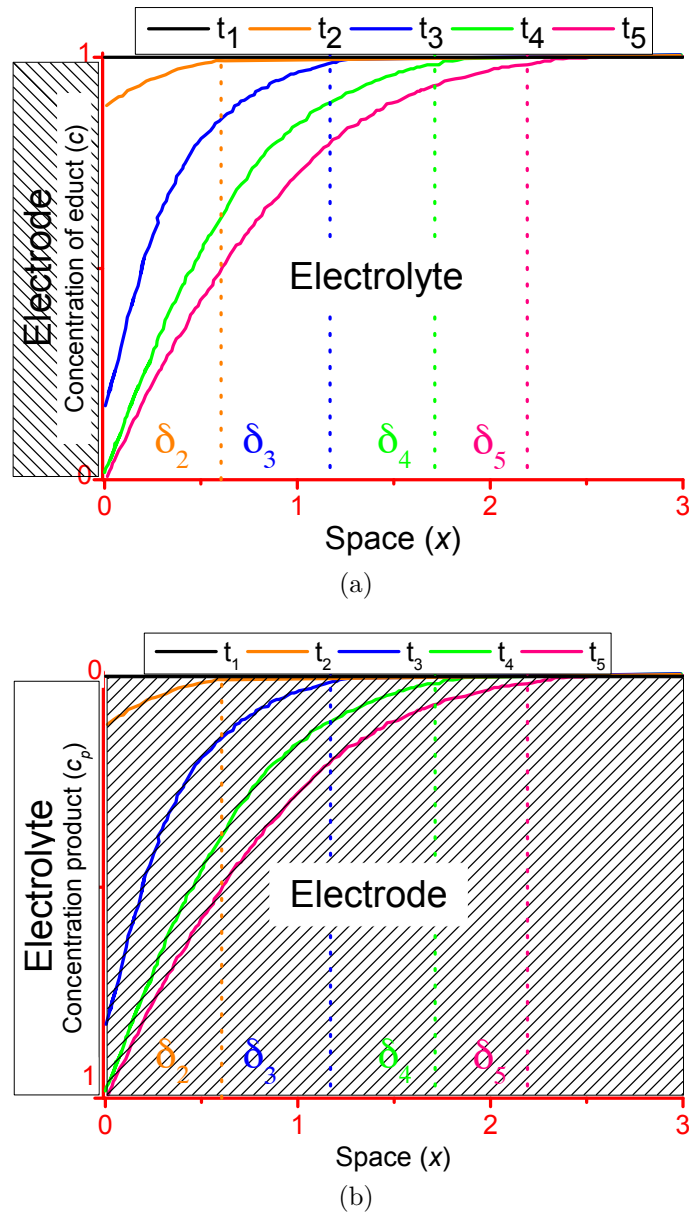
Figure 1.17: Concentration profile caused by the potential variation during a CV inside (a) an electrolyte and (b) an electrode (adapted from [48]).

at $E_{\lambda 1}$, the concentration at $x = 0$ is still zero at first and the CV curve still exhibits a $\sqrt{t}$ form between t_5 and t_6. At a certain point the concentration of *ox* at the electrode increases again according to equation 1.32 by electrochemical oxidation of *red*. A positive cell current is observed. The same processes, as described above, of increase and decrease of the concentration gradient take place and result in an oxidation peak.

In the case of ion insertion into a solid bulk material, the concentration gradient most probably is built within the electrode material rather than within the electrolyte as diffusion in solids is much slower than in liquid phases. The concentration profile may be imagined as depicted in figure 1.17 (b). At $t = 0$ the concentration of the inserted species is zero. With time the concentration increases inside the host structure until it reaches 100% state of charge.

The CV behavior as described above is only observed in simple electrochemical arrangements, such as planar electrodes, where reversible electrochemical reactions, soluble reactants and diffusion are the main limiting processes. For example in the case of ion insertion into WO_3, processes are more complicated, including mass transfer at the electrode/electrolyte interface (insertion/extraction), solid state diffusion, phase transitions etc. A quantitative examination, if possible at all, therefore requires much more elaborate models [49].

1.5.2 Constant current chronopotentiometry

As GITT, the galvanostatic charge/discharge method is a type of chronopotentiometry. When a constant current is applied to the electrode of an electrochemical cell, an underlying reaction is run with a constant rate, which means that the concentration of reactants linearly changes with time. In case of insertion electrodes this corresponds to a linear change of the degree of insertion, also called *state of charge* in battery terms. The change of electrode potential and state of charge can be visualized in a so-called *charge-potential profile* or *charge/discharge curve*. Depending on the type of cell and cell reaction charge-potential curves show some characteristic features. It is mentioned that only for infinitesimal small currents the measured potential corresponds to the equilibrium (Nernst) potential. An overview of some battery cells is provided by R. A. Huggins in his book of *Advanced batteries*. Corresponding charge/discharge curves are depicted in figure 1.18 (a). It can be seen that some discharge curves are almost flat, others possess plateaus, flat regions, and another type is slanted or stretched s-shaped. The three basic types are qualitatively summarized in figure 1.18 (b).

The different types of discharge curves can be explained by the *Gibbs Phase Rule*, which is often written as [22]:

$$F = C - P + 2 \tag{1.33}$$

in which C is the number of components, P the number of phases present in the
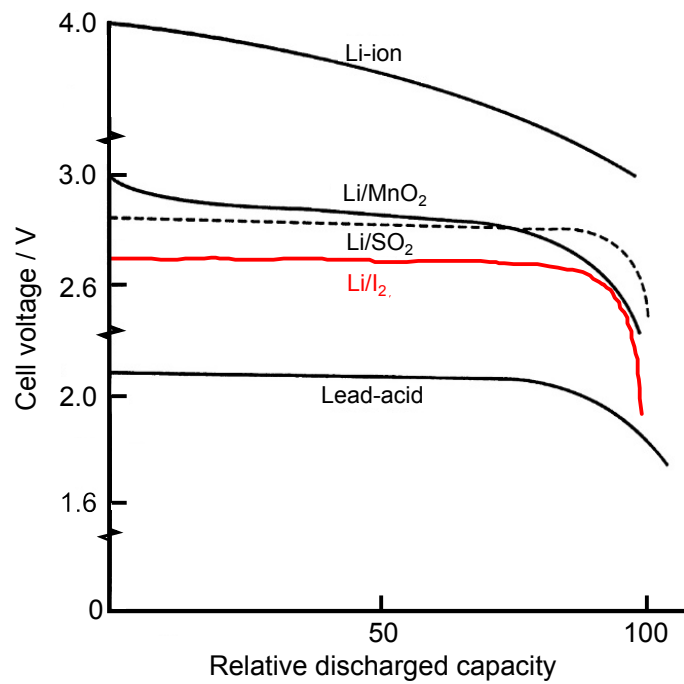
(a)
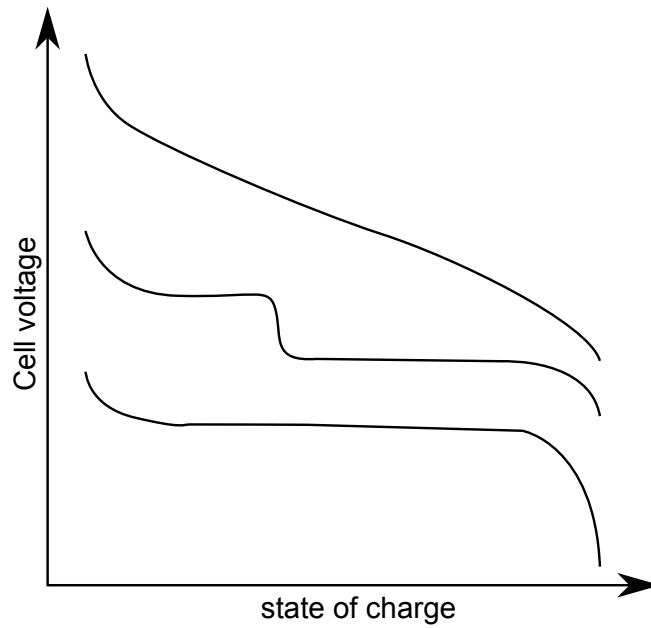
(b)

Figure 1.18: (a) Overview of some battery cell charge-potential profiles. (b) Three basic types of charge-potential profiles (adapted from [22]).

experiment and F the number of degrees of freedom, i.e the number of intensive thermodynamic parameters such as temperature, overall pressure, and the chemical potential or chemical composition of each of the phases present. Here, intensive means that their values are independent of the amount of material present. Using the example of the Li/I_2 battery, the formation of a discharge curve is explained as follows: There is only one phase present at the lithium electrode; one component with only one type of atom, thus P, and the number of components, C, is 1. Therefore F equals 2. Constant current chronopotentiometry is usually carried out at constant temperature and pressure, therefore two intensive variables are fixed and the Gibbs Phase Rule

$$F = C - P \qquad (1.34)$$

holds. No degrees of freedom remain and the *residual value of F* is zero, meaning that all intensive parameters including the potential of the lithium electrode have fixed values. During discharge of the cell, the amount of lithium is decreased and LiI is formed, thus the amount of lithium changes as a function of state of charge, but C and P do not change and the electrode potential remains constant, regardless of the state of charge. The same holds for the positive electrode: It consists of I_2 (educt) and LiI (product) meaning that there are 2 phases and 2 components. Hence for fixed T and p, F equals zero, too. The cell voltage, being the electrode potential difference, is constant, too (neglecting overpotentials), and a flat, plateau-like discharge curve is observed (see figure 1.18 (a)).

Now we consider the lithium insertion into Li_xWO_3 (equation 1.17) and in the first place neglect any changes in the structure of Li_xWO_3. In this case there is one phase (Li_xWO_3), two components (Li, WO_3) and therefore $F = 1$, meaning that the potential of the electrode is not fixed. In a more quantitative way, the Nernst equation for reaction equation 1.17 holds:

$$E_0 = E_{00} + \frac{RT}{zF}\ln\left(\frac{a_{Li^+}}{a_{Li,\,WO_3}}\right) \qquad (1.35)$$

with $a_{Li,\,WO_3}$: the activity of lithium inside the WO_3 lattice. Besides the standard potential, at constant T, the electrode potential depends on the activity of lithium ions in the electrolyte and of lithium in the WO_3 lattice. In combination with the constant half cell potential of the lithium electrode the equilibrium cell voltage follows:

$$\Delta E_0 = E_0^{Li_xWO_3} - E_0^{Li} - \frac{RT}{zF}\ln(a_{Li,\,WO_3}). \qquad (1.36)$$

E_0 decreases with increasing state of discharge, corresponding to an increase of $a_{Li,\,WO_3}$, and shows the s-shaped type depicted in figure 1.18 (b). However, in reality the curves look much more complicated as shown in figures 1.13 and 1.19.

It seems that the voltage profile consists of at least two consecutive s-shaped parts or even two s-shaped parts and two voltage plateaus. This is a result of changes in

the crystal structure of Li_xWO_3 during the insertion process. Two s-shaped parts may be observed if for a certain value of x a transition from the initial to a new phase occurs instantaneously. A real potential plateau is observed if two phases coexist. Qualitatively this can be explained by the Gibbs phase rule with $F = 0$ for $C = 2$ (Li, WO_3) and $P = 2$. A quantitative description is beyond the scope of this thesis but is described in standard textbooks of physical chemistry. Figure 1.19 shows the charge and discharge curve for insertion/extraction of lithium into/from WO_3 by Zhong et al. discussed earlier in terms of crystal phase transitions upon ion insertion. Both two phase regions, monoclinic and tetragonal phase, and tetragonal and cubic phase, suggest potential plateaus. However, a real two phase region, as shown in figure 1.18 (b), is a pronounced horizontal plateau, which is not the case for WO_3. In chapter 3 a similar discharge curve for lithium insertion into crystalline dip-coated WO_3 will be shown. The profile is similar and exhibits two plateau-like features, however, XRD shows that only one phase transition takes place.
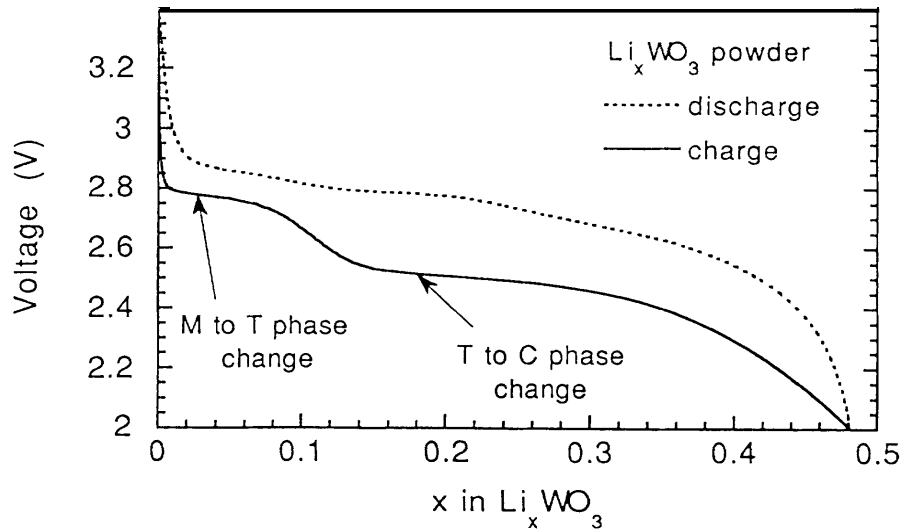
Figure 1.19: Charge and discharge curve for insertion/extraction of lithium into WO_3 (Copyright (1992) by The American Physical Society [19]).

1.6 Sol-gel synthesis

Besides WO_3 thin film synthesis via electron-beam evaporation, a chemical method was also employed. The basic principles of the so-called *sol-gel derived dip-coating method* are described in the following.

A sample comprising colloidal particles with diameter of 1 - 100 nm dispersed in a liquid, solid or a gas is called a *sol*. After hydrolysis and condensation of the initial sol, it can be converted into a *gel*, which is a semi-solid substance containing at least two components, a solid consisting of a network of long-chained or branched polymeric bonds and a fluid as dispersant [50].

Synthesis of metal oxides M_xO_y via *sol-gel* chemistry is based on the polycondensation of metal alkoxides $M(OR)_x$ (where R is typically an alkyl group). These alkoxides can be formed by dissolving suitable metal chlorides MCl_x in an alcoholic solution (ROH) by the following reaction [51]:

$$MCl_x + xROH \longrightarrow M(O)R_x + xHCl \tag{1.37}$$
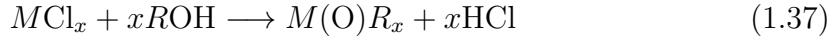
The alkoxide then serves as precursor for the sol-gel synthesis. By adding water to the system, hydrolysis converts the alkoxide into a hydroxide $(M(OH)_x)$ by the following reaction:

$$M(OR)_x + xH_2O \longrightarrow M(OH)_x + xROH \tag{1.38}$$
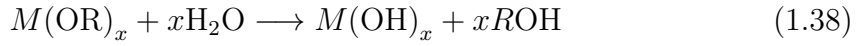
Condensation leads to formation of bridging oxygen, either by *alkoxolation* or *oxolation*:

- alkoxolation: creating a bridging oxo-group between metal atoms by elimination of an alcohol molecule according to the following reaction:

$$R_nM(OH)_x + R_mM(OR)_y \longrightarrow (OH)_{x-1}R_nM-O-MR_m(OR)_{y-1} + ROH \tag{1.39}$$
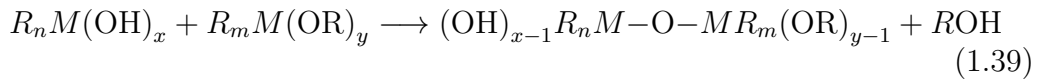
- oxolation: creating a bridging oxo-group between metal atoms by reaction of two hydroxyl groups under release of water according to the reaction:

$$R_nM(OH)_x + R_mM(OH)_y \longrightarrow (OH)_{x-1}R_nM-O-MR_m(OH)_{y-1} + H_2O. \tag{1.40}$$
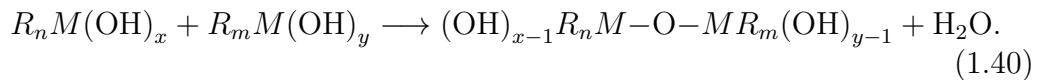
2 Experimental Setup and Sample Preparation

2.1 Experimental setup

In situ transmission spectroscopy of an electrochemically active material is a challenging task. The physical and chemical setups itselves are fairly complex and combining them causes additional constraints. In the following the setup that was specially designed for performing these measurements is introduced. The optical setup consists of a microscope system that is attached to a spectrometer which is equipped with a charge coupled device (CCD) for detecting the signal. The second part of the setup comprises a measurement chamber for electrochemical analysis. Compact cells for aqueous hydrogen insertion and non-aqueous lithium insertion, which can be attached to the microscope system, will be introduced.

2.1.1 Microscope system for time and spatially resolved spectroscopy
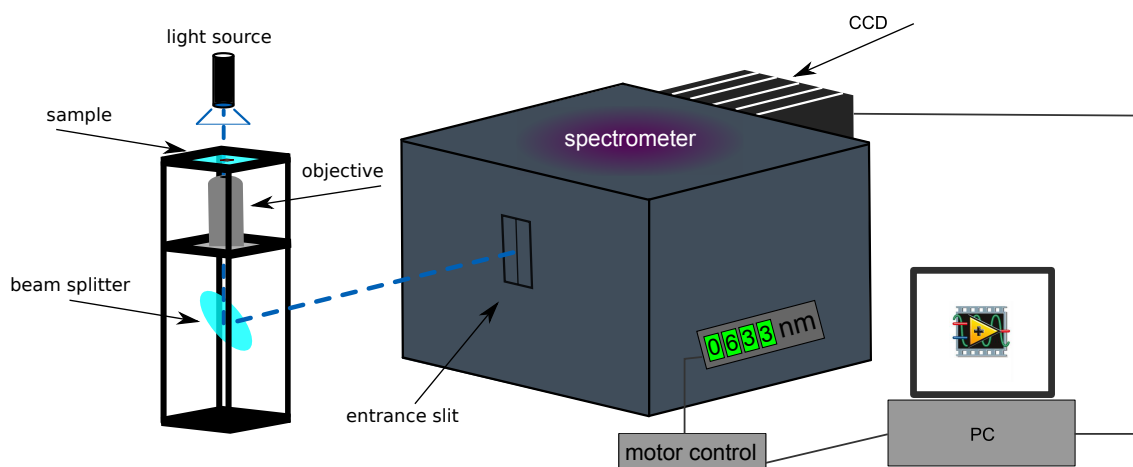
Figure 2.1: Optical setup for time, space and energy resolved transmission spectroscopy consisting of light source, objective, mirror/beam splitter, subtractive double spectrometer and CCD camera.

Figure 2.1 shows a schematic illustration of the optical setup. Spatially resolved experiments on the micrometer scale require a microscope system that yields the desired magnification of the sample. This microscope system should consist of a light source, a microscope stage and an objective. The light source is the top most element of the system and right below it a sample or later an electrochemical cell is placed. The sample can be attached to a microscope stage which allows one to adjust the sample position with respect to the microscope objective, which is situated underneath the microscope stage. The microscope stage, depicted in figure 2.2 (a), is attached to a solid metal table which has a big opening in its center so that sample or cell can be moved freely in $x-$ and $y-$direction.

(a)   (b)
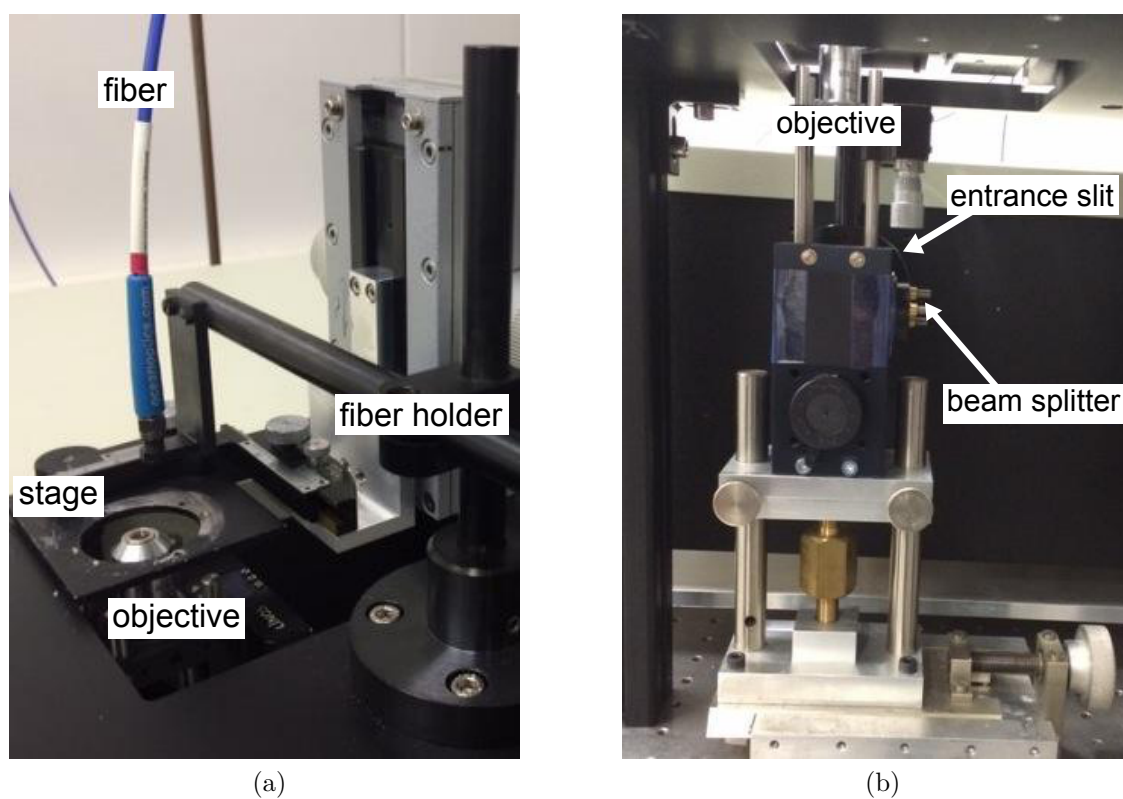
Figure 2.2: Photographic image of the microscope set up. (a) Mobile fiber holder for the probe light, attached to a solid metal table, above the microscope stage; the objective is situated below fiber and stage. (b) Metal skeleton comprising objective and beam splitter.

A frame is attached to the microscope stage such that a cover slip can serve as specimen holder in the case of a single sample. In the case of an electrochemical transmission experiment the electrochemical cell will be attached to the frame. The light of a halogen lamp is transmitted by a commercially available optical fiber (from

the company *ocean optics*) onto the sample. The fiber's end is connected to a mobile holder, shown in figure 2.2 (a), which is attached to the metal table. The fiber holder can be positioned freely above the sample or electrochemical cell. The objective is attached to a metal skeleton with a beam splitter or mirror underneath. The beam splitter reflects the magnified image of the transmitted light by 90° onto the entrance slit of a subtractive double spectrometer, Spex 1680 b by *Horiba*. Besides the transmission mode, the microscope can be operated in a second mode, i.e. reflection mode, yielding two operation modes for the microscope system:

1. transmission mode

2. reflection mode

The light path for each operation mode is depicted in figure 2.3 (a). Transmission measurements can be carried out with the probe light, depicted in yellow, illuminating the top of the sample, as described before. The light transmitted by the sample is magnified by an objective and is reflected onto the entrance slit of the spectrometer by a mirror or beam splitter forming a magnified image of the illuminated sample spot on the entrance slit of the spectrometer.

The reflection mode can be employed for samples deposited on top of an opaque substrate. In this case the sample is placed on the microscope stage upside down. The probe light, depicted in blue, is situated in front of a mirror which reflects the light onto the beam splitter that transmits a fraction of the probe light. The light then passes the objective and is focused onto the sample. The excited sample emits fluorescence light, which is collected by the same objective and is reflected by the beam splitter onto the entrance slit of the spectrometer forming an image of the sample surface in the plane of the entrance slit.

The subtractive double spectrometer serves as a bandpass, i.e. the image that is sent onto the entrance slit is sustained after its wavelength is filtered by a spectral window, $[\lambda_0 - \frac{\Delta\lambda}{2}, \lambda_0 + \frac{\Delta\lambda}{2}]$, where λ_0 is the central wavelength determined by the grating position and $\Delta\lambda$ is the width of the interval determined by the width of the intermediate slit. Figure 2.3 (b) shows the optical path of light inside the spectrometer via mirrors and gratings. In the following, for clarity not a bundle of rays is depicted but only the center beam ray. The image, which is focussed onto the entrance slit, is reflected by 90° (M1) onto a collimating mirror (M2) at distance f, confocal length, from the entrance slit. M2 reflects the light rays parallely onto the first grating (G1), which disperses the light into its spectral constituents. It should be mentioned that the rays leaving the grating are sent parallely onto M3, which could not be illustrated in the schematic and to depict the dispersion of the white light, the dispersed rays are drawn in different angles. The dispersed light is sent onto another collimating mirror (M3) and is focused as a spectrally dispersed line (a multitude of images of different wavelengths) in the plane on the intermediate

slit. The light passing the intermediate slit corresponds to the wavelength interval $[\lambda_0 - \frac{\Delta\lambda}{2}, \lambda_0 + \frac{\Delta\lambda}{2}]$.
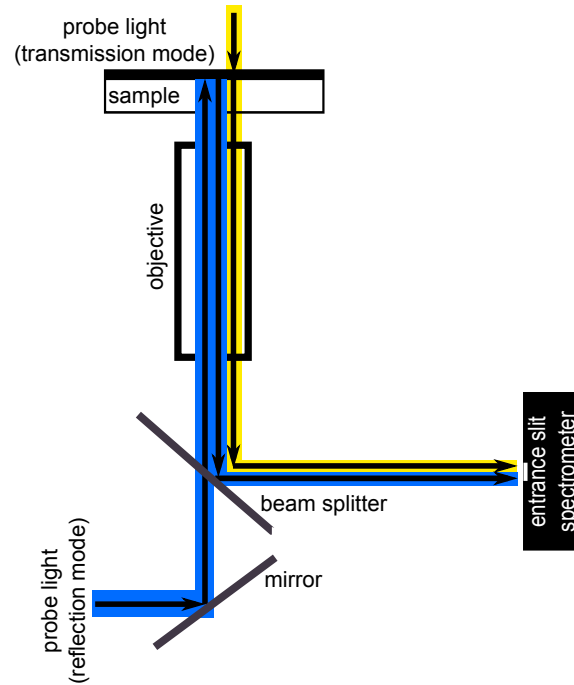
(a)
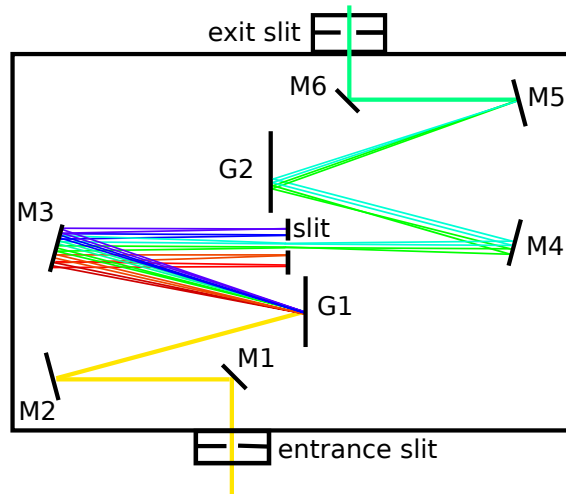
(b)

Figure 2.3: (a) Light path for transmission (yellow) and reflection (blue) mode. (b) Light path inside a subtractive double spectrometer.

As in the case of the light leaving the entrance slit, the light leaving the intermediate slit diverges again and is reflected (M4) parallely onto the second grating (G2).

The grating merges the remaining dispersed light again. M5, another collimating mirror focuses the light and after being reflected by another mirror (M6) the image is focused onto the exit slit where the CCD chip is located.

The angle of the grating position can be controlled by a stepping motor covering a spectral range of $0\,\mathrm{nm}$ to $1000\,\mathrm{nm}$. The spectrometer's gratings have $500\,\mathrm{nm}$ blaze wavelength and $300\,\mathrm{gr/mm}$. The camera employed is a 14 bit CCD, pco1400 by *pco*, with $1392\,\mathrm{px} \times 1040\,\mathrm{px}$ (1.4 megapixel), pixel size of $6.5\,\mathrm{\mu m} \times 6.5\,\mathrm{\mu m}$ and a peak quantum efficiency of 62% at $500\,\mathrm{nm}$. Motor and camera control were implemented in Labview, *National Instruments*. The program is capable of obtaining sample images at different center wavelengths λ_0 by turning the spectrometer's gratings to the desired spectral position, and time resolved images by controlling the rate of image recording. Due to 1.4 megapixel of the camera, spatial resolution is only constrained by the microscope system.

2.1.2 Electrochemical cells

Electrochemical cells for aqueous measurements, i.e. hydrogen insertion, and non-aqueous measurements, i.e. lithium insertion, were specially designed for combining electrochromic experiments and transmission spectroscopy. On the one hand, the cells needed to be small and compact in order to fit onto the micrsocope stage and, on the other hand, cells have to be large enough in order to house the three electrodes to perform good electrochemical measurements.

Hydrogen cell

The compact hydrogen cell shown in figure 2.4 (a) contains the following three electrodes: a commercial Ag/AgCl reference electrode (Driref-450, *WPI*), platinum as counter electrode and the thin film on top of a transparent conducting oxide (TCO) substrate representing the working electrode. The confined space on top of the specimen holder of the microscope system restricts the dimensions of the cell. The probe light for the transmission experiment enters the cell via a window opposite the sample position. The reference electrode is brought close to the working electrode while counter electrode and sample have an angle of $90\,^\circ$. The platinum electrode is covered by a polyether ether ketone (PEEK), an organic polymer, tube and serves as filling channel. Another PEEK channel on top of the reference electrode serves as outlet. The design of this cell was adapted from Wallys et al. who used the protoype cell for detecting potential and pH dependent photoluminescence of nanowire ensembles grown on silicon substrates [52]. All hydrogen insertion experiments were carried out inside this hydrogen cell with a $0.1\,\mathrm{M}$ H_2SO_4 in high purity water electrolyte solution bought from *Sigma-Aldrich*.
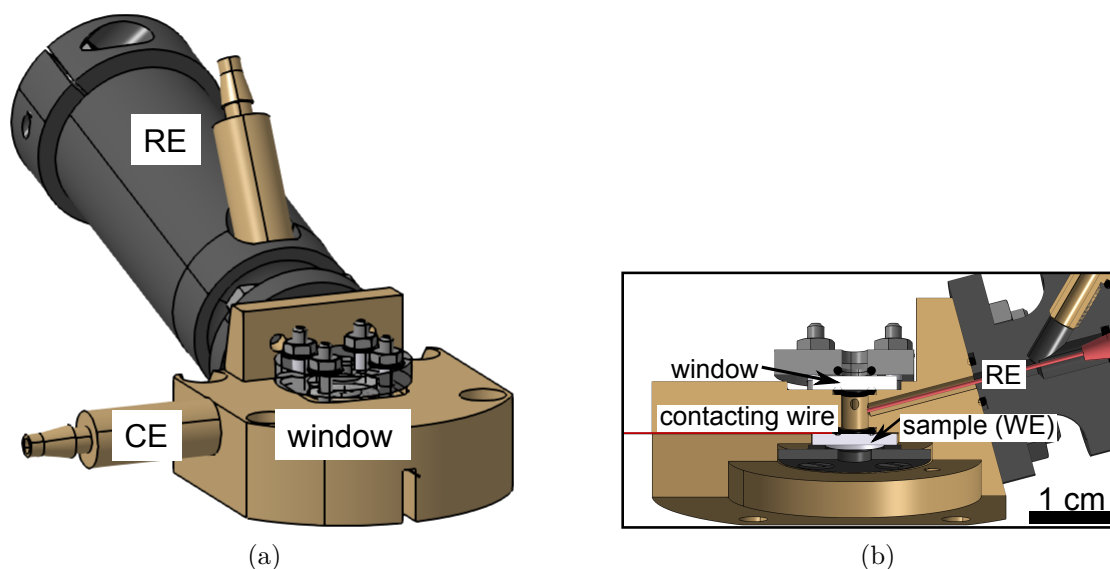
Figure 2.4: Illustration of the three-electrode electrochemical cell drawn with the software Catia V5 R21 by *Dassault Systems*. (a) Front view and (b) cross-sectional image of the cell.

Lithium cell

Inserting lithium into a WO_3 thin film and carrying out transmission spectroscopy at the same time demands a compact cell which needs to be assembled in a water and oxygen free atmosphere. A metal pin shown in figure 2.5 (a) serves as electric contact on which the sample is pressed. The probe light enters the chamber via a window opposite the sample. Stainless steel screws serve as holders of counter and reference electrode. Lithium foil attached to the screws serve as the actual electrode material. The reference electrode is located close to the working electrode. To achieve this, a channel was drilled into the bulk of the cell under an angle of 40° (relative to the screws aligned horizontally as depicted in figure 2.5(b)) so that the lithium foil could be pressed as close to the working electrode as possible without touching it. A peak at the tip of the stainless steel screw helps pushing the foil into the designated channel. The counter electrode on the other hand should be opposite the working electrode. However, as the sample itself is the working electrode and transmission measurements have to be conducted, this is not possible and the rather large counter electrode and working electrode have an angle of 90°. In order for the counter electrode to have a large lithium area, but the lithium not to come off, a hollow cylinder made of PEEK is attached to the screw's tip. The lithium inside this cylinder is firmly attached. A third screw serves as filling. All lithium insertion experiments were carried out with 0.2 M $LiClO_4$ (battery grade granulate by *Sigma Aldrich*) in propylene carbonate (PC) by *BASF*. The spectro-

electrochemical analysis can be carried out with the cell on top of the specimen holder of the optical setup introduced in section 2.1. If only time and energy resolved measurements are needed, the window and sample attachment of the cell can be modified such that optical fibers for probe and transmission light can be attached to the cell, i.e. the one end of the fiber for the probe light is connected to the light source and at the other end the detection fiber is connected to a compact *ASEQ* spectrometer. Assembling of the lithium cell was carried out in a glove box at the Institute of Physical Chemistry in the group of Professor Janek.
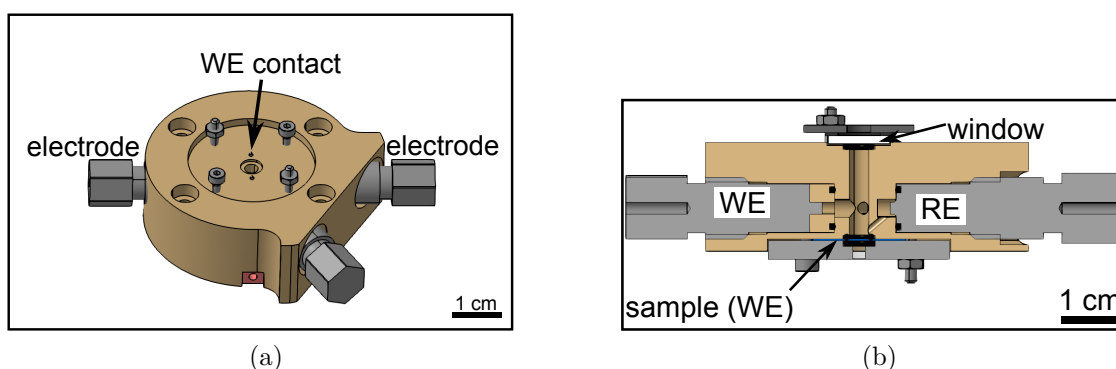
Figure 2.5: Compact three-electrode electrochemical cell for in situ transmission spectroscopy during electrochemical lithium insertion from a liquid electrolyte. (a) Front view and (b) cross-sectional image of the cell.

2.2 Sample preparation

Tungsten trioxide thin films can be deposited by various methods. I prepared samples by electron-beam evaporation and dip-coating myself and, in addition, also obtained sputtered samples prepared by other members of the institute for my experiments. While the evaporation was carried out from tungsten trioxide powder, dip-coated thin films were deposited from a solution of WCl_6 and for sputtered samples a tungsten target was employed. The crystallinity of the dip-coated samples was controlled by the calcination temperature while amorphous evaporated and sputtered films could be crystallized by heat treatment after deposition.

Sol-gel synthesis

For the synthesis of tungsten trioxide, a dark orange solution consisting of 0.68 g WCl_6 and 5 g ethanol was stirred for approx. 12 hours which resulted in a turquoise to blue gel. Additionally, a triblock-copolymer, namely Pluronic F127 was added to reduce the surface tension to enable better wettability of the substrates. WO_3 thin

films on FTO covered glass substrates (sheet resistance of $7\,\Omega/\text{sq}$) were prepared by dip-coating using a specially designed pulling device in a controlled atmosphere with relative humidity lower than $10\,\%$ and a constant withdrawal rate of $10\,\text{mm/s}$. After dip-coating, the films were dried in a furnace for at least $1\,\text{h}$ at $100\,°\text{C}$ and $12\,\text{h}$ at $300\,°\text{C}$ with a ramp of $2\,°\text{C/min}$. Calcination was carried out at different temperatures; $400\,°\text{C}$ and $450\,°\text{C}$, according to the desired texture. Dip-coating was carried out at the Institute of Physical Chemistry in the group of Professor Smarsly.

Electron-beam evaporation

Due to the high melting point of WO_3, electron-beam evaporation was used to deposit WO_3 thin films from a tungsten(VI) oxide 99.995% powder (*ChemPur GmbH*). An electron-beam evaporation system consisting of a V_e-beam electron gun system by the company *Vecco Intruments INC* was employed for deposition of amorphous WO_3 thin films. At a pressure of $p \leq 10^{-2}\,\text{Pa}$ WO_3 powder was heated inside a graphite crucible with a $100\,\text{W}$ electron-beam and evaporated with a rate of $1\,\text{nm/s}$ to a thickness of approximately $100\,\text{nm}$ on ITO and FTO covered glass substrates ($30\text{-}60\,\Omega/\text{sq}$ and $7\,\Omega/\text{sq}$ respectively). Annealing the samples at $400\,°\text{C}$ with a ramp of $100\,°\text{C/h}$ resulted in crystalline WO_3 thin films.

Sputtering

Amorphous WO_3 thin films were deposited by RF-magnetron sputtering from a W target in an atmosphere of Ar and O_2 using a SLS-400/1000 system manufactured by *Pfeiffer Vakuum*. The power was $200\,\text{W}$, and the O_2/Ar flow ratio was 2/3. The gas pressure during the sputtering process was $2.2 \cdot 10^{-2}\,\text{mbar}$ and the background pressure was $3.5 \cdot 10^{-6}\,\text{mbar}$. The film was deposited onto an FTO covered glass substrate. Annealing the samples at $400\,°\text{C}$ with a ramp of $100\,°\text{C/h}$ resulted in crystalline WO_3 thin film layers. Samples were supplied by the group of Professor Meyer.

2.3 Sample patterning for diffusion experiments

For lateral ion diffusion to occur inside the film, a concentration gradient is required. This is done by locally defining an ion reservoir of high concentration inside the film, which is spatially separated from regions of the film where the transport process shall be detected. For this purpose, the thin film is covered by another transparent electrically inert layer. By leaving only a certain area free of this protective layer, a reservoir region is defined, i.e. ions can only be transported from that area into the WO_3 film. From the reservoir they will laterally diffuse across the area of observation. Figure 2.6 illustrates the WO_3 layer covered by a transparent film with

a line as reservoir in the center. Applying an electric potential, the WO$_3$ line is inserted with ions from the liquid electrolyte, with proceeding time those ions are transported laterally through the oxide layer, which can be observed through the transparent protective layer by the blue coloration of the electrochromic film.
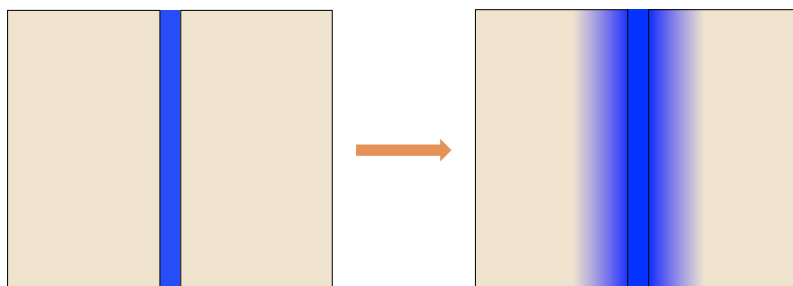
Figure 2.6: Schematic illustration of ion diffusion from an inserted WO$_3$ thin film through the electrochromic film covered by a transparent protective layer.

Electron-beam lithography

In the case of proton transport the sample may be covered by the electron-beam resist, PMMA, as protective layer as it is electrochemically stable in H$_2$SO$_4$ and electrically insulating. By controlled PMMA exposure of certain areas of the sample to the electron-beam, the desired source region can be defined. A Delta6 RC spin coater by *SÜSS* was employed to deposit 4 % PMMA in anisol by *microchem*. The resist was spinned for 45 s with 3000 rpm yielding a 400 nm thick resist layer after heating the sample for 2 min on a 180 °C hot plate. The sample was attached to the specimen holder and transferred into the specimen chamber of a *JEOL* JSM 7001F, a modified scanning electron microscope (SEM) that can be used for performing electron-beam lithography (EBL). The desired pattern was created with the exposure control program (ECP). A pattern (.pat) file of a 50 μm wide line and with a height ranging over the whole field size of 800 μm was created by the *RECT* command. This pattern was repeated with a loop inside the control (.ctl) file in one dimension in order to yield an "infinite" line. The dose of a pattern can be controlled by adjusting *increment* and *dwell time* for a given beam current and field size. In this case an increment of 2, meaning that only every 2 × 2 pixel are exposed, and a dwell time of of the beam of 3413 ps resulted in a dose of 100 μC/cm^2. At a pressure of 9·10^{-5} Pa the lithography was started with the *exposure control program* (ECP) software. Exposure beam current was 200 pA and accelerating potential 15 keV.

Photolithography

For lithium insertion another protective film has to be employed since PMMA is chemically unstable in organic solutions. A good alternative is MgO as film material, it is transparent and electrically insulating. With an appropriate photo mask the same line structure as described above can be transferred onto the sample. The positive photo resist, maP-1215 by *micro resist technology GmbH*, was spin coated with 3000 rpm for 45 s and resulted in a 1.5 µm thick resist layer. Afterwards the sample was heated for 120 s on a 100 °C hot plate. Photolithography was carried out with a maskaligner MA56 by *Karl SÜSS*, UV light of 4.6 mW/cm^2 at 365 nm and light of 7.5 mW cm^2 at 405 nm was used to expose the resist for about 12 s. After developing the resist for about 35 s in ma-D 331 the resist exhibited the inverse of the desired line pattern. With a rate of 1 nm/s about 100 nm MgO (*chempur*) was deposited by electron-beam evaporation at a pressure of $p \leq 10^{-2}$ Pa and power of 100 W. After lift-off in acetone the MgO line was formed on the electrochromic layer. This method of patterning, however, is only applicable for crystalline WO$_3$ samples since amorphous WO$_3$ is removed by the basic developer used. Another way of transferring a pattern onto amorphous tungsten trioxide thin films is by covering half of the sample by aluminum foil. Evaporation of MgO then yields a WO$_3$ thin film whose other half is covered by MgO. Diffusion can be monitored at the MgO-WO$_3$ intersection since one edge is sufficient to define gradients in ion concentration essential for the diffusion process to occur.

2.3.1 Analytical methods

Samples for ex situ XPS, XRD and UV-Vis analysis were prepared as follows: The galvanostatic lithium insertion was carried out inside a glove box using a two-electrode setup inside a cuvette with lithium foil as counter electrode. Stainless steel screws were used as electric contacts and for fixing counter electrode and sample.

X-ray photoelectron spectroscopy (XPS)

XPS measurements were performed using a PHI 5000 Versaprobe Scanning ESCA Microprobe by *Physical Electronics* equipped with a monochromatic aluminum X-ray source (beam area 200 µm × 1400 µm, X-ray power 100 W) at a chamber pressure of around 10^{-8} mbar. Pass energy for high resolution spectra was 23.5 eV and energy step width 0.1 eV. The spectra were analyzed with the CasaXPS software package (Version 2.3.17dev6.3y). The spectra were energy calibrated by shifting the binding energy of the adventitious carbon signal to a position of 284.8 eV. Measurements were carried out at the Institute of Physical Chemistry in the group of Professor Janek. The idea for in situ lithiation experiments originate from the group of Professor

Janek.

X-ray diffraction (XRD)

Structural investigations on pristine and lithium-inserted samples were carried out by X-ray diffraction (XRD), using a PANalytical Empyrean diffractometer with Cu K_α radiation ($\lambda_1 = 154.056$ pm, $\lambda_2 = 154.539$ pm, $I(\lambda_2/\lambda_1) = 0.5$) in Bragg-Brentano $\Theta - \Theta$ geometry. Diffraction diagrams were recorded in a 2Θ range from 10° to 90° with a step size of 0.013° and a counting time of 270 s per step. The average crystallite size in the thin films was calculated via *Williamson-Hall* analysis, using LaB6 powder (NIST Standard Reference Material 660B) as external standard for instrumental line broadening and omitting FTO substrate reflections. Powder samples were measured in a similar manner, but with a step size of 0.026°. Measurements were carried out at the Institute of Physical Chemistry in the group of Professor Janek.

UV-Vis spectroscopy

UV-VIS transmission spectroscopy was performed with a Perkin Elmer Lambda 900 spectrometer. The integration time was 0.16 s and the scan speed was 300 nm/s for the UV-VIS range and 375 nm/s for the NIR range with a spectral resolution of 5 nm. Measurements were carried out at the I. Physical Institute in the group of Professor Meyer.

Scanning electron microscopy (SEM)

SEM investigations were performed with a *JEOL* JSM 7001F, a modified scanning electron microscope (SEM) that can be used for performing electron-beam lithography (EBL), and on a Merlin high resolution Schottky field emission electron microscope (Zeiss SMT) equipped with an X-Max energy dispersive X-ray spectroscopy detector (*Oxford Instruments*) at the Institute of Physical Chemistry in the group of Professor Janek.

3 Results and Discussion

In this chapter results of time and spatially resolved transmission experiments on microstructured devices of electrochromic WO_3 are presented and discussed. The first part comprises the characterization of the optical microscope system introduced in chapter 2. This includes the determination of the spectral window of the bandpass and a discussion of the versatile spectroscopic applicability for photoluminescence, transmission or reflection measurements. The second part is divided into two sections, which discuss time and spatially resolved ion insertion into WO_3, respectively. Time resolved ion insertion experiments comprise insertion of hydrogen and lithium into thin films prepared by three different methods, i.e. dip-coating, sputtering and electron-beam evaporation. The correlation between coloration efficiency and chemical oxidation states is discussed in a case study of nanocrystalline dip-coated WO_3 thin films. The description and discussion of spatially resolved ion diffusion experiments on amorphous electron-beam evaporated thin films concludes this chapter.

3.1 Microscope system characterization

Different imaging modes of the microscope system were examined in order to give a proof of principle. In the case of the transmission imaging mode, a chromium-glass mask and pixels of a cellular phone were employed as test patterns. While samples deposited on top of opaque substrates were analyzed with the microscope in the reflection mode, as described in chapter 2.

3.1.1 Determination of the spectral width of the bandpass

In order to gain information about the spectral window of the bandpass realized by the subtractive double spectrometer, the light of a laser diode (635 nm) was focussed onto the entrance slit. The width of the entrance slit was 0.1 mm and the intermediate slit was 2 mm. Figure 3.1 shows the resulting spectrum of the bandpass. The center wavelength is $\lambda_0 = 637$ nm and $\Delta\lambda = \pm 15$ nm (full width at half maximum). Thus the following experiments were all carried out within the spectral window of $\lambda_0 \pm 15$ nm.
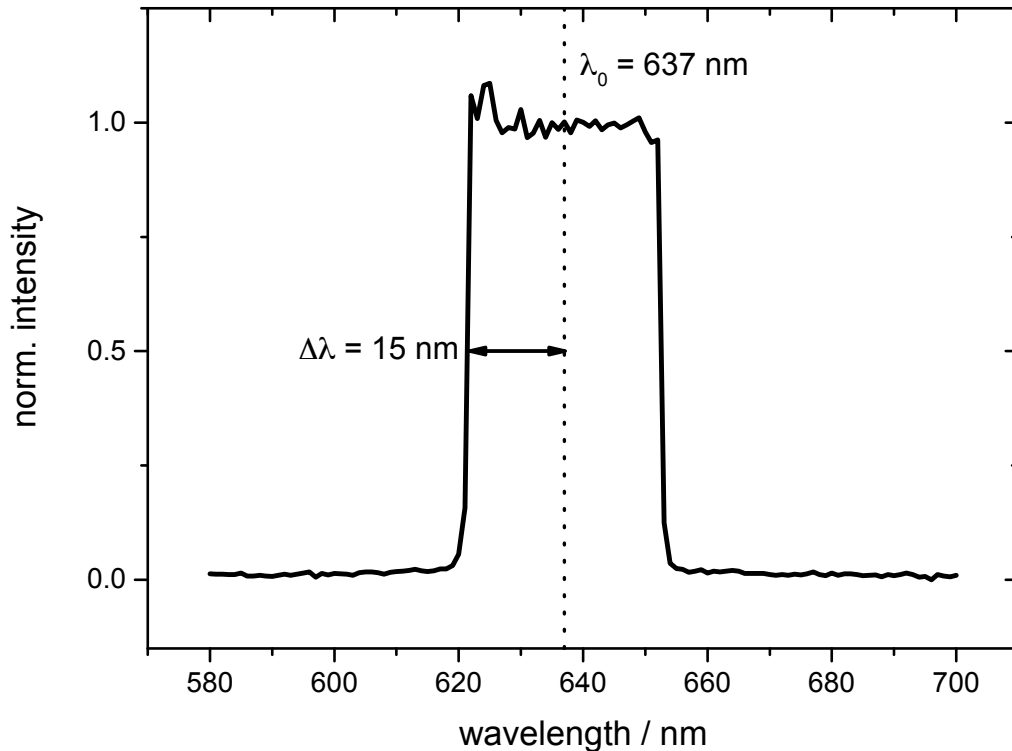
Figure 3.1: Spectrum of the bandpass realized by the subtractive double spectrom-
eter. Entrance slit: 0.1 mm, intermediate slit: 2mm and light source:
635 nm laser diode.

3.1.2 Imaging spectrally filtered by a bandpass

Photolithography was used to fabricate test samples consisting of well defined micro-
and nano structures to gain information about the upper limit of spatial resolution
of the optical system. The schematic image of a photo mask depicted in figure 3.2 (a)
shows a finger structure where line widths of the fingers decrease from 125 µm down
to 548 nm in steps of factor $^6\sqrt{2}$.

The photo mask was employed to define a corresponding chromium pattern onto a
coverslip. Figure 3.2 (b) shows the transmission image of the chromium-glass pattern
with the gratings of the spectrometer set to detection in zero order. The white light
source is a halogen white light lamp. The image is magnified with a 10 × objective.
Fingers of structures 1 - 4 are in focus. Starting with structure 5, the fingers become
blurry. The fingers of structure 6 (line width: 9 µm) are unfocused but can still be
distinguished. Thus the upper limit of spatial resolution is in the range of 9 µm.

Imaging of different types of samples was carried out for different central wave-
lengths, λ_0, of the bandpass. Imaging of samples deposited on transparent substrates
was carried out in transmission mode of the microscope. This also includes the imag-

(a)   (b)
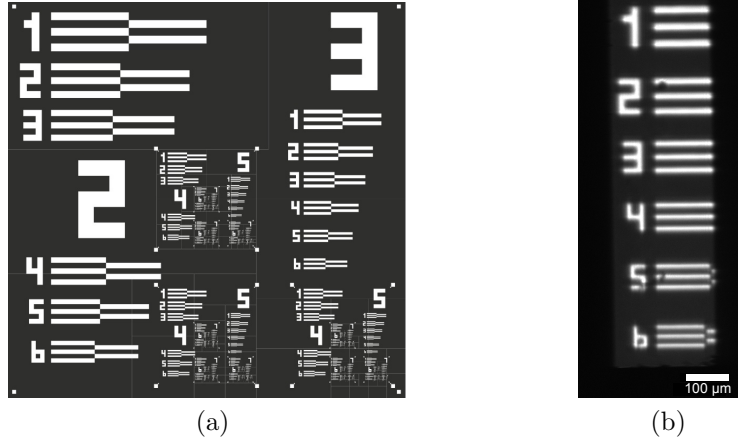
Figure 3.2: (a) Schematic image of a photo mask for the fabrication of test patterns for determining the spatial resolution of the microscope system. Finger line widths are between $125\,\mu m$ and $548\,nm$. (b) $10\times$ magnified transmission image of a chromium-glass structure illuminated by white light with the positions of the two gratings of the spectrometer set to detection in zero order.

ing of display pixels of a cellular phone at different central wavelengths λ_0, allowing one to resolve the different color pixels. Another type of transmission measurement was carried out with the glass-chromium pattern mentioned above, which was covered with a fluorescent substance. With the gratings of the spectrometer at the central wavelength λ_0 corresponding to the maximum of the fluorescence light, the light emitted by the substance could be detected avoiding effects from the excitation light. For samples deposited on top an opaque substrate, the reflection mode of the microscope was employed. Fluorescing polymer spheres were deposited on a silicon wafer. The reflection/PL image of the sample was recorded at a central wavelength λ_0 corresponding to the luminescence maximum of the spheres.

Imaging in transmission mode

White light of a cellular phone display is provided by the superposition of light emitted by three types of color pixels, red, green and blue. Figure 3.3 (a) shows the magnified image of a cellular phone displaying a white picture with the gratings of the spectrometer in zero-order position and using a $10\times$ microscope objective. Three rectangular shaped pixels of same size are distinguishable. If the position of the gratings are moved to $\lambda_0 = 450\,nm$, only the pixel at the top is discernable, the blue pixel. At $\lambda_0 = 550\,nm$ only the green pixel in the center is observable. Only the red pixel can be seen at central wavelength position of the bandpass of $\lambda_0 = 610\,nm$. This test measurement is a proof of principle of the performance of

the transmission mode of the presented microscope system in terms of spatially and spectrally resolved imaging.

(a)   (b)
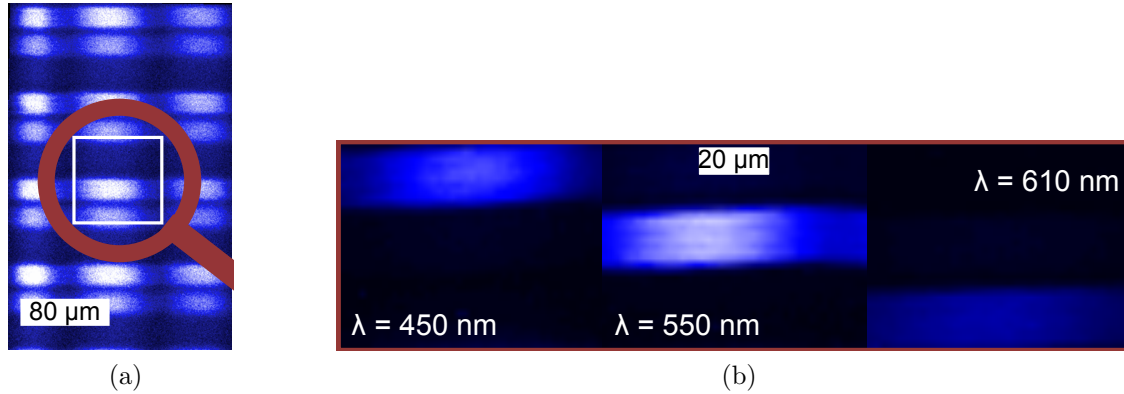
Figure 3.3: Color pixels of a cellular phone, (a) with positions of the two gratings of the spectrometer corresponding to detection in zero order and (b) spectrally filtered at 450 nm, 550 nm and 610 nm.

In another test experiment, a chromium-glass structure, as described above, was covered with the dye Rhodamine 590, which has its photoluminescence maximum at about 550 nm. Figure 3.4 shows a schematic image of the arrangement. The excitation light illuminates the fluorescent substance, which is deposited on top of the chromium-glass structure. The fluorescence light is transmitted through the glass regions yielding a fluorescence image of the chromium glass pattern. The sample was illuminated using a 405 nm laser diode. Figure 3.5 left shows the transmission image with central wavelength $\lambda_0 = 405$ nm corresponding to the excitation wavelength. As can be seen, no structure can be discerned. The image is black, i.e. no photons are detected, since the dye layer absorbs all light. When the central wavelength position is changed to $\lambda_0 = 550$ nm the structure becomes visible (figure 3.5 right) due to the fluorescence light, which is transmitted through the glass area of the structure.

Another experiment was carried out using an indium gallium nitride (InGaN) quantum dot sample. This sample was set on top of a chromium-glass structure, mentioned above. A 280 nm LED was used to illuminate the sample. Imaging was carried out at $\lambda_0 = 450$ nm, the wavelength position of the quantum dots' emission maximum. The resulting photoluminescence (PL) image is shown in figure 3.6 (a).

Imaging in reflection mode

Fluorescing polymer spheres (of 10 μm in diameter) distributed on an opaque substrate were used to test the optical system in reflection geometry. The light of a laser diode of 405 nm was placed in front of the beam splitter, according to the schematic
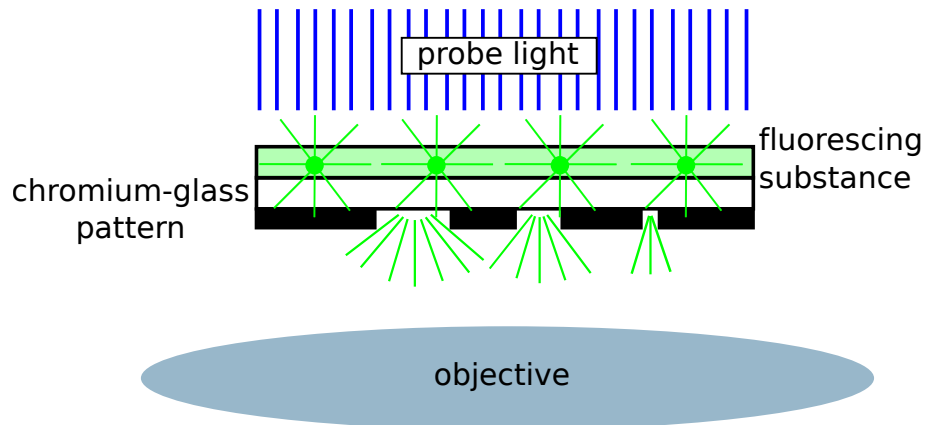
Figure 3.4: Schematic image of the arrangement for transmission imaging of a fluorescent sample set on top of a chromium/glass pattern. The probe light is absorbed by the flourescent species. The fluorescence light is transmitted by the glass regions yielding a fluorescence image of the chromium-glass pattern.

image shown in figure 2.3 (a). After being reflected and transmitted by the beam splitter and after passing the microscope objective, the laser light is focused onto the spheres and excites them. The emitted fluorescence image is collected by the same microscope objective and redirected by the beam splitter onto the entrance slit of the spectrometer, yielding an image of the sample in the plane of the entrance slit. The central position of the bandpass was set at $\lambda_0 = 500\,\mathrm{nm}$. Figure 3.6 (b) shows the fluorescence image of the polymer spheres. The image of the fluorescing spheres appears somewhat blurred. The reason is the comparatively large size of the spheres. As a consequence not the entire sphere is located in the focal plane and the parts outside the focal plane only give a blurred contribution to the image.
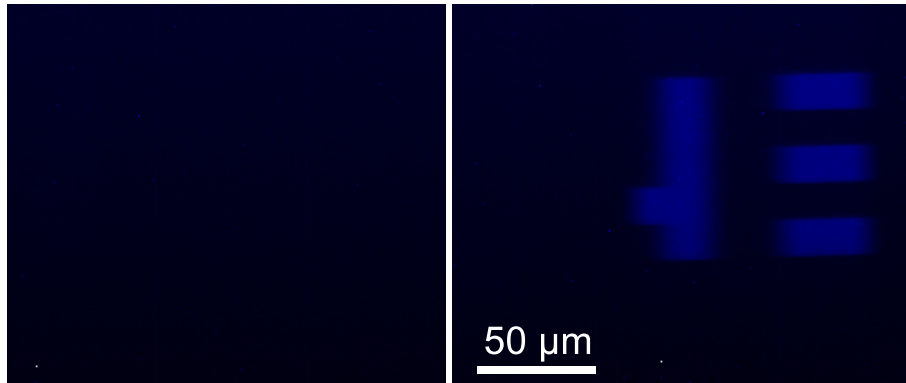
Figure 3.5: Transmission image of a chromium-glass structure covered with Rhodamine 590 dye, illuminated with a 405 nm laser diode. Left: position of the spectrometer gratings according to the central wavelength of the excitation wavelength, all light is absorbed by the dye. Right: central wavelength position of the bandpass at 550 nm, the photoluminescence maximum of Rhodamine 590. PL light makes the glass structure visible.

(a)   (b)
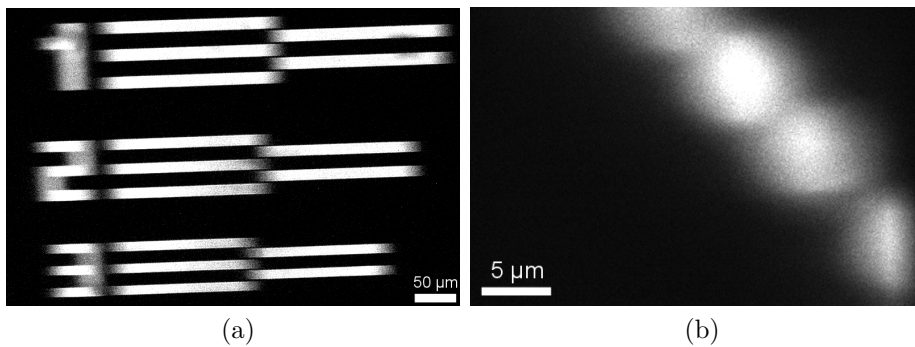
Figure 3.6: (a) Transmission image of an InGaN quantum dot sample set on top of a chromium-glass structure, illuminated with a 280 nm LED, recorded at the central wavelength of the bandpass at 450 nm. (b) Reflection image of fluorescent polymer spheres with the central wavelength of the bandpass at 500 nm.

3.1.3 Commercial imaging solutions

Commercially available imaging microscopes and spectro-electrochemical cells are what comes closest to the setup presented in this thesis. Spectro-electrochemical cells, shown in figure 3.7 (a), provide in situ electrochemical and transmission measurements. Raman imaging microscopes, schematically shown in figure 3.7 (b), provide spectrally resolved imaging.

(a)   (b)
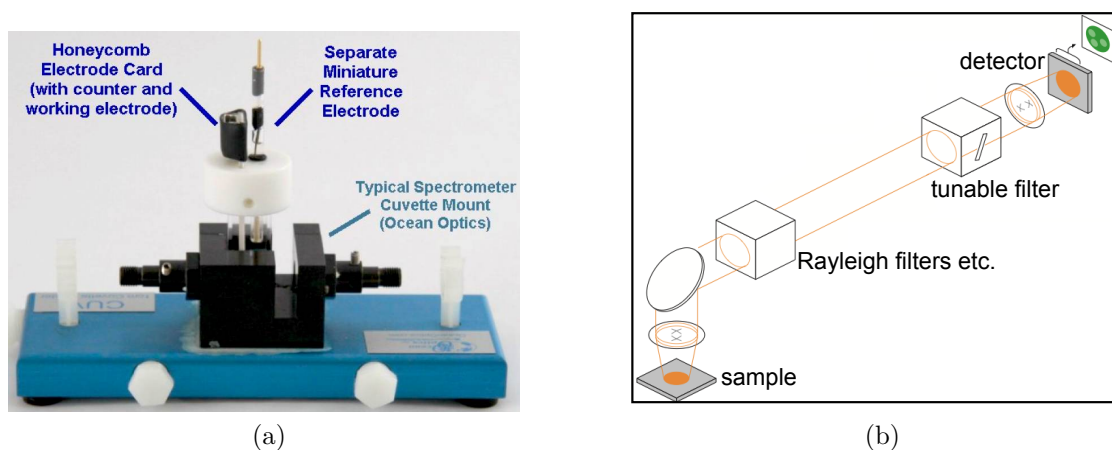
Figure 3.7: (a) Honeycomb spectro-electrochemical cell commercially available by *Pine Research Instruments* [53] (b) Schematic of a *True Raman Imaging*™ system [54].

A typical *spectro-electrochemical cell* usually consists of three electrodes inside a transparent cuvette. From one side light is sent onto the sample and from the opposite side, behind the sample, the transmitted light is collected by a compact spectrometer or a photo diode. This setup is very simple and does not provide any spatial information. The lid of the cuvette is usually not air or watertight and can only be used inside a glove box or for experiments not sensitive to water or oxygen. With a compact spectrometer a transmission spectrum in a certain wavelength range, depending on the employed detector, can be acquired. Spectral resolution is typically in the range of 0.2 nm. If the energy distribution of the transmitted light is not of interest, a photo diode, which only collects the sum of light entering the detector, can be employed.

With Raman imaging microscopes the PL or Raman-scattered light image of a sample can be recorded. *True Raman Imaging*™ by the company *Renishaw* is a commercial solution of such an imaging microscope. The spot of the laser light, which is sent through an objective onto the sample, is expanded in order to illuminate a large area of the sample. Depending on the employed objective, the disc shaped illumination area is in the µm range, however, a drawback is the inhomogeneity of

the resulting laser spot. For a $50 \times$ objective the spot is about $50\,\mu$m in diameter. The PL or Raman-scattered image is magnified by the objective and reflected onto tuneable filters. The image can then be spectrally filtered. The tuneable filters comprise a set of dielectric filters each exhibiting a narrow bandpass. The spectrally filtered image is then directly recorded by a CCD. An illustration of the schematic setup is depicted in figure 3.7 (b) [54].

The setup presented in this thesis combines the properties of an imaging microscope, i.e. spectral and spatial resolution, and of a spectro-electrochemical cell, i.e. electrochemical information. In operando measurements play an important role for the investigation of the electrochromic coloration process in WO_3, since there is much literature that presents time controlled transmission data, but essentially only provide data for very few discrete points in time. However, a quasi continuous recording of data is important for detailed analysis of kinetics especially if it can be directly correlated with spatial information. This kind of measurement is possible with the presented setup and will be introduced in section 3.3.

3.2 Thin film characterization

All samples prepared, i.e. amorphous or crystalline electron-beam evaporated or sol-gel derived tungsten trioxide thin films, were characterized by scanning electron microscopy (SEM) and X-ray diffraction (XRD). To gain additional information about the morphology inside the film and its thickness, also SEM images of the samples' cross-sections were taken. XRD measurements of tungsten trioxide powder samples were also performed as a reference for the thin film data.

3.2.1 SEM

Figure 3.8 shows SEM images for amorphous electron-beam WO_3 deposited on an ITO covered glass substrate. Figure 3.8 (a) shows an image with $10\,000 \times$ magnification. The surface of the WO_3 film in general is smooth, however, spherical bumps smaller than $100\,$nm are visible. During the evaporation process WO_3 powder particles might rise and be deposited without being evaporated. Another spot on the sample, shown in figure 3.8 (b), shows cracks in the film with typical gap widths of about $200\,$nm. Figure 3.9 (a) shows a crystalline electron-beam evaporated WO_3 thin film on an ITO covered glass substrate at $10\,000 \times$ magnification. Spherical bumps of same size and spatial distribution as for amorphous films can be seen. $100\,000 \times$ magnification reveals cracks with widths of a few nanometers in the crystalline film, which are much thinner than those in amorphous films. Figure 3.10 shows cross-sectional SEM images of amorphous and crystalline electron-beam evaporated WO_3 thin films on top of ITO covered glass. Gold was evaporated on top of the thin films for improving the electric conductivity at the specimen holder/layer interface

(a) (b)
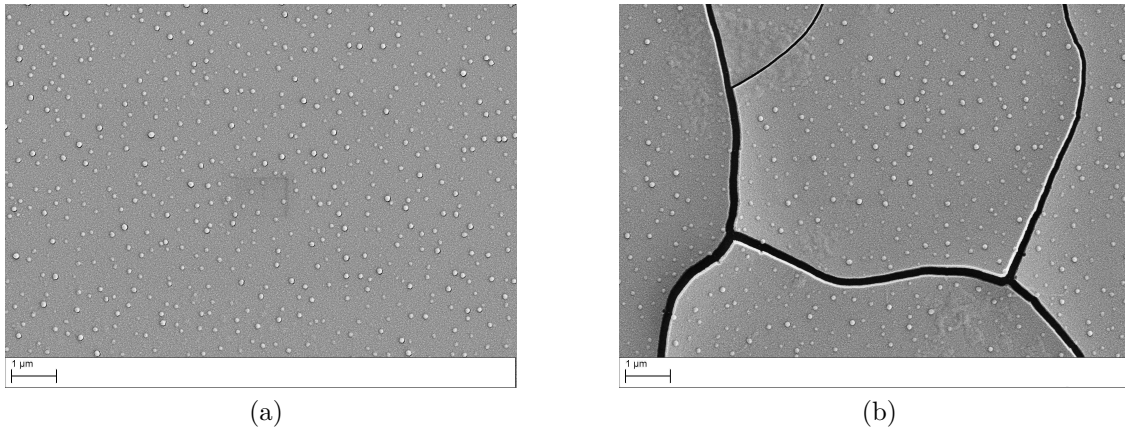
Figure 3.8: SEM image of amorphous electron-beam evaporated tungsten trioxide on top of ITO covered glass substrate.

(a) (b)
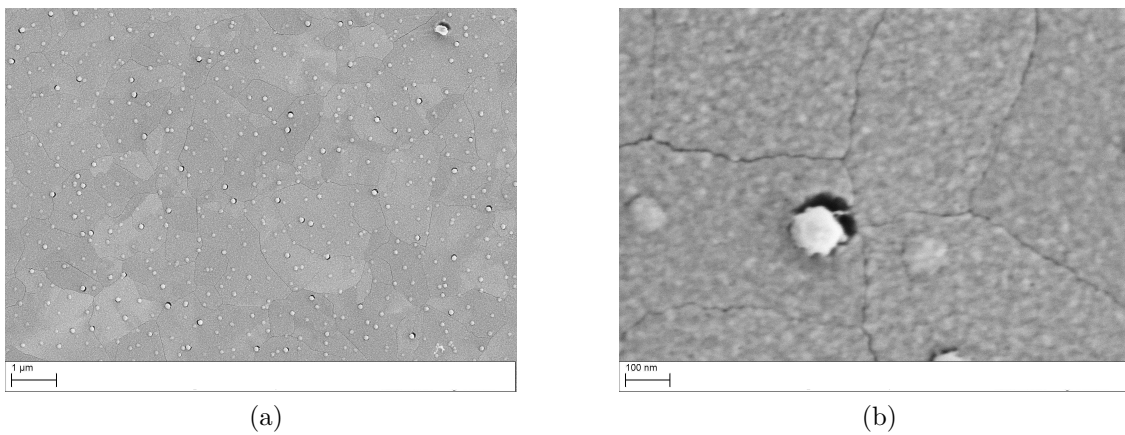
Figure 3.9: SEM images of crystalline electron-beam evaporated tungsten trioxide on top of ITO covered glass substrate.

allowing one to obtain images of higher resolution. This amorphous electron-beam evaporated sample has a film thickness of $138 \, \text{nm} \pm 3 \, \text{nm}$. Tempering at $400 \, °\text{C}$ leads to thinning of the layer, thus the corresponding crystalline electron-beam evaporated sample has a thickness of $92 \, \text{nm} \pm 7 \, \text{nm}$ only.

Figure 3.11 shows SEM images of nanocrystalline dip-coated tungsten trioxide calcinated at $450°$ at $20\,000 \times$ and $50\,000 \times$ magnification. The surface is laced with fine cracks and contains holes of up to a few tens of nanometers. A typical area circumvented by cracks has a width of about $100 \, \text{nm}$ to $200 \, \text{nm}$ while crystalline electron-beam evaporated thin films exhibit crack circumvented areas of up to $2 \, \mu\text{m}$. Cross-sectional images reveal the nanocrystalline character of dip-coated

(a) Amorphous tungsten trioxide

(b) Crystalline tungsten trioxide
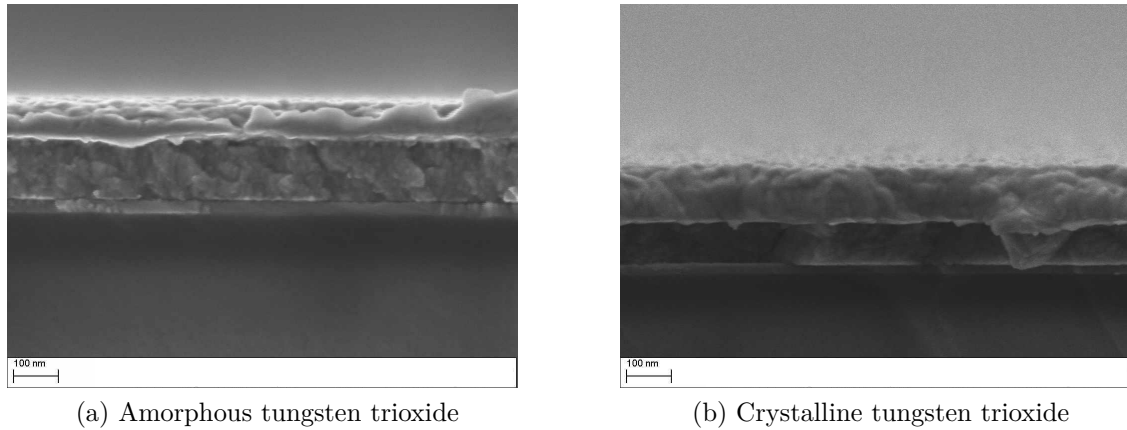
Figure 3.10: Cross-sectional SEM images of amorphous and crystalline electron-beam evaporated tungsten trioxide.

(a)

(b)
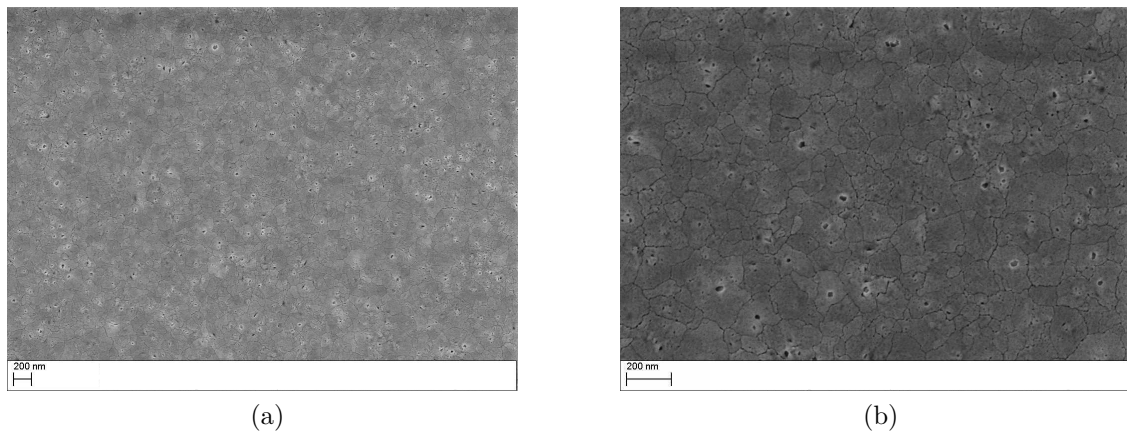
Figure 3.11: SEM images of nanocrystalline dip-coated tungsten trioxide calcinated at 450 °C.

thin films. Figure 3.12 (a) shows a cross-sectional image of amorphous dip-coated WO_3 at $100\,000\times$ magnification. As electron-beam evaporated thin films, amorphous dip-coated films are dense and do not show any cracks or pores inside the thin film. Figure 3.12 (b) shows the cross-sectional image of nanocrystalline WO_3 on top of FTO covered glass, again gold was evaporated onto the tungsten trioxide layer in order to have good electric conductivity at the specimen holder/sample interface. The film is composed of particles of a few nanometers as well as pores of about 20 nm. Film thicknesses for these thin films are $155\,\text{nm} \pm 7\,\text{nm}$ and $144\,\text{nm} \pm 23\,\text{nm}$ for amorphous and nanocrystalline dip-coated thin films respectively. The large uncertainty for dip-coated film thicknesses is due to the FTO covered glass substrate,

which is very rough yielding an uneven cross-sections after breaking the specimens.

(a) Amorphous tungsten trioxide

(b) Nanocrystalline tungsten trioxide
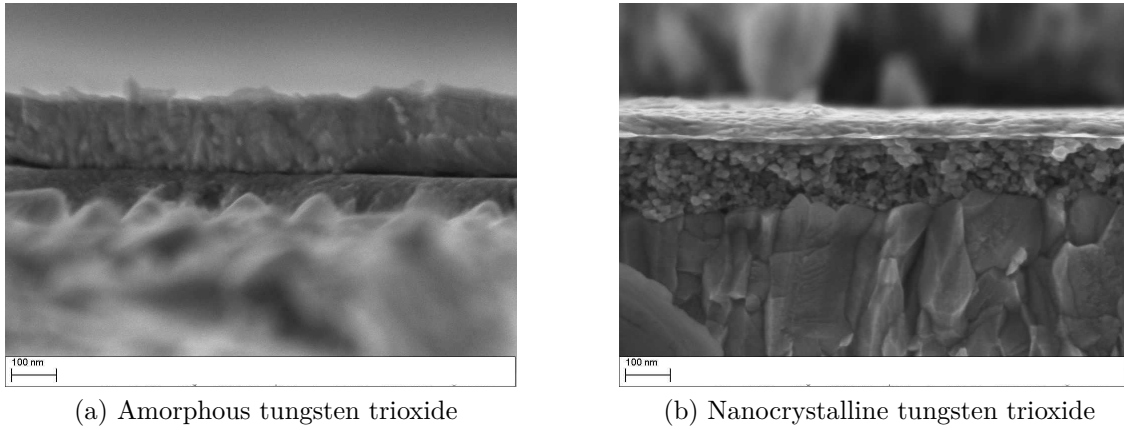
Figure 3.12: Cross-sectional SEM images of amorphous and nanocrystalline dip-coated tungsten trioxide.

Figure 3.13 shows SEM images of amorphous and crystalline (tempered at 400 °C) WO$_3$ samples sputtered by other members of the institute. The surface exhibits cauliflower like shape giving the thin film a large surface area. The florets of the amorphous sample are rough with diameters of about 80 nm to 250 nm. The crystalline florets look smoother with diameters similar to those of the amorphous thin film.

(a) Amorphous tungsten trioxide

(b) Crystalline tungsten trioxide
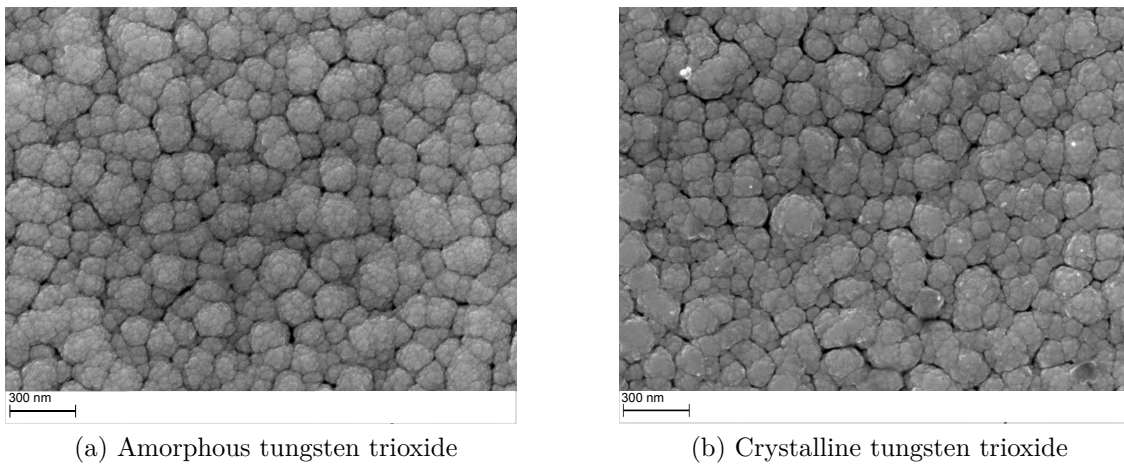
Figure 3.13: SEM images of amorphous and crystalline sputtered tungsten trioxide.

3.2.2 XRD

X-ray diffraction analysis was carried out for crystalline electron-beam evaporated WO_3 thin films deposited on a <100> silicon wafer, and for the commercial powder that was used for evaporation. Furthermore, dip-coated thin films calcinated at $450\,°C$ on FTO covered glass substrates, were analyzed. In addition, structural properties of powder samples that were synthesized from the same sol-gel derived precursor as the dip-coated samples, were analyzed.

XRD analysis of commercially available tungsten trioxide powder, as expected, resulted exclusively in reflections of monoclinic WO_3, the corresponding diffractogram is shown in figure 3.14 (a). Calculated average crystallite size (*Williamson-Hall-analysis*) is $80\,nm \pm 40\,nm$.
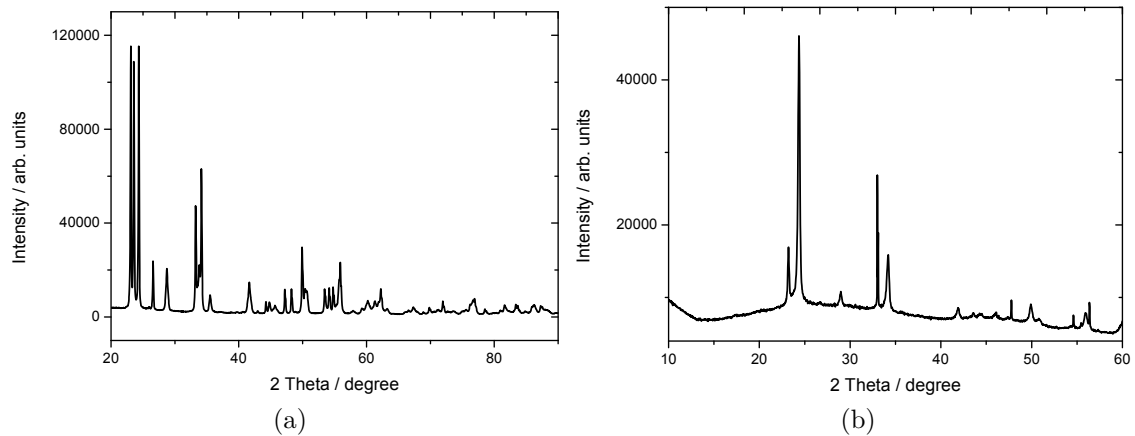
Figure 3.14: X-Ray diffraction diagrams of (a) commercial WO_3 powder and (b) a crystalline electron-beam evaporated WO_3 thin film. The highly structured background can be attributed to the Si substrate.

Electron-beam evaporation of monoclinic WO_3 powder results in amorphous thin films, which can be crystallized by subsequent heat treatment. Figure 3.14 (b) shows the diffractogram of a crystalline electron-beam evaporated thin film. Interestingly, the thin film possesses a tetragonal instead of the expected monoclinic structure after deposition. So far tungsten trioxide has been reported to have a monoclinic crystal structure at room temperature and only tends to transform into a tetragonal structure at temperatures higher than $740\,°C$ [55], or if small ions are inserted [19]. Several other groups also reported that evaporated tungsten trioxide thin films exhibit a monoclinic structure after heat treatment below $740\,°C$ [56, 57]. As neither the temperature for crystallization was above $740\,°C$ nor ions were inserted during preparation steps, the question remains which processes lead to the formation of this unusual phase during our evaporation process.

The powder synthesized from a sol-gel-derived precursor by heating at $450\,°C$,

exhibits the monoclinic crystal structure (space group $P21/c$), also found for commercially available WO_3 [58]. Despite the lower degree of crystallinity, Rietveld refinement of the diffraction diagram proves phase purity of the sample. Graphical results of the refinement are shown in figure 3.15 (a). The particular crystal structure is depicted in figure 3.16.

(a)

(b)
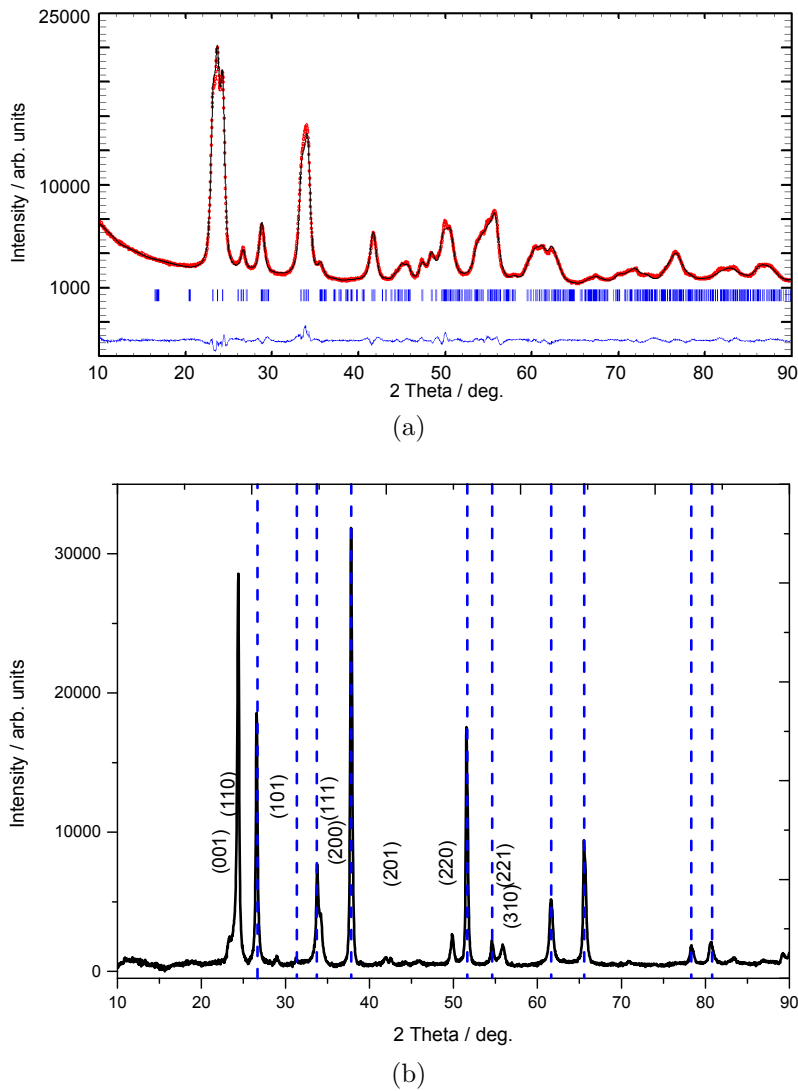
Figure 3.15: (a) Graphical results of the Rietveld refinement of WO_3 powder made from a sol-gel-derived precursor. (b) Diffractogram of a sol-gel derived WO_3 thin films calcinated at 450 °C.

Average crystallite sizes for incompletely calcinated (heated at 300 °C) powders are $7\,nm \pm 2\,nm$ and $23\,nm \pm 9\,nm$ for powders calcinated at 450 °C, which is in good agreement with results from SEM investigations. Dip-coated thin films made
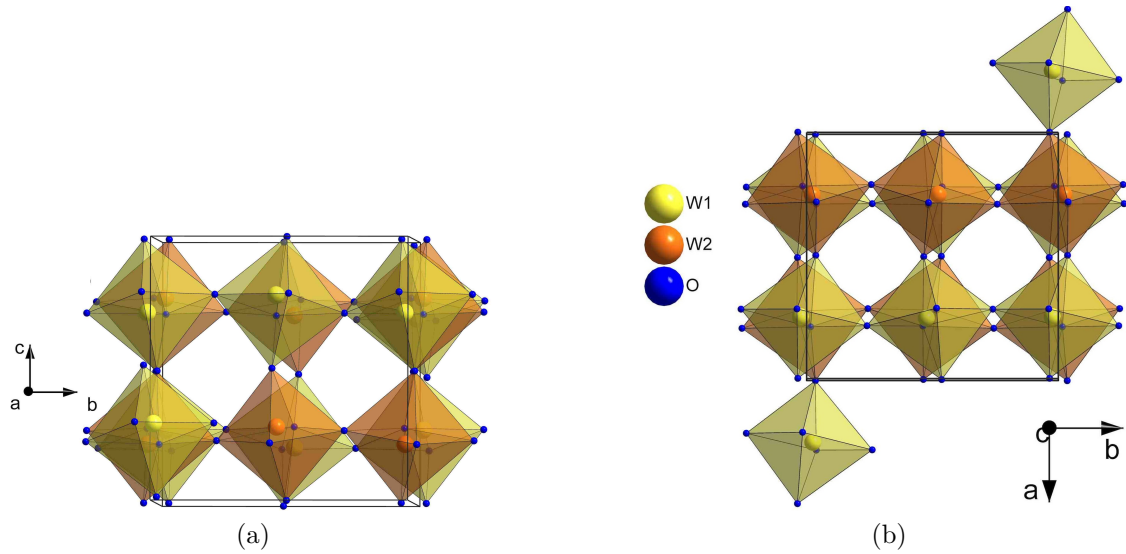
Figure 3.16: Crystal structure of monoclinic tungsten trioxide powder prepared by sol-gel derived synthesis and calcinated at 450 °C (visualized with the software *Diamond*).

from the sol-gel derived precursor, however, also show a tetragonal structure after calcination at 450 °C, posing the same question as for the evaporated thin films. The corresponding diffractogram is shown in figure 3.15 (b) along with the Miller indices, *hkl* [19]. Reflections that can be attributed to the FTO layer on the substrate, are marked by vertical blue dashed lines.

3.2.3 In situ lithiation - XPS

Chemical reduction of WO_3 can be realized by successively sputtering little amounts of lithium on top of the thin film. This kind of experiment was carried out to compare this insertion process, i.e. diffusion of lithium into the tungsten trioxide thin film, with electrochemical lithium insertion from a liquid electrolyte.

The argon ion gun, usually employed to clean the sample surface before carrying out XPS measurements, was focused on a lithium foil that was placed in the vicinity of the WO_3 thin film. Angle of the gun was 52° with respect to the surface of the lithium foil. By doing so, lithium metal was ablated and deposited on to the WO_3 film and caused chemical reduction of the material. This kind of experiment can be used to study the stability of battery materials towards lithium [59, 60]. During lithium deposition the films changed their color from transparent to a blue color as in the case of electrochromic experiments. The state of reduction can be determined by XP spectroscopy. Alternating the recording of XP spectra and the sputtering eventually give a correlation of sputter time and degree of reduction.
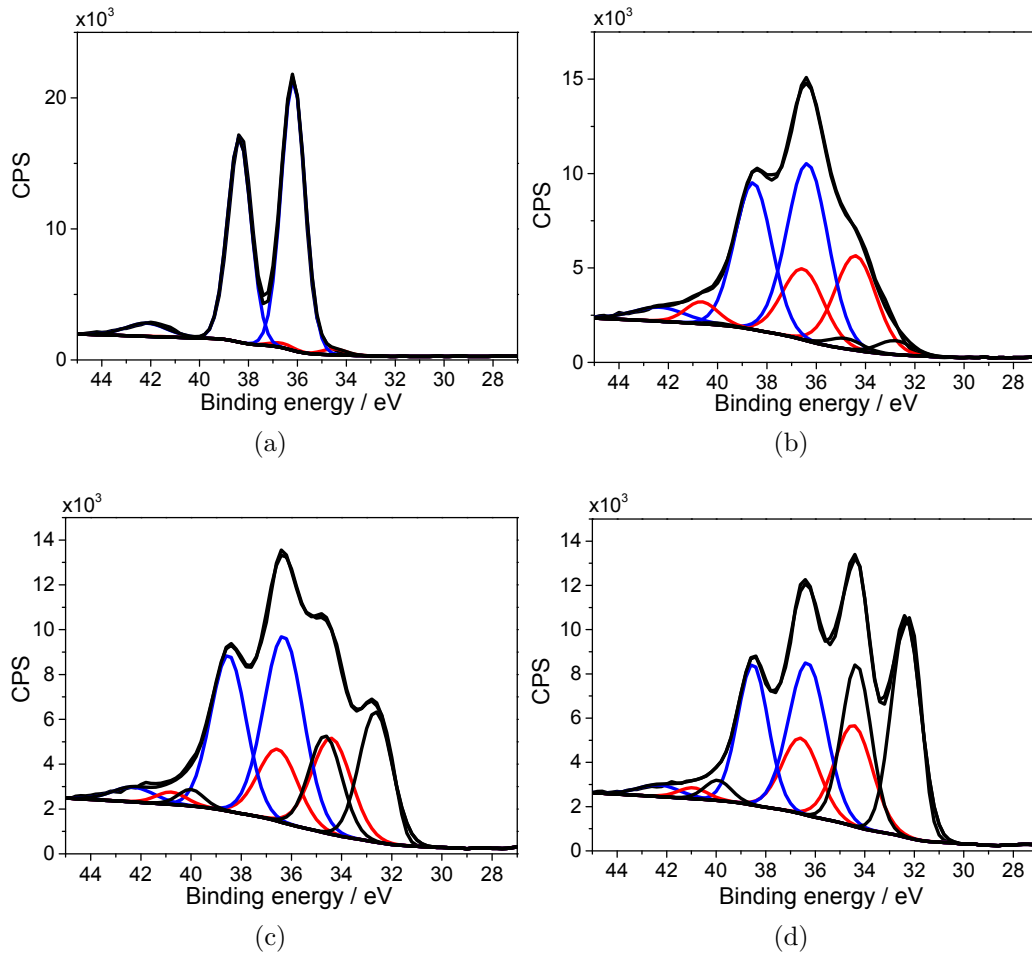
Figure 3.17: (a) XP spectrum of pristine crystalline electron-beam evaporated tungsten trioxide on top of ITO covered glass. XP spectra after (b) 600 s (c) 1200 s and (d) 1800 s lithium sputtering.

Figure 3.17 (a) shows an XP spectrum of a pristine crystalline electron-beam evaporated WO_3 thin film on top of ITO covered glass. A typical W $4f$ doublet peak, which corresponds to a pure W^{6+} oxidation peak, and the W $5p_{3/2}$ line at 42 eV can be identified [61]. Figures 3.17 (b) to 3.17 (d) show XP spectra of the thin film after 600 s, 1200 s and 1800 s total lithium sputtering time. Within the course of lithium sputtering, at first a second and third doublet developed at lower binding energies. At first glance, four peaks can be identified in the last spectrum. These peaks can indeed be fitted by three overlapping W$4f$ doublet peaks of three different oxidation states, W^{6+} of the initial state (blue curve), W^{5+} (red curve) and W^{4+} (black curve) that successively appear upon lithium deposition.

Table 3.2.3 summarizes peak positions and FWHM for each fit carried out with *Shirley background subtraction.*

Formal W oxidation state	Binding energy W $4f_{7/2}$ / eV	FWHM W $4f_{7/2}$ / eV
6^+	36.0 - 36.3	1.1 - 2.0
5^+	34.0 - 34.8	1.0 - 1.6
4^+	32.0 - 32.8	1.3 - 2.0

Peak positions of WO_3 before lithium sputtering, with $E_{BE} = 36$ eV, are in good agreement with literature [61]: $E_{BE} = 35.6$ eV, [62]: $E_{BE} = 35.7$ eV, [63]: $E_{BE} = 35.73$ eV. Reduction of tungsten trioxide by different methods, i.e. electrochemical ion insertion, ion bombardment or thermal heating, is reported by several groups and peak positions of around $E_{BE} = 34$ eV are attributed to the tungsten W^{5+} oxidation state [63, 64, 65, 66, 67]. It is also reported on the W^{4+} oxidation states, with $E_{BE} = 33$ eV, which is slightly higher than in in situ lithiation experiments [64, 65, 66]. Thus our findings are mostly in good agreement with values found in literature.
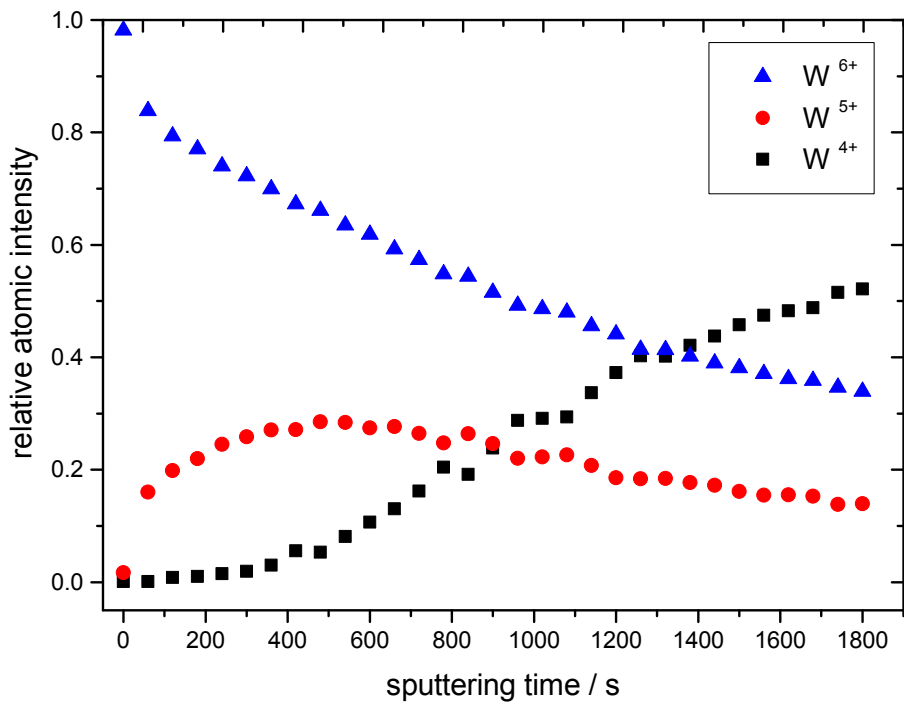
Figure 3.18: Relative amount of tungsten oxidation states in crystalline WO_3 as a function of sputtering time.

Figure 3.18 shows the relative amount of atoms that are reduced to a certain oxidation state of tungsten as a function of sputtering time. As expected, at first the amount of W^{6+} decreased and the amount of W^{5+} increased. At 400 s W^{6+}

is reduced down to a relative amount of 70% and 30% W^{5+} is formed. Then W^{4+} started to occur while the other two oxidation states, W^{6+} and W^{5+} slowly decreased until they reached 35% and 15%, respectively, at 1800 s. At 1800 s the fraction of W^{4+} is represented by 50%.

The same experiment was carried out for amorphous electron-beam evaporated WO_3. Figure 3.19 shows the relative amount of tungsten oxidation states as a function of sputtering time. As in crystalline WO_3, at first the amount of W^{6+} decreased and the amount of W^{5+} increased. At 1000 s W^{6+} is reduced down to a relative amount of 60% and 40% W^{5+} is formed. Then the W^{4+} signal rose while the amount of W^{5+} remained almost constant and the amount of W^{6+} slowly decreased. At 3600 s W^{5+} and W^{4+} exhibit relative amounts of 30% and the initial state, W^{6+}, has a relative amount of 40%.
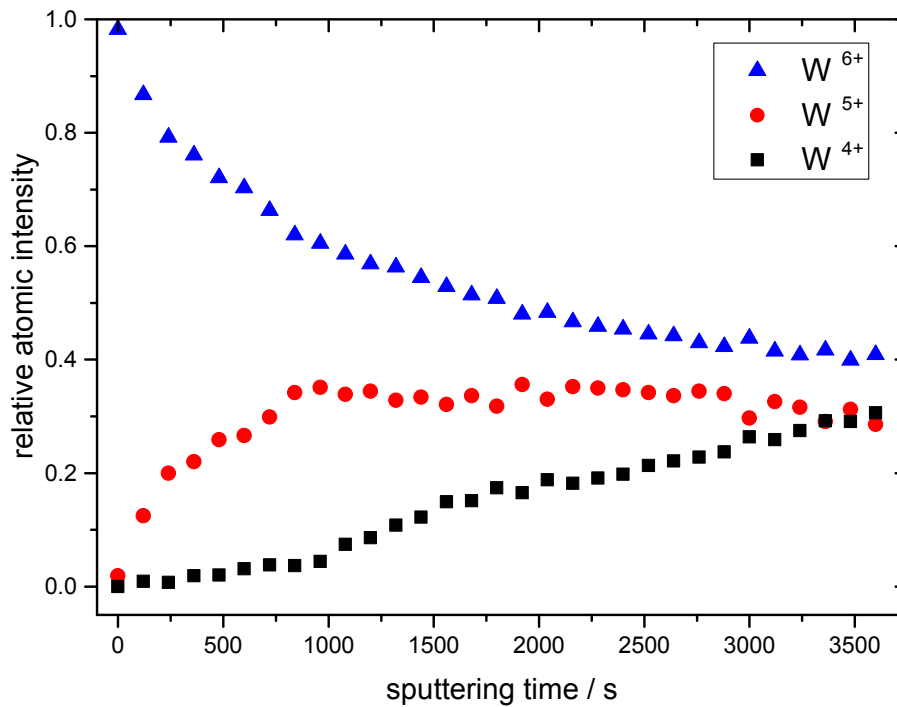
Figure 3.19: Relative amount of tungsten oxidation states in amorphous WO_3 as a function of sputtering time.

It should be mentioned that the kinetics of the formation of reduced tungsten species may not be directly compared within two in situ sputter experiments as the deposition rate of lithium is unknown. However, to obtain more detailed information about the kinetics, the amount x of deposited lithium was derived from the $W^{6+}:W^{5+}:W^{4+}$ ratio assuming that each lithium atom deposited accounts for chemical reduction. Figure 3.20 shows the deposition rate of lithium as a function of sputtering time for amorphous and crystalline WO_3, respectively.
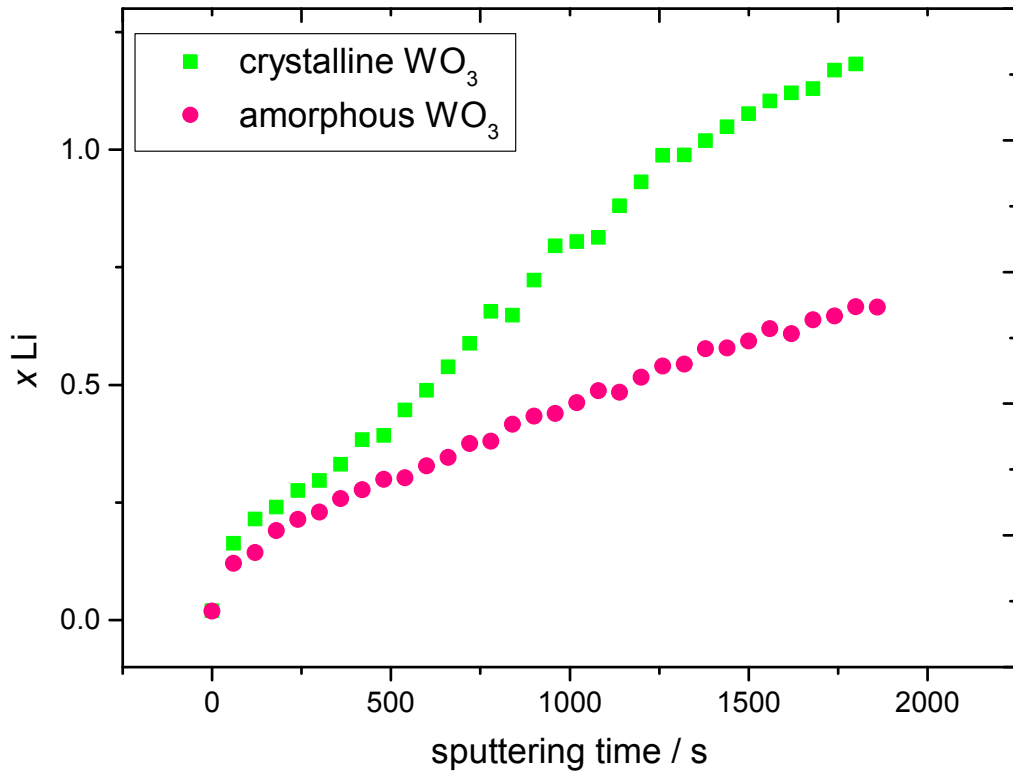
Figure 3.20: Lithium fraction x as a function of sputtering time for amorphous and crystalline Li_xWO_3.

For the first 200 s lithium deposition onto the amorphous and crystalline sample are similar. With increasing time the deposition rate onto the crystalline film seems to be much higher than that of the amorphous film. Since XPS is a surface sensitive technique, these rates are prone to error. As was shown from cross sectional SEM images, the crystalline samples are about 70% thinner than the amorphous films. Therefore the thicker amorphous film exhibits more volume for the deposited lithium to diffuse, i.e. escape the detection limit of the XPS. Also, for the experiment on the amorphous sample, the location of lithium source and the location of XP detection were farther apart than during the experiment on the crystalline sample yielding a lower effective lithium deposition rate.

Figure 3.21 shows the relative amounts of the different tungsten oxidation states as a function of x for the amorphous and crystalline sample. In this representation the similarity becomes more obvious. If the difference in deposition rates, for reasons mentioned above, is neglected, both curves are qualitatively the same: curves of W^{5+} and W^{4+} have an intersection at around $x = 0.8$ and a relative atomic intensity of ≈ 0.25 while the curve for W^{6+} exhibits a larger amount than the other two oxidation states.
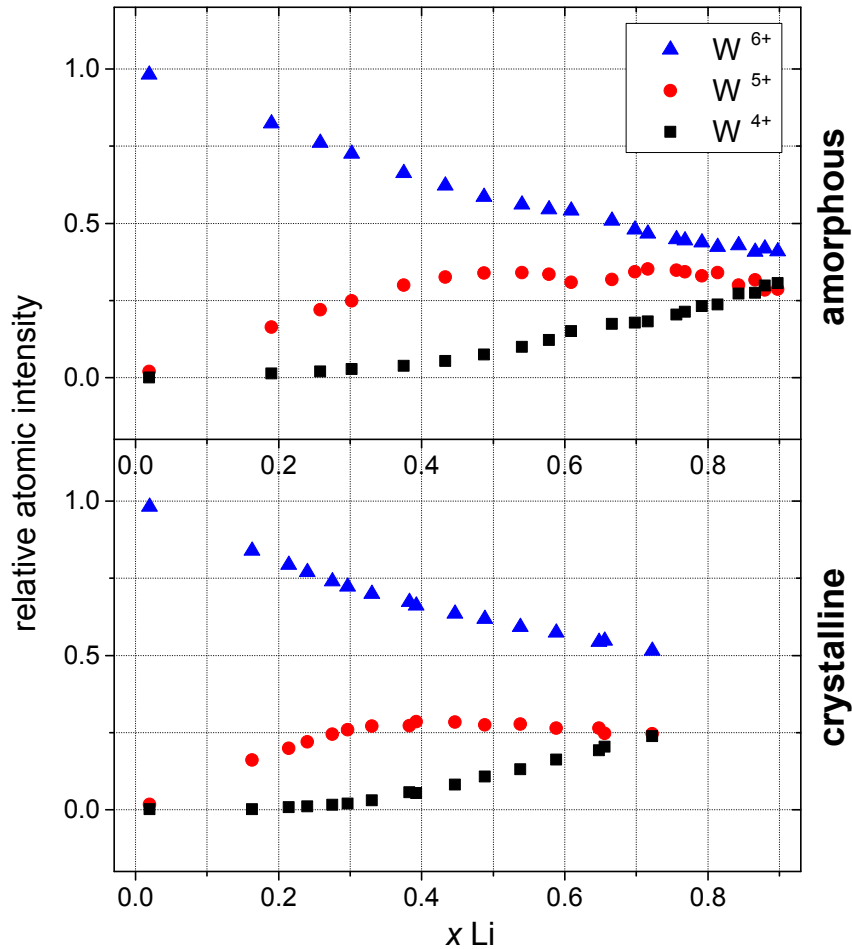
Figure 3.21: Relative atomic intensities of the different oxidation states of tungsten in amorphous and crystalline Li_xWO_3.

The in situ lithiation experiment shows that large amounts of W^{5+} as well as W^{4+} are present in Li_xWO_3. This is a first very good indication that the coloration mechanism only relying on W^{5+} does not give the full picture of the electrochromic behavior for both amorphous and crystalline WO_3.

It should be kept in mind that the chemical lithiation as presented above is only partially comparable to the electrochemical experiment. In fact it would correspond to an electrochemical lithium insertion at a potential near 0 V vs. Li/Li^+ as metallic lithium vapor is deposited on the sample surface. However, electrochemical insertion of lithium into dip-coated crystalline WO_3 studied by means of ex situ XPS, discussed in detail in section 3.3.2, show similar behavior in regard of large amounts of W^{4+} formation. The XPS measurements were carried out after the WO_3 thin film was inserted by galvanostatic discharge to certain values x of Li_xWO_3, similar to the experiments of Zhong at al. discussed in section 1.5.2. The electrochemical reduction

of nanocrystalline tungsten trioxide to a state of charge of $x = 0.49$ yielded in the formation of 50% W^{6+}, 20.4% W^{5+} and 29.6% W^{4+}.

In literature, three different transitions are proposed as reason for coloration in tungsten oxide:

1. Single polaronic transitions from W^{5+} to W^{6+} [24, 25, 68].

2. Single polaronic transitions from W^{4+} to W^{5+} [31, 69, 70] (for this transition it is proposed that W^{4+} and W^{6+} are present in the pristine film and ion insertion leads to formation of W^{5+} permitting the mentioned single polaronic transition).

3. Bipolaronic transitions from W^{4+} to W^{6+} [32] which is claimed to be more likely than a single polaronic transition.

Transition 1. surely takes place and causes a certain amount of coloration in WO_3. Section 3.3.2 will show that only a small coloration efficiency is found when W^{5+} is formed in crystalline WO_3 and a large coloration efficiency is found when W^{4+} is formed. Transition 2. is a possible transition containing W^{4+} but in contrast, in the present thesis, WO_3 with, according to XPS, only W^{6+} was employed and it was shown that both W^{4+} and W^{5+} are formed during lithium insertion. Transition 3. most likely takes place due to large amounts of W^{4+} and W^{6+}.

3.3 Time resolved measurements of hydrogen insertion

UV-Vis transmission measurements of pristine and ion inserted WO_3 show that the main transmission change takes place in a spectral range above 500 nm (figure 3.33 (b)). The highest transmission change is observed around 633 nm, therefore most WO_3 transmission experiments are carried out spectrally filtered around that position or with a laser of 633 nm wavelength providing the probe light [71, 72]. For this reason the gratings of the subtractive double spectrometer were set to a position corresponding to a central wavelength of 633 nm for all insertion experiments. Ion insertion experiments were carried out for amorphous and crystalline electron-beam evaporated, dip-coated and sputtered thin films.

3.3.1 Ion insertion into thin films of different degree of crystallinity

Hydrogen insertion into tungsten trioxide thin films were performed employing a 0.1 M H_2SO_4 in H_2O electrolyte solution. For lithium insertion an electrolyte solution of 0.2 M $LiClO_4$ in propylene carbonate (PC) was used. During cyclic voltammetric measurements the transmission was recorded. Typical OCP values after cell assembly were 0.1 V vs. Ag/AgCl and 2.8 V vs. Li/Li$^+$, respectively. Starting at the OCP, with a rate of 1 mV/s, a potential of -0.6 V vs. Ag/AgCl or 1.7 V vs. Li/Li$^+$ was applied at the sample.

Hydrogen insertion

Figure 3.22 shows the transmission data at a central wavelength $\lambda = 633$ nm as a function of electrode potential for the amorphous and crystalline tungsten trioxide thin films prepared by the different methods. The maximum transmission change for all thin films is between 20% to 30%.

The transmission curve of an amorphous electron-beam evaporated thin film displays very steep coloring and bleaching characteristics, i.e. the coloration/bleaching process takes place within a narrow electrode potential range of 0 V vs. Ag/AgCl and -0.6 V vs. Ag/AgCl. The difference of transmission characteristics between the amorphous and a corresponding crystalline thin film is very large. The transmission change for the amorphous film is about 25% while the crystalline film exhibits merely a 15 % change. And while the change of transmission of the amorphous thin film takes place in a very narrow potential range, that of the crystalline thin film requires a rather broad potential range. Unlike the amorphous film, the crystalline film does not attain its initial transmission value at the upper end of the CV, $E_{\lambda 2} = 1$ V vs. Ag/AgCl.
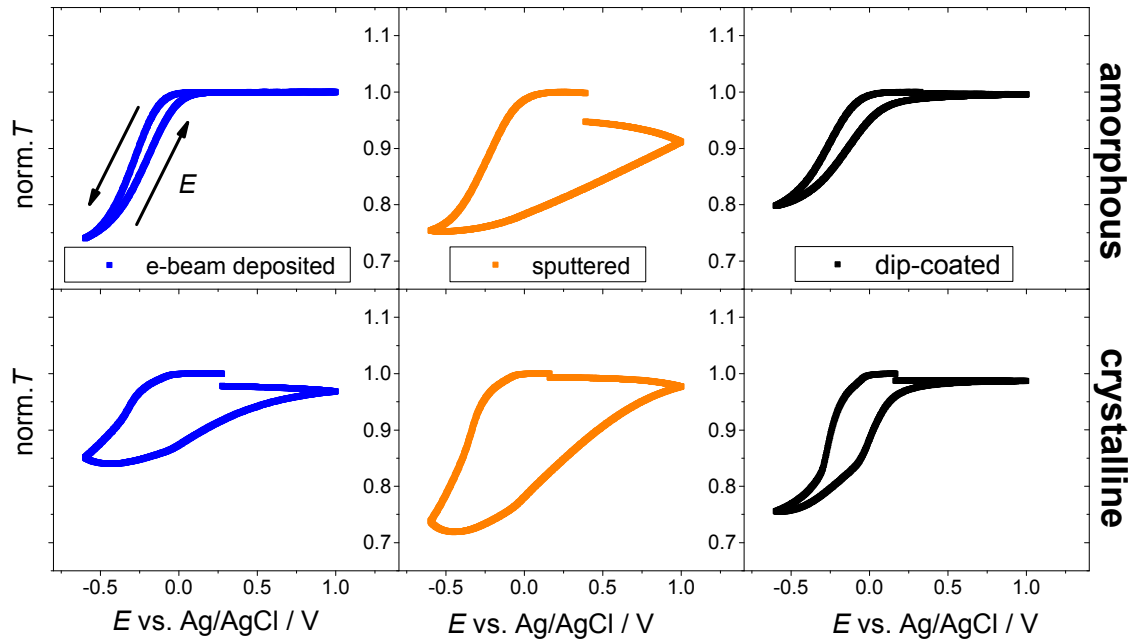
Figure 3.22: Transmission course for amorphous and crystalline tungsten trioxide thin films during electrochemical hydrogen insertion/extraction.

In contrast the amorphous sputtered thin film shows a steep coloring but a very shallow bleaching process and at $E_{\lambda 2} = 1\,\mathrm{V}$ vs. Ag/AgCl the film does not attain its former transmission value. The corresponding crystalline film exhibits similar transmission properties. However, unlike the corresponding amorphous film, the crystalline film almost attains its initial transmission value at the upper end of the CV.

The amorphous dip-coated thin film also shows similar characteristics as its crystalline counter part. The amorphous transmission curve is shallower than the crystalline curve and is somewhat similar to the curve of the amorphous electron-beam evaporated film. The curve of the crystalline dip-coated film exhibits slightly broader hysteresis and almost attains its initial transmission value at $E_{\lambda 2} = 1\,\mathrm{V}$ vs. Ag/AgCl.

Figure 3.23 and 3.24 show the differential transmission change in time, $\mathrm{d}T/\mathrm{d}t$, as a function of electrode potential and the corresponding CV for amorphous and crystalline $\mathrm{WO_3}$ thin films respectively. Here one can easily see that all the CVs strongly deviate from an ideal electrochemical process as described in section 1.5.1. No clear peaks for reduction and oxidation can be assigned. For this analysis data of one cycle starting at $E_{\lambda 2} = 1\,\mathrm{V}$ vs. Ag/AgCl, were employed.
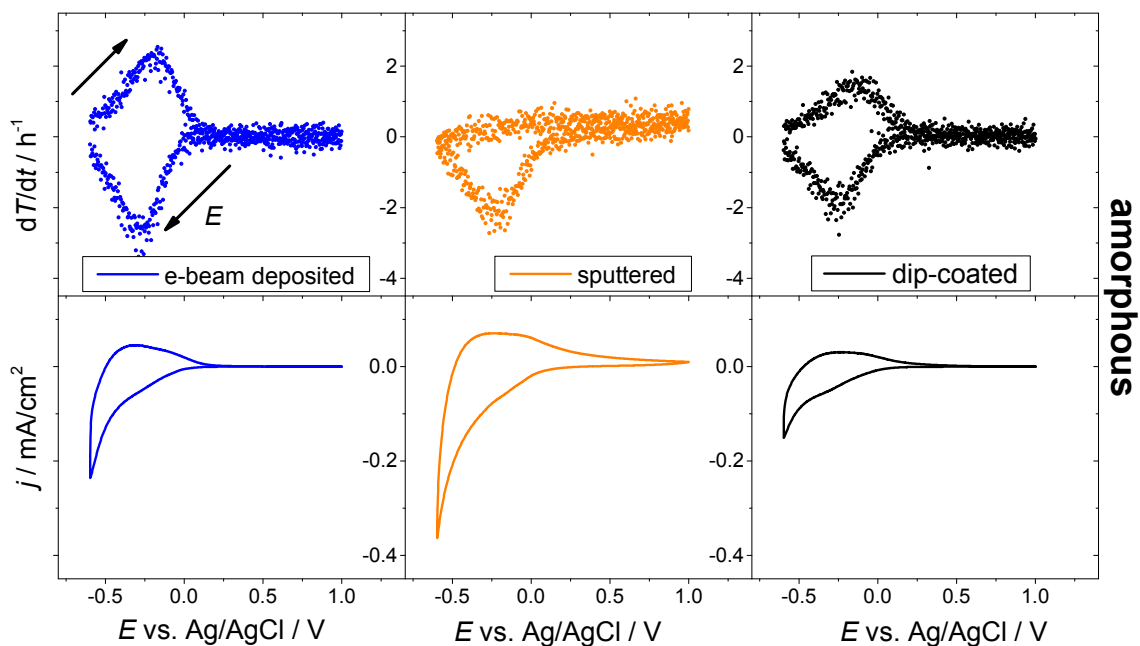
Figure 3.23: Differential transmission change dT/dt as a function of electrode potential for amorphous tungsten trioxide thin films during electrochemical hydrogen insertion/extraction and the corresponding CVs.
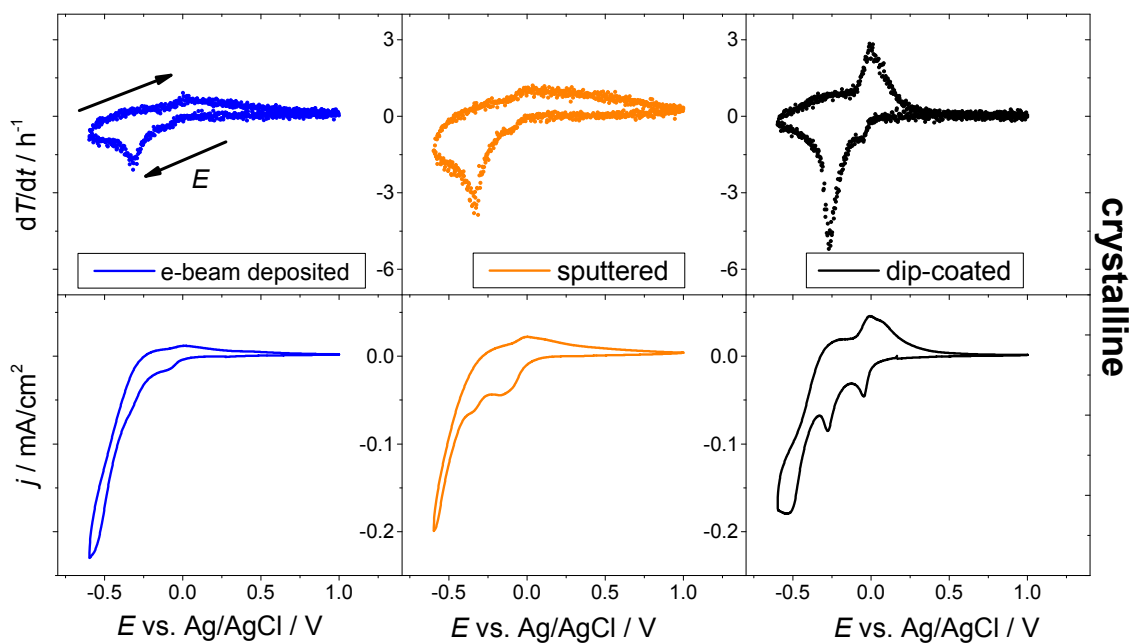
Figure 3.24: Differential transmission change dT/dt as a function of electrode potential for crystalline tungsten trioxide thin films during electrochemical hydrogen insertion/extraction and the corresponding CVs.

From the CV of the amorphous electron-beam evaporated thin film it can be seen that no current flows in the range of about 1 V vs. Ag/AgCl to 0 V vs. Ag/AgCl and no transmission change is observed for that range in the dT/dt curve. At around 0 V vs. Ag/AgCl electrochemical reduction starts, which is indicated by a negative current, and at the same time the change in transmission begins to occur, i.e negative values for dT/dt. When the polarity is changed, as soon as tungsten is oxidized, positive currents flow and positive values for dT/dt are also observed. For both, electrochemical reduction and oxidation broad dT/dt peaks are observed.

A very similar behavior is observed for the amorphous dip-coated film, but both, the electric current and the dT/dt values are smaller. The sputtered samples show a slightly different behavior. Especially the bleaching (positive currents) takes place over the whole potential range. No dT/dt peak is observed for positive currents, meaning that the potential applied to the electrode might be too low to completely bleach the sample.

All amorphous thin films show almost symmetric rhombic or triangular shaped dT/dt curves, whereas the curves of the crystalline thin films display rather asymmetric shapes. And while the CVs of the amorphous films are crooked and broad, the CVs of the crystalline counter parts are very pointed and show two distinct reduction peaks, which are most pronounced for the dip-coated thin film. For all samples at very low potentials the reductive current is maximal. However, the change in transmission tends to zero. This shows that additional reactions other than hydrogen insertion into WO_3 may take place.

To further analyze the correlations between transmission change, applied potential and the amount of inserted charge, dT/dE and dT/dQ are plotted as a function of electrode potential, E, in the potential range of $E_{\lambda 2} = 1$ V vs. Ag/AgCl down to $E_{\lambda 1} = -0.6$ V vs. Ag/AgCl, i.e. the range where the bleached thin film is colored due to successive ion insertion. Figure 3.25 shows dT/dE as a function of electrode potential for all amorphous samples and figure 3.26 for all crystalline thin films.

All samples exhibit distinct dT/dE peaks implying that the coloration is most efficient in a specific potential range. For amorphous thin films a dT/dE peak extends from about 0 V vs. Ag/AgCl to -0.6 V vs. Ag/AgCl with a peak position of about $E = -0.3$ V vs. Ag/AgCl and values between 0.5 V^{-1} and 1.0 V^{-1}. This means that the coloration gradually takes place over this broad potential range.

Crystalline thin films, however, display an additional peak at higher electrode potentials. The first peak, at around $E = -0.05$ V vs. Ag/AgCl, with a value of about 0.3 V^{-1} is much smaller than the main peak, at around $E = -0.3$ V vs. Ag/AgCl, with values between 0.7 V^{-1} and 1.5 V^{-1}. Sputtered and dip-coated samples display a very narrow and high second peak. This means that unlike amorphous thin films, crystalline thin films display a quick and efficient coloration for a small potential range.
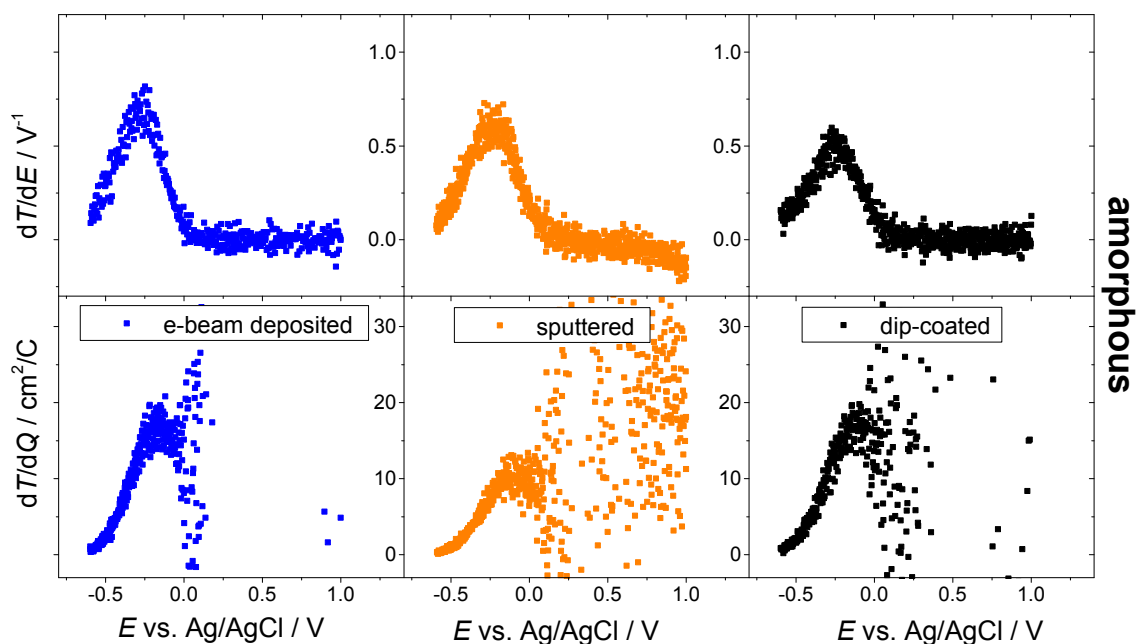
Figure 3.25: Differential transmission change $\mathrm{d}T/\mathrm{d}E$ and coloration efficiency $\mathrm{d}T/\mathrm{d}Q$ as a function of electrode potential for all amorphous thin films during the coloration process.
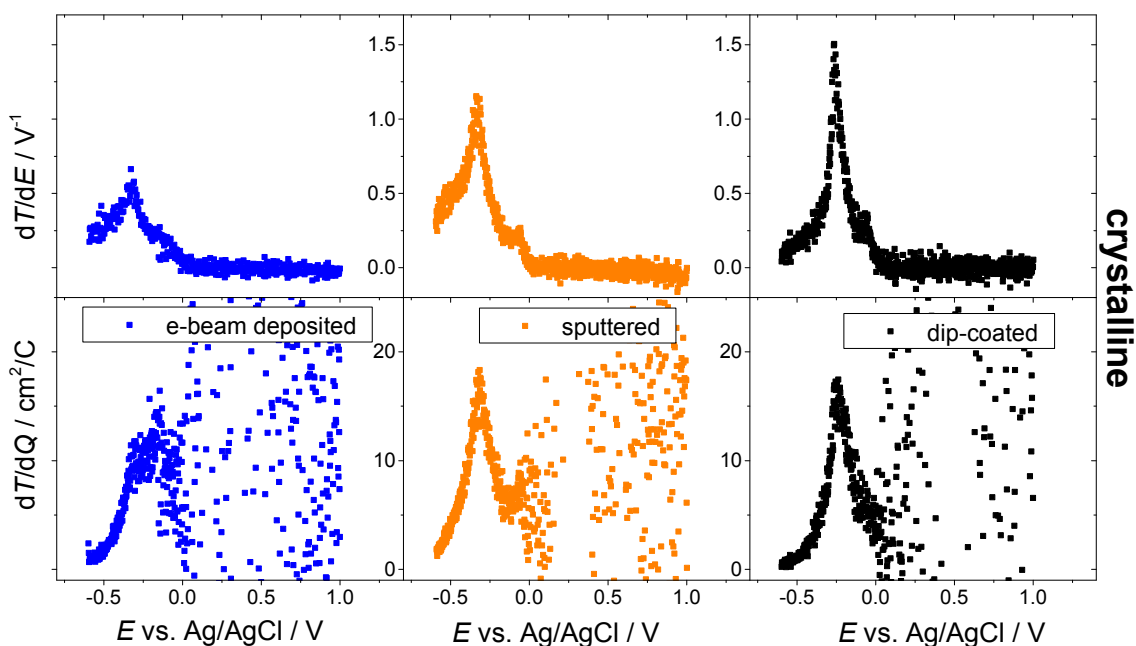
Figure 3.26: Differential transmission change $\mathrm{d}T/\mathrm{d}E$ and coloration efficiency $\mathrm{d}T/\mathrm{d}Q$ as a function of electrode potential for all crystalline thin films during the coloration process.

Interestingly, amorphous electron-beam evaporated thin films show the highest $\mathrm{d}T/\mathrm{d}E$ values of all analyzed amorphous thin films, while dip-coated thin films exhibit the lowest value. A reversed observation is made for crystalline samples, i.e. crystalline electron-beam evaporated thin films have a very broad $\mathrm{d}T/\mathrm{d}E$ peak with a mere value of about $0.5\,\mathrm{V}^{-1}$ and dip-coated samples have a $\mathrm{d}T/\mathrm{d}E$ value of about $1.5\,\mathrm{V}^{-1}$.

While $\mathrm{d}T/\mathrm{d}E$ values differ strongly for each type of thin film, the coloration efficiency of each type of sample exhibits a $\mathrm{d}T/\mathrm{d}Q$ value of $15\,\mathrm{to}\,20\,\mathrm{cm}^2\mathrm{C}^{-1}$. The peak shape for curves of the amorphous samples is again rounded at the peak while crystalline thin films, except that of the electron-beam evaporated samples, show curves of triangular shape. The positions of the $\mathrm{d}T/\mathrm{d}Q$ peaks agree with the $\mathrm{d}T/\mathrm{d}E$ peak positions. At the $\mathrm{d}T/\mathrm{d}E$ peak at higher potentials of the crystalline samples, it is hardly possible to also discern a $\mathrm{d}T/\mathrm{d}Q$ peak since the data scatter very strongly within this potential range due to fluctuations of the values of Q close to zero. The lowest value for coloration efficiency $\mathrm{d}T/\mathrm{d}Q$ is found for amorphous sputtered and crystalline electron-beam evaporated thin films with values of around $15\,\mathrm{cm}^2\mathrm{C}^{-1}$.

Lithium insertion

The green curve in figure 3.29 shows the CV of an ITO covered glass substrate. As can be seen from the high current values of the CV, electrochemical ion insertion in an aqueous environment comes along with side reactions. Besides substrate reduction, which leads to aging of the electrodes, other side reaction such as self-bleaching, which will be discussed in more detail in section 3.3.3, lead to current-free discoloration of the film in aqueous electrolytes. In order to avoid these effects similar measurements with lithium ions, using a non-aqueous electrolyte and an oxygen and water free environment, were carried out.

Figure 3.27 and 3.28 show the differential transmission change $\mathrm{d}T/\mathrm{d}E$ as a function of electrode potential and the corresponding CVs for several cycles for all measured amorphous and crystalline thin films respectively. Smoothed and raw data for $\mathrm{d}T/\mathrm{d}E$ curves are shown in one graph. As for hydrogen insertion, $\mathrm{d}T/\mathrm{d}E$ curves for lithium insertion into tungsten trioxide show that coloration is most efficient for a specific electrode potential range. All $\mathrm{d}T/\mathrm{d}E$ peaks extend from $2\,\mathrm{V}$ to $3\,\mathrm{V}$ while crystalline dip-coated samples exhibit the narrowest and highest peaks, thus having the fastest and most efficient coloration.

For amorphous thin films values of $\mathrm{d}T/\mathrm{d}E$ peaks are in the range of $0.5\,\mathrm{V}^{-1}$ to $0.75\,\mathrm{V}^{-1}$, with sputtered samples exhibiting the lowest peak value $\mathrm{d}T/\mathrm{d}E = 0.5\,\mathrm{V}^{-1}$ and electron-beam evaporated and dip-coated samples both having a value of about $\mathrm{d}T/\mathrm{d}E = 0.75\,\mathrm{V}^{-1}$.
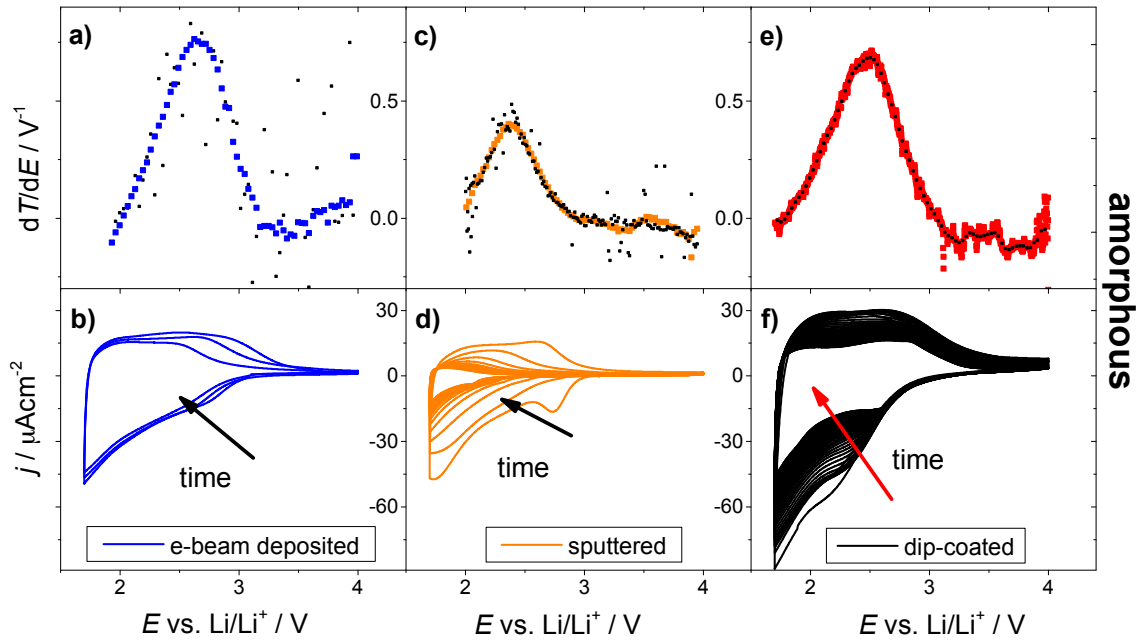
Figure 3.27: Differential transmission change $\mathrm{d}T/\mathrm{d}E$ and the corresponding CVs as a function of electrode potential for all analyzed amorphous thin films during the electrochemical lithium insertion/extraction.
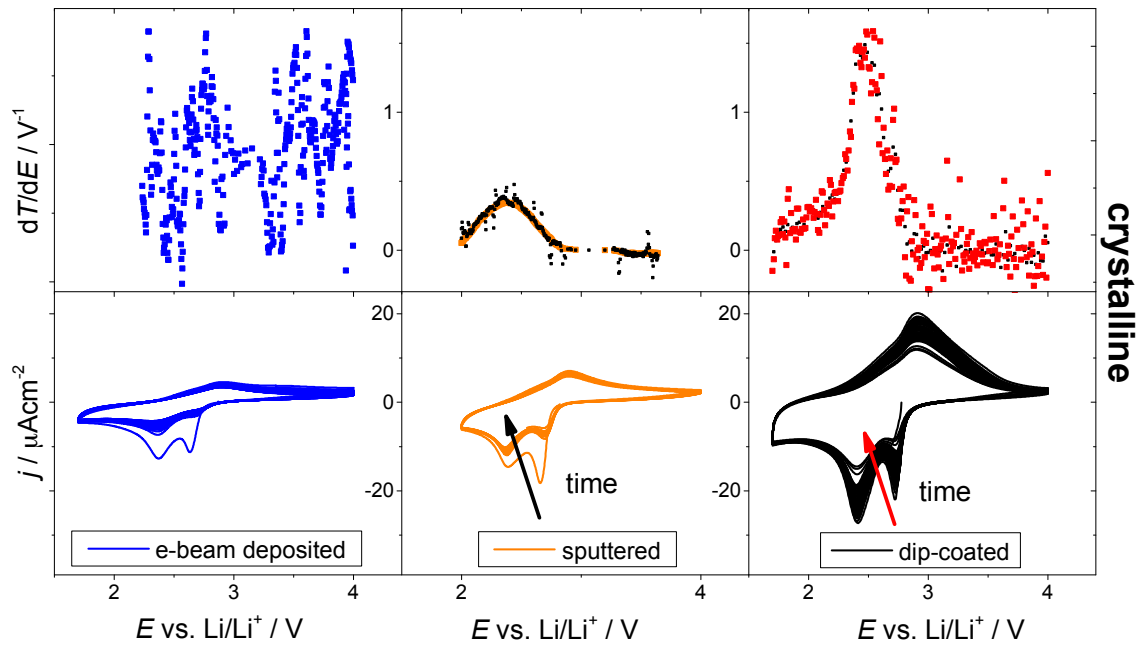
Figure 3.28: Differential transmission change $\mathrm{d}T/\mathrm{d}E$ and the corresponding CVs as a function of electrode potential for all crystalline thin films during the electrochemical lithium insertion/extraction.

For crystalline electron-beam evaporated samples, the $\mathrm{d}T/\mathrm{d}E$ peak for hydrogen insertion (figure 3.26) is very low and is even lower for lithium insertion so that it cannot be discerned. The curve for the crystalline sputtered lithium inserted sample (figure 3.28) looks more like a curve for an amorphous thin film, a rounded tip and the $\mathrm{d}T/\mathrm{d}E$ peak extending over a wide range. However, with a value of the $\mathrm{d}T/\mathrm{d}E$ peak of $0.5\,\mathrm{V}^{-1}$ the peak is even lower than that of an amorphous hydrogen inserted thin film (figure 3.25). With a $\mathrm{d}T/\mathrm{d}E$ peak value of $1.5\,\mathrm{V}^{-1}$ the dip-coated crystalline thin film reaches the same value as the corresponding hydrogen inserted sample. The width of the $\mathrm{d}T/\mathrm{d}E$ peak for hydrogen insertion, however, is much narrower than for lithium insertion.

For lithium insertion all CVs display current densities which are by a factor of 10 lower than for hydrogen insertion while exhibiting the same $\mathrm{d}T/\mathrm{d}E$ values. This means that the coloration efficiency of WO_3 for lithium insertion is significantly larger than for hydrogen insertion. $\mathrm{d}T/\mathrm{d}Q$ values could not be obtained for lithium insertion measurements since the spectrometer, employed for measurements inside the glove box, yielded too noisy transmission data.

CVs for amorphous samples show a similar form as for hydrogen insertion, however, without the high peak for low potentials. For crystalline samples the reduction current peaks as well as the $\mathrm{d}T/\mathrm{d}E$ peaks are much narrower and more pronounced in the case of hydrogen insertion. This shows that the kinetics of hydrogen insertion are much faster, as already mentioned in section 1.4. The diffusion coefficient for H^+ in WO_3 is orders of magnitudes larger than for Li.

While current densities for amorphous films are in the range of $30\,\mathrm{\mu A/cm^2}$ to $-60\,\mathrm{\mu A/cm^2}$, current densities of crystalline thin films range from $20\,\mathrm{\mu A/cm^2}$ to $-25\,\mathrm{\mu A/cm^2}$, exhibiting two reduction peaks at around $E = 2.8\,\mathrm{V}$ and $E = 2.4\,\mathrm{V}$. CVs of dip-coated samples display the highest current densities, the lowest are observed for electron-beam evaporated thin films. An additional $\mathrm{d}T/\mathrm{d}E$ peak, at higher electrode potentials, can only be discerned for crystalline dip-coated thin films. After several cycles current densities of most thin films are decreased, which shows that the films do not exhibit long term stability. However, crystalline sputtered and electron-beam evaporated thin films show a difference in the first cycle and then remain constant during all cycles, i.e. they exhibit good long term stability.

With the setup presented in this thesis, it was possible to follow the transmission behavior as a function of electrode potential of WO_3 thin films in operando. This yields detailed information about the kinetics of the ion insertion process. The coloration of amorphous WO_3 takes place in a narrow potential range, while a wide potential range is needed in order to color and bleach crystalline films. The correlation of transmission and electrode potential ($\mathrm{d}T/\mathrm{d}E$) showed that coloration is most efficient for a specific potential range. $\mathrm{d}T/\mathrm{d}E$ peaks for amorphous films are wide, meaning that efficient coloration can take place within that wide range. Very narrow $\mathrm{d}T/\mathrm{d}E$ peaks for crystalline films with similar peak values as for amorphous samples show that there is only a small potential range where efficient coloration is possible. Direct correlation of the amount of inserted charge and the corresponding transmission change can be given by $\mathrm{d}T/\mathrm{d}Q$ (if the measured current is not distorted by parasitic currents), which again reveals the differences in insertion into amorphous and crystalline WO_3 thin films.

3.3.2 Time resolved measurements of ion insertion - a case study on crystalline dip-coated tungsten trioxide

Crystalline dip-coated tungsten trioxide thin films exhibit the most pronounced characteristics in the CV and transmission data. In order to correlate electrochemical characteristics and the electrochromic coloration process a case study of this type of thin film was performed and the results are discussed in the following.
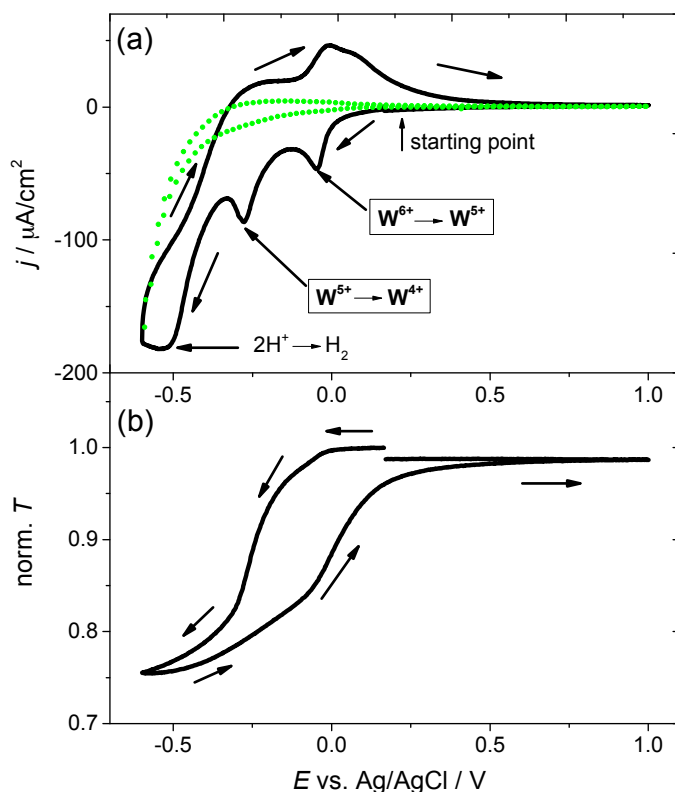
Figure 3.29: (a) CV of a dip-coated tungsten trioxide thin film calcinated at 450 °C (inside 0.1 M H_2SO_4 in H_2O). The green dots show the CV of a bare ITO covered glass substrate. (b) Normalized transmission as a function of electrode potential during cycling.

Figure 3.29 shows the CV and the corresponding transmission change as a function of electrode potential for hydrogen insertion into a crystalline dip-coated WO_3 thin film calcinated at 450 °C. Starting at the OCP, at about 0.29 V vs. Ag/AgCl, the electrode potential of the sample is reduced by a rate of 1 mV/s. At -0.05 V vs. Ag/AgCl and -0.3 V vs. Ag/AgCl reduction peaks occur (negative current maximal). The current drop at around -0.5 V vs. Ag/AgCl is due to reactions at the ITO substrate (compare green curve). As a reminder, negative currents cause insertion of protons into WO_3 from the electrolyte and of charge compensating electrons from

the external electric circuit which lead to a transmission decrease until the polarization is reversed at -0.6 V vs. Ag/AgCl. At about -0.4 V vs. Ag/AgCl positive cell currents appear denoting proton extraction or net oxidation causing bleaching of the thin film. At $E = 1\,\text{V}$ vs. Ag/AgCl the transmission almost reaches its initial value.
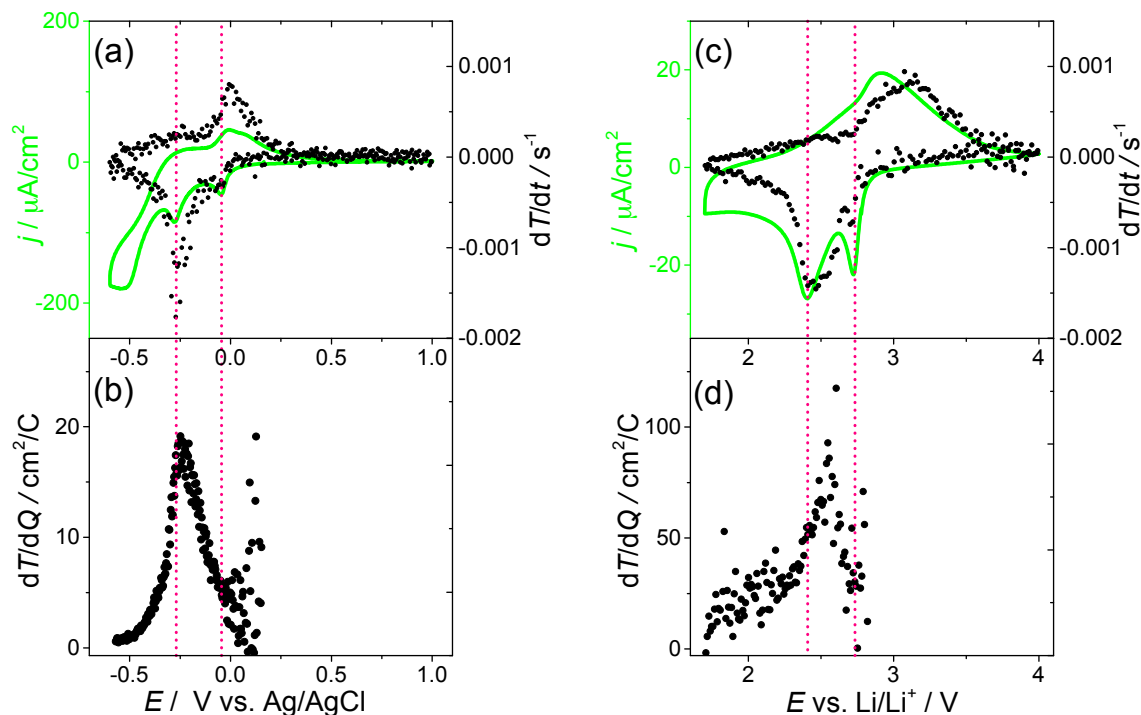
Figure 3.30: Hydrogen: (a) CV and dT/dt as a function of electrode potential, (b) dT/dQ as a function of electrode potential of a crystalline dip-coated tungsten trioxide thin film calcinated at $450\,°\text{C}$ ($0.1\,\text{M}\,H_2SO_4$ in H_2O), lithium: (c) CV and dT/dt as a function of electrode potential, (d) dT/dQ as a function of electrode potential of a crystalline dip-coated tungsten trioxide thin film calcinated at $450\,°\text{C}$ ($0.2\,\text{M}\,LiClO_4$ in PC).

Figure 3.30 (a) shows the derivative of the transmission with respect to time and the corresponding CV. The dT/dt curve peaks at the same potential positions as the current density j. However, the second reduction peak results in a higher transmission change than the first, so at first glance one might conclude that high cell currents result in high coloration. To verify this conclusion, the coloration efficiency dT/dQ is plotted as a function of time. For the potential position of the first reduction peak in the CV, dT/dQ exhibits no distinct feature on the smoothly increasing background, while it shows a pronounced maximum, with a value of dT/d$Q = 20\,\text{mC/cm}^2$, in the vicinity of the second peak in the CV.

To gain more information on the correlation of reduction peaks and coloration

characteristics, dT/dE is plotted as a function of electrode potential. Figure 3.31 depicts dT/dE for (a) the first and (b) for the 10th CV cycle with the corresponding dQ/dE curves, which for a constant scanning rate basically represent the current density. In this representation differential transmission change dT/dE shows distinct features for both reduction peaks in the CV, with a small first dT/dE peak and a distinct second peak with $dT/dE = 1.25\,\mathrm{V}^{-1}$. Figure 3.31 (b) shows that after the 10th CV cycle the first dT/dE peak vanishes and the second becomes narrower and with a dT/dE value of $1.5\,\mathrm{V}^{-1}$ even a little higher.
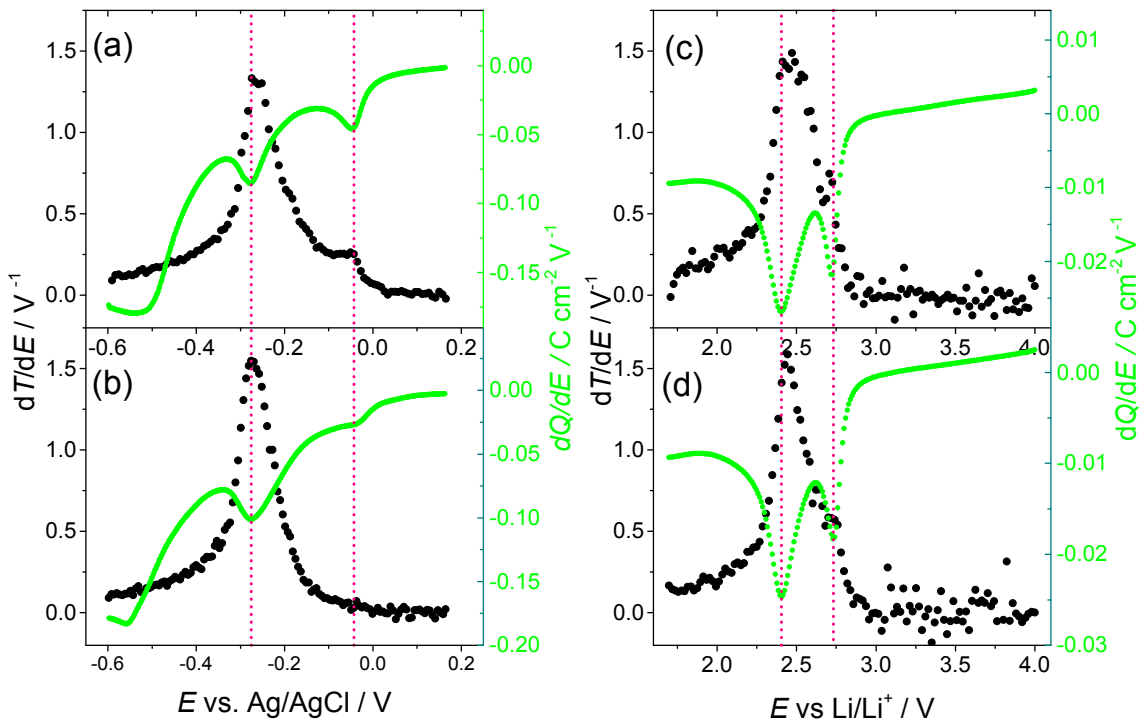
Figure 3.31: Hydrogen: (a) dQ/dE and dT/dE as a function of electrode potential for the first and (b) 10th CV cycle of a crystalline dip-coated tungsten trioxide thin film calcinated at $450\,°C$ ($0.1\,M\ H_2SO_4$ in H_2O), lithium: (c) dQ/dE and dT/dE as a function of electrode potential for the first and (d) 10th CV cycle of a dip-coated tungsten trioxide thin film calcinated at $450\,°C$ ($0.2\,M\ LiClO_4$ in PC).

In the following the lithium insertion into the same type of sample is discussed. Figure 3.30 (c) shows the dT/dt curve for lithium insertion. The corresponding CV exhibits two current peaks at $E = 2.7\,V$ vs. Li/Li^+ and $E = 2.4\,V$ vs. Li/Li^+. As for hydrogen insertion those peaks are $0.3\,V$ apart but while displaying the same transmission change, the reduction peaks are smaller by a factor of 10, showing that coloration via lithium insertion is more efficient. After the second CV peak, the current relaxes almost to zero indicating that no further electrochemical process

takes place. The coloration efficiency dT/dQ, shown in figure 3.30 (d), again is very small and hardly discernable for the first reduction peak at $E = 2.7\,\text{V}$ vs. Li/Li$^+$ due to differentiating with respect to Q leading to strong scattering of values for Q close to zero. At $E = 2.4\,\text{V}$ vs. Li/Li$^+$ a distinct dT/dQ peak occurs with a value of $100\,\text{cm}^2/\text{C}$, about a factor of 5 higher than for hydrogen insertion. Calculating the overall efficiency $\Delta T/\Delta Q$ for each reduction peak yields values of $\Delta T/\Delta Q = 0.45\,\text{mC}^{-1}$ for the first (at higher potentials) and $\Delta T/\Delta Q = 1.15\,\text{mC}^{-1}$ for the second peak (at lower potentials). Figure 3.31 (c) shows dT/dE as a function of electrode potential and the corresponding dQ/dE curve. As in the case of hydrogen insertion, two peaks at the reduction peak positions, $E = 2.7\,\text{V}$ vs. Li/Li$^+$ and $E = 2.4\,\text{V}$ vs. Li/Li$^+$, occur with the second peak accounting for the main coloration. After the 10th CV cycle, shown in figure 3.31 (d), both reduction peaks are smaller, by 20% for the first and by 10% for the second peak. The first dT/dE peak is also decreased but is still clearly visible.

The results of spectro-electrochemical measurements of hydrogen and lithium clearly show a two-step insertion mechanism, of which the first reduction at higher electrode potentials exhibits low transmission change and a low amount of charge transfer while the second reduction results in the main coloration. For hydrogen insertion the small dT/dE peak vanishes after 10 cycles and is clearly reduced for lithium insertion. Possible reasons are incomplete reoxidation of tungsten or incomplete phase re-transformation. According to Limaye et al. ions slowly migrate into WO$_6$ octahedra of the tungsten trioxide thin film and give rise to structural disorder. During the bleaching process some ions are trapped inside the octahedra. With increasing number of cycles the amount of trapped ions also increases and eventually give rise to poor recovery of the film [34].

In order to obtain a better understanding of the two-step mechanism, UV-Vis transmission experiments, XRD and XPS measurements were carried out at different charge states of the specimens. Lithium inserted thin films were employed for these ex situ analyses because no side reactions occur, in contrast to the hydrogen insertion process mentioned above. Instead of a dynamic CV insertion with a preset scan rate, galvanostatic insertion at low current densities was carried out, in order to ensure both a high degree and a homogeneous insertion of Li throughout the entire sample. Figure 3.32 (a) shows the galvanostatic discharge curve of a nanocrystalline thin film for a constant current of -300 nA.

Starting at the OCP, at about $E = 2.9\,\text{V}$, within the range of $Q = 0\,\text{mC}$ to $2\,\text{mC}$ the curve displays an s-shaped form (as discussed in section 1.5.2) with a rapid potential drop at its end. The cell potential at around $1\,\text{mC}$ might be described by a potential plateau. Then another s-shaped form of the potential develops. The potential decreases over a wider range with a shallower slope until a second plateau-like form appears at $Q = 2.5\,\text{mC}$ with a value of $E = 2.55\,\text{V}$. Figure 3.32 (b) shows another representation of the discharge curve. dQ/dE as a function of electrode
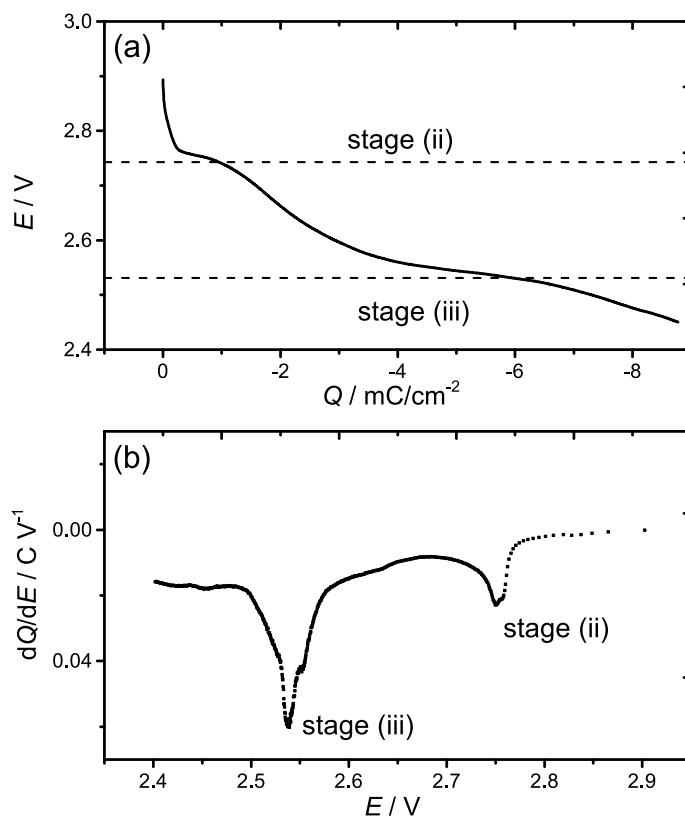
Figure 3.32: (a) Galvanostatic discharge in $0.2\,\text{M}$ LiClO_4 in PC for a dip-coated tungsten trioxide thin film calcinated at $450\,°\text{C}$. (b) $\text{d}Q/\text{d}E$ curve of the galvanostatic discharge curve.

potential exhibits two peaks, at around $E = 2.75\,\text{V}$ vs. Li/Li^+ and $E = 2.45\,\text{V}$ vs. Li/Li^+, which correspond to the peaks of the CV or the plateau-like forms of the discharge curve. It has to be kept in mind that due to polarization in the galvanostatic discharge experiment the equilibrium potential of the electrode is not measured. Thus to proof whether reduction potential plateaus (two phase regions) are present or not, titration experiments (e.g. GITT) have to be carried out.

In order to obtain a better understanding of the two-step mechanism, UV-Vis, XRD and XPS experiments were carried out for samples at three distinct states, i.e. the pristine state, the sample inserted at the first and second step. Galvanostatic discharge was stopped at the ends of the potential plateaus at high Q in order to investigate the corresponding states of charge x of Li_xWO_3:

- (i): $x = 0$, pristine WO_3

- (ii): $x = 0.08$ ($E = 2.73\,\text{V}$), tetragonal Li_xWO_3 according to Zhong et al. [19]

- (iii): $x = 0.49$ ($E = 2.45\,\text{V}$), cubic Li_xWO_3 according to Zhong et al. [19]

UV-Vis spectroscopy

In operando measurements of the optical transmission in the narrow spectral window centered at a wavelength of 633 nm showed, that the change in transmission is quite low for the first CV peak at 2.75 V (figure 3.31). To make sure that no other significant transmission changes take place in the visible spectrum at this CV peak, UV-Vis spectroscopy was carried out for three stages of insertion (i-iii), defined above. Figure 3.33 (a) shows the corresponding transmission curves for pristine and the state of charge at stage (ii). The curves look almost identical. At no wavelength significant changes in transmission could be observed. However, transmission curves for the pristine sample and the sample at stage (iii), shown in figure 3.33 (b), display large differences. Beyond 500 nm transmission of the sample in stage (iii) drops remarkably. These data support the findings that the first insertion step hardly contributes to the electrochromic characteristics of nanocrystalline WO_3 thin films. It should be mentioned that the transmission curves, shown in figure 3.33 (a) and (b), were measured in air. Hence partial degradation of the films cannot be ruled out. From optical inspection however, it is evident that the coloration of the lithium inserted films is stable for several days.
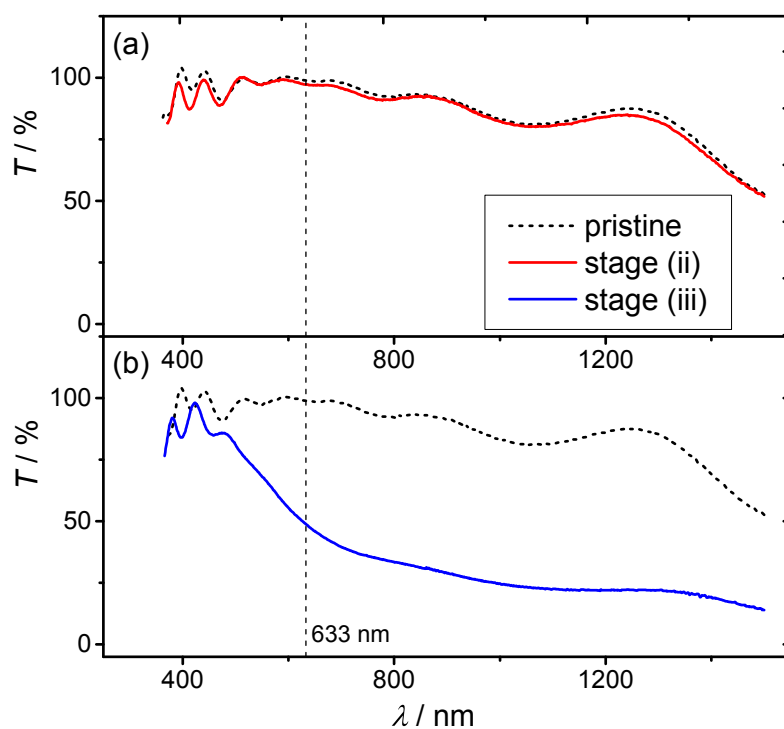
Figure 3.33: (a) UV-Vis spectrum for a pristine and a film at stage (i). (b) UV-Vis spectrum for a pristine and a film at stage (iii).

X-ray diffraction
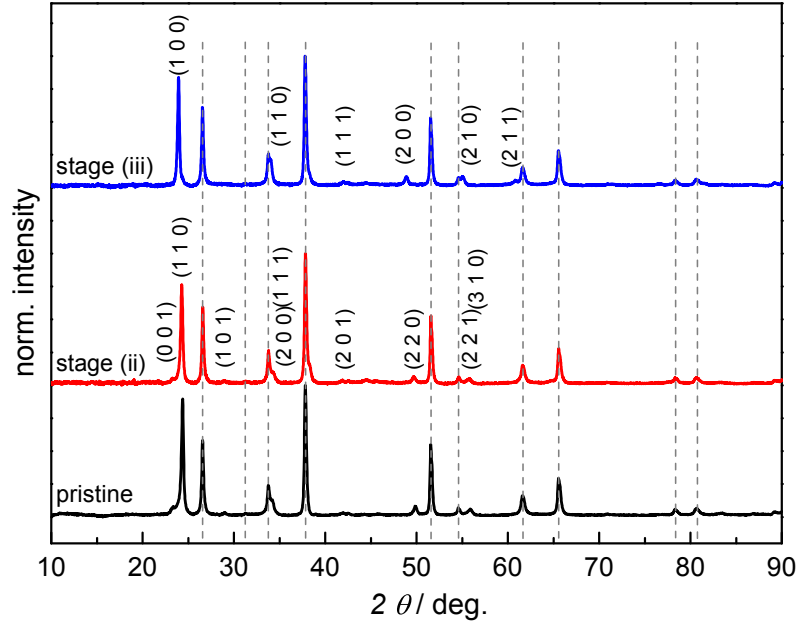
Figure 3.34: Diffractograms nanocrystalline WO_3 thin films calcinated at $450\,^\circ$C for pristine WO_3 and Li_xWO_3 at stage (ii) ($x = 0.08$) and (iii) ($x = 0.49$). Reflections that can be attributed to FTO of the substrate, are marked by vertical gray dashed lines

Furthermore, XRD measurements were carried out for samples in the three states of charge. The corresponding diffractograms of dip-coated thin films at different insertion stages are shown in figure 3.34. Reflections that can be attributed to FTO of the substrate, are marked by vertical gray dashed lines. According to Zhong et al., the two potential plateaus that appear in the discharge curve refer to the coexistence of two phases (initial monoclinic and tetragonal WO_3) and eventually tetragonal and cubic WO_3 [19]. As mentioned before, the prisitine WO_3 thin films in this work already exhibit a tetragonal structure. Figure 3.34 shows the diffractograms of the pristine film and the sample at stage (ii) ($x = 0.08$) and stage (iii) ($x = 0.49$), respectively, along with the Miller indices, hkl, of the reflections attributed to tetragonal tungsten trioxide (stage (ii)) and cubic tungsten trioxide (stage (iii)). A main reflection at $2\,\theta = 24^\circ$ can be clearly seen for all samples pointing to a preferred orientation in the (110)-direction for the pristine sample and that with $x = 0.08$ (stage (ii)) and in the (100)-direction for that with $x = 0.49$ (stage (iii)). The broad and minor features reveal the nanocrystalline nature of the samples. The pristine film as well as $Li_{0.08}WO_3$ exhibit tetragonal symmetry. The $Li_{0.49}WO_3$ thin films underwent a phase transition to the cubic structure. This means that

the first plateau-like form of the discharge curve rather corresponds to an s-shape, see chapter 1.5.2, than a real plateau or one may assume that the first plateau-like potential curve is due to the coexistence of a tetragonal WO_3 and a tetragonal Li_xWO_3 phase. While the second part may be described by a plateau, which reflects the coexistence of a tetragonal and a cubic WO_3 phase during insertion between $x = 0.08$ and $x = 0.49$.

Further analysis of the diffraction patterns gave information on the crystallite size and the unit cell volume. An increase in the average crystallite size from $11\,\mathrm{nm}$ for pristine WO_3 to $20\,\mathrm{nm}$ for $Li_{0.08}WO_3$ and $22\,\mathrm{nm}$ for $Li_{0.49}WO_3$ was observed. Furthermore, an increase in unit cell volume with increasing lithium content was derived. While the pristine film has a unit cell volume of $51 \cdot 10^6\,\mathrm{pm}^3 \pm 2 \cdot 10^6\,\mathrm{pm}^3$ per formula unit, the unit cell volume of $Li_{0.08}WO_3$ is $53 \cdot 10^6\,\mathrm{pm}^3 \pm 3 \cdot 10^6\,\mathrm{pm}^3$ per formula unit. For $Li_{0.49}WO_3$ a unit cell volume of $53 \cdot 10^6\,\mathrm{pm}^3 \pm 1 \cdot 10^6\,\mathrm{pm}^3$ is found. Unit cell volumes are in good agreement with literature. Values for tetragonal unit cell volumes of $52\text{-}57 \cdot 10^6\,\mathrm{pm}^3$ and for cubic WO_3 values of $51\text{-}57 \cdot 10^6\,\mathrm{pm}^3$ are reported, depending on the deposition method [55].
A sample that was oxidized to the deintercalated (tetragonal) state at $4\,\mathrm{V}$ vs. Li/Li^+ after 10 cycles, was analyzed in order to check on the reversibility of this behavior. This sample exhibited an average crystallite size of $26\,\mathrm{nm}$, which is even larger than the value the cubic sample exhibited during the first cycle.

X-ray photoelectron spectroscopy

During the ion insertion process a charge compensating electron is inserted into the thin film, which is equivalent to electrochemical reduction. To find out whether the electrochemical reduction of WO_3 constitutes a two-step process, an XPS analysis of samples at the three insertion states was carried out. The samples were transferred from the glove box into the XPS chamber without contact to atmosphere. Figure 3.35 shows the $W\,4f$ core spectra obtained from samples in the three different charge states. Pristine tungsten trioxide, as expected, shows a typical single $W\,4f$ doublet peak with peak positions of $W\,4f_{7/2}$ at $35.4\,\mathrm{eV}$ and $W\,4f_{5/2}$ at $37.6\,\mathrm{eV}$. This can clearly be attributed to the W^{6+} oxidation state (see also section 3.2.3). Insertion to $Li_{0.08}WO_3$ (stage (ii)) yields a new feature in the XP spectrum, another doublet peak with positions of $W\,4f_{7/2}$ at $34.5\,\mathrm{eV}$ and a fractional area of 20% of the total $W\,4f_{7/2}$ signal. This doublet corresponds to the W^{5+} position [63, 64, 65, 66, 67]. Further lithium insertion, stage (iii) ($Li_{0.49}WO_3$), results in an even more pronounced feature, with a doublet peak with peak position of $W\,4f_{7/2}$ at $33.3\,\mathrm{eV}$. This can be attributed to the W^{4+} oxidation state with fractional peak areas of W^{6+}:50%, W^{5+}:20.4% and W^{4+}:29.6% [64, 65, 66].

Within its information depth, theses XPS measurements show that the observed two-step insertion comes along with a two-step reduction of tungsten, in the first step from W^{6+} to W^{5+} and in the the second step from W^{5+} to W^{4+}. Thus the

maximum transmission change in nanocrystalline WO_3 thin films is observed when a significant amount of W^{4+} can be detected, and W^{5+} seems to induce only a small transmission change.
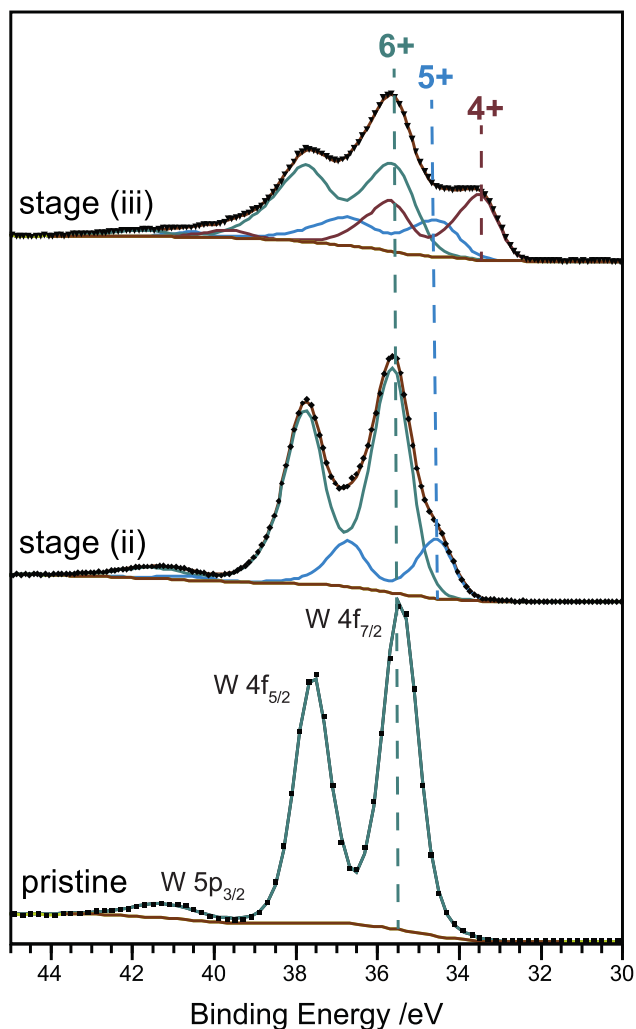
Figure 3.35: XP spectra for crystalline dip-coated tungsten trioxide calcinated at 450 °C for a prisitine sample (stage (i)) and lithium inserted film up to $x = 0.08$ (stage (ii)) and $x = 0.49$ (stage (iii)) of the galvanostatic discharge curve.

The coloration in WO_3 associated to the existence of W^{4+} has been proposed in literature, however there are significant differences to the findings presented in this thesis. In the work of Deb et al. [69] the existence of W^{4+} was correlated to the presence of an oxygen vacancy which means that an equal concentration of oxygen vacancies and W^{4+} is present. For the findings presented in this thesis, i.e. 30% after intercalation, this would require 10% of oxygen sites being vacant ($WO_{2.7}$). Such a high concentration of oxygen vacancies in crystalline WO_3 is very improbable. In addition XPS analysis clearly showed that the pristine films are almost stoichiometric, as only W^{6+} was detected. From this one can conclude that the formation of W^{4+} does not require oxygen vacancies in crystalline WO_3 but is a result of electrochemical reduction via lithium insertion. Formation of W^{4+} ($W_W^{''}$) via formation of oxygen vacancies ($V_O^{\bullet\bullet}$):

$$WO_3 \rightarrow W_W^{''} + V_O^{\bullet\bullet} + 2O_O^x + \frac{1}{2}O_{(2,(g))}. \tag{3.1}$$
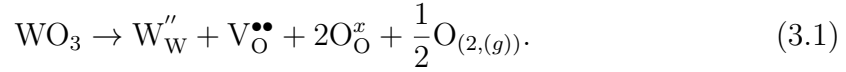
Formation of W^{4+} via lithium insertion (formation of lithium interstitials, $Li_i^{\bullet}$):

$$WO_3 + 2Li \rightarrow W_W^{''} + 2Li_i^{\bullet} + 3O_O^x. \tag{3.2}$$
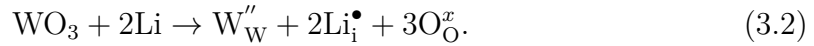
In the works of Lee et al. [70, 73, 74] it was proposed that (transparent) pristine amorphous tungsten trioxide thin films mainly contain W^{6+} and W^{4+} and that due to ion insertion W^{5+} is formed and by performing the following transition [70, 74] coloration is induced:

$$h\nu + W^{4+}(A) + W^{5+}(B) \rightarrow W^{5+}(A) + W^{4+}(B) \tag{3.3}$$
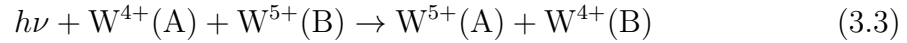
and the transition from W^{5+} to W^{6+}:

$$h\nu + W^{5+}(A) + W^{6+}(B) \rightarrow W^{6+}(A) + W^{5+}(B). \tag{3.4}$$
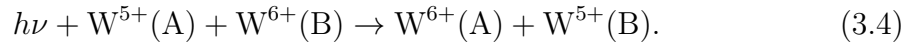
In contrast to the findings of Lee et al., results presented in this work show that pristine nanocrystalline WO_3 is almost stoichiometric, as only W^{6+} is detected, and a high coloration is only possible due to the presence of W^{4+}, most probably mainly performing the following bipolaronic transition:

$$h\nu + W^{4+}(A) + W^{6+}(B) \rightarrow W^{6+}(A) + W^{4+}(B) \tag{3.5}$$
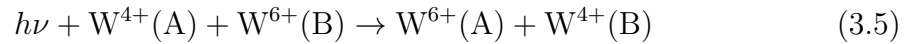
which, according to Schirmer et al. [32], is more likely than single polaronic transitions (eq. 3.3 and 3.4).

3.3.3 Self-bleaching

In terms of electrochromism, the open circuit memory denotes the period of time in which the insertion/coloration state is stable. The colored state of an electrochromic thin film may be altered by *self-bleaching*, which is the phenomenon of current-free discoloration.

Self-bleaching behavior for hydrogen inserted WO_3 films was analyzed for amorphous and crystalline electron-beam evaporated and sputtered thin films. Time-dependent self-bleaching was monitored after coloring the sample by potentiostatic coulometry (constant potential at the working electrode).
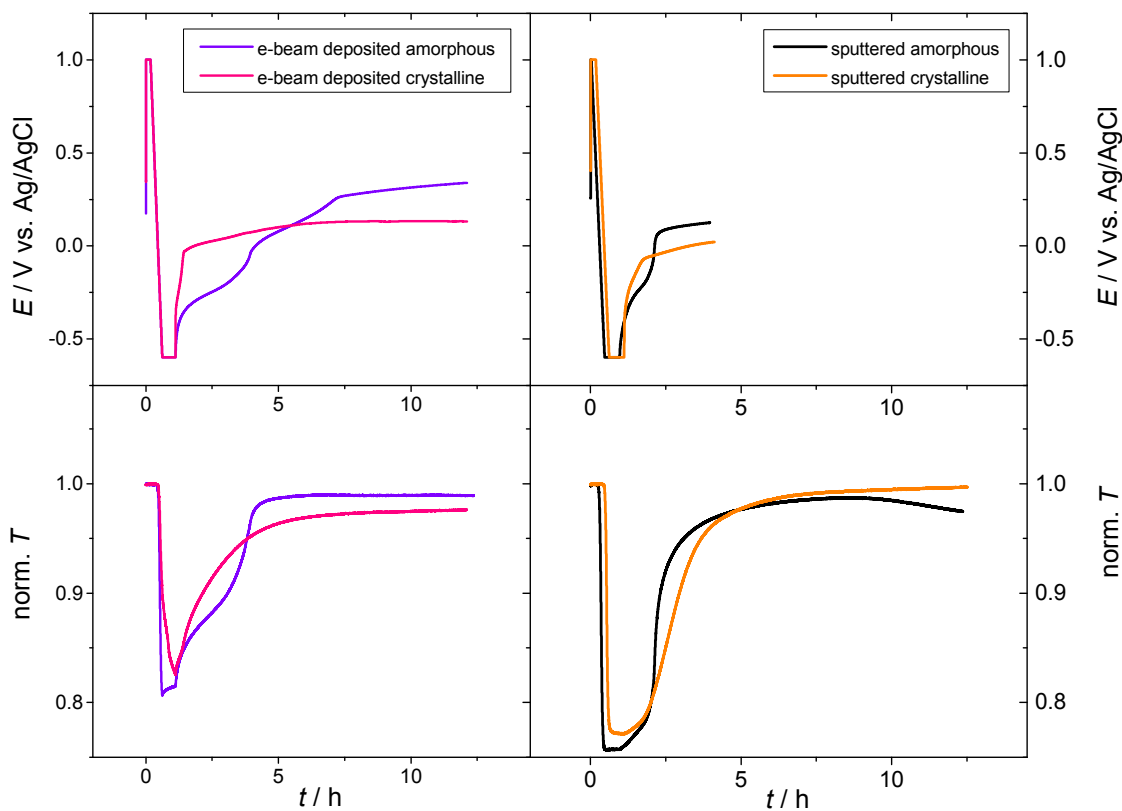
Figure 3.36: Transmission spectra and potential curves for crystalline and amorphous electron-beam and sputtered WO_3 thin films during coloration and self-bleaching.

After recording the open circuit potential (around 0.3 V vs. Ag/AgCl), the samples were bleached at 1 V vs. Ag/AgCl for 1 to 10 min, then with a ramp of 1 mV/s a constant potential of -0.6 V vs. Ag/AgCl was approached and held at the working electrode for 30 min. After coloring, the external electric potential was turned off and OCP and transmission were recorded. Figure 3.36 shows transmission and potential data for this experiment.

Transmission of the crystalline electron-beam evaporated thin film does not saturate during the ion insertion process. When the external electric potential is turned off, it relaxes rapidly. The OCP however instantly relaxes towards $E = -0.3\,\mathrm{V}$ vs. Ag/AgCl and after that then linearly, with a steep slope, by another $0.3\,\mathrm{V}$ within 30 min. At that point, $E = 0\,\mathrm{V}$ vs. Ag/AgCl, there is a sharp bend and the OCP relaxes within 6 h with a shallow slope and saturates at $E = 0.1\,\mathrm{V}$ vs. Ag/AgCl, 200 mV from the original OCP.

As expected from the quick coloration kinetics of amorphous WO_3 (see section 3.3.1), the amorphous thin film almost instantly reached its minimum transmission after the application of the final electrode potential of -0.6 V vs. Ag/AgCl. During the period of the application of a constant potential, the transmission increases rapidly within a small range until the external potential is turned off. A possible reason is the degradation of the WO_3 film itself. Then during OCP, the transmission relaxes exhibiting two plateaus with the second plateau at the sample's initial transmission value (3 h after the external potential is turned off). The OCP also relaxes exhibiting two potential plateaus, the first one extending over 3 h toward $E = -0.1\,\mathrm{V}$ vs. Ag/AgCl. Interestingly, the transmission has gained its initial value at that state, however, after that a second potential plateau develops without having any impact on transmission. The second plateau extends for another 3 h, after that time the OCP relaxes linearly with a small slope without reaching saturation after 10 h of self-bleaching.

Transmission minima of amorphous and crystalline sputtered thin films are reached as soon as the final potential is applied. During application of a constant potential the transmission remains constant, indicating that the samples are more stable than the amorphous electron-beam evaporated films. Both, amorphous and crystalline sputtered thin films nearly reach their initial transmission values by self-bleaching within 10 h of OCP.

The transmission of the sputtered amorphous thin film first linearly relaxes for the first hour. For the next 5 hours the transmission relaxes first vertically and then rapidly. After that time both samples start saturating close to the initial OCP value. The OCP of the amorphous film exhibits two plateaus, each extending over one hour, until it trails off with a very small slope at $E = 0.1\,\mathrm{V}$ vs. Ag/AgCl. The OCP of the sputtered crystalline film first vertically jumps up to $E = -0.25\,\mathrm{V}$ vs. Ag/AgCl and then linearly relaxes towards $E = 0\,\mathrm{V}$ vs. Ag/AgCl within 1 hour when it starts relaxing with a smaller slope.

Obviously no stable coloration of WO_3 could be obtained in the aqueous electrolyte used, unless a negative potential is applied continuously.

A similar experiment using amorphous Li_xWO_3 shows that self-bleaching of tungsten trioxide is much slower for Li as inserted metal than for hydrogen. After stopping the insertion at 2 V vs. Li/Li^+, transmission and OCP slowly and linearly relax

toward their initial value (see figure 3.37). However, after 10 h of self-bleaching, transmission only relaxed from 78% to 85% and OCP, at a value of $E = 2.4\,\mathrm{V}$ vs. $\mathrm{Li/Li^+}$, did not reach its initial value.
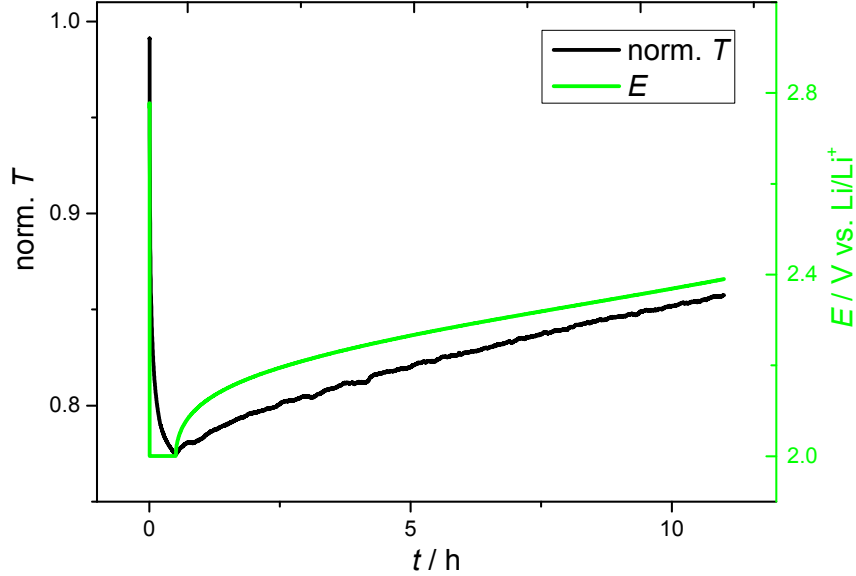
Figure 3.37: Transmission and potential curve for an amorphous electron-beam evaporated $\mathrm{WO_3}$ thin film during coloration and self-bleaching.

$\mathrm{Li}_x\mathrm{WO_3}$ samples stored in argon atmosphere were still blue after weeks of storage. Hydrogen inserted samples on the other hand bleached over night in air atmosphere. According to a model presented by Zhang et al., self-bleaching only takes place in environments containing oxygen [31]. Oxygen is assumed to diffuse into the thin film and oxidizes $\mathrm{W^{5+}}$ according to the chemical reaction of hydrogen inserted tungsten trioxide:

$$\mathrm{WO}_{3-y-x/2} \cdot n\mathrm{H_2O} + \frac{x}{4}\mathrm{O_2} \longrightarrow \mathrm{WO}_{3-y} \cdot n\mathrm{H_2O} \tag{3.6}$$

As presented earlier, electrochromic coloration in nanocrystalline $\mathrm{WO_3}$ is mainly due to the formation of $\mathrm{W^{4+}}$, but equation 3.6 is independent from the oxidation state of tungsten and may also be applied to $\mathrm{W^{4+}}$. Initial tungsten trioxide, WO_{3-y}, and water are created during the self-bleaching process. In the case of $\mathrm{Li}_x\mathrm{WO_3}$, oxygen $\left(\frac{x}{4}\mathrm{O_2}\right)$ oxidizes $\mathrm{WO}_{3-y-x/2}$ to its initial form (WO_{3-y}) according to:

$$\mathrm{WO}_{3-y-x/2} \cdot [n\mathrm{H_2O} \cdot \frac{x}{2}\mathrm{Li_2O}] + \frac{x}{4}\mathrm{O_2} \longrightarrow \mathrm{WO}_{3-y} \cdot [n\mathrm{H_2O} \cdot \frac{x}{2}\mathrm{Li_2O}] \tag{3.7}$$
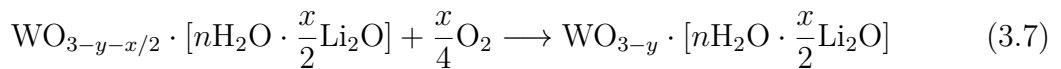
Lithium oxide remains inside the thin film and cannot easily be removed, which eventually leads to a degradation of the film. Kamal et al. analyzed self-bleaching for amorphous and crystalline sputtered $\mathrm{WO_3}$ thin films for different environmental

conditions [29]. Figure 3.38 shows self-bleaching of an amorphous WO_3 thin film as a function of time. The specimens were surrounded by different oxidatives, 0.1 M H_2SO_4, pure water and air, after saturated coloration of the samples. The self-bleaching process is quick at the beginning and then saturates linearly. A saturated state was attained within the first 3 minutes of the self-bleaching process. Self-bleaching is quickest inside the electrolyte solution and slowest in air. Curves for crystalline thin films were not presented, but are reported to have larger open circuit memory due to large polarons, which are assumed to be more tightly bound than small polarons of amorphous thin films. Loosely bound polarons are thus assumed to be more easily available for reactions with oxygen than tightly bound polarons.
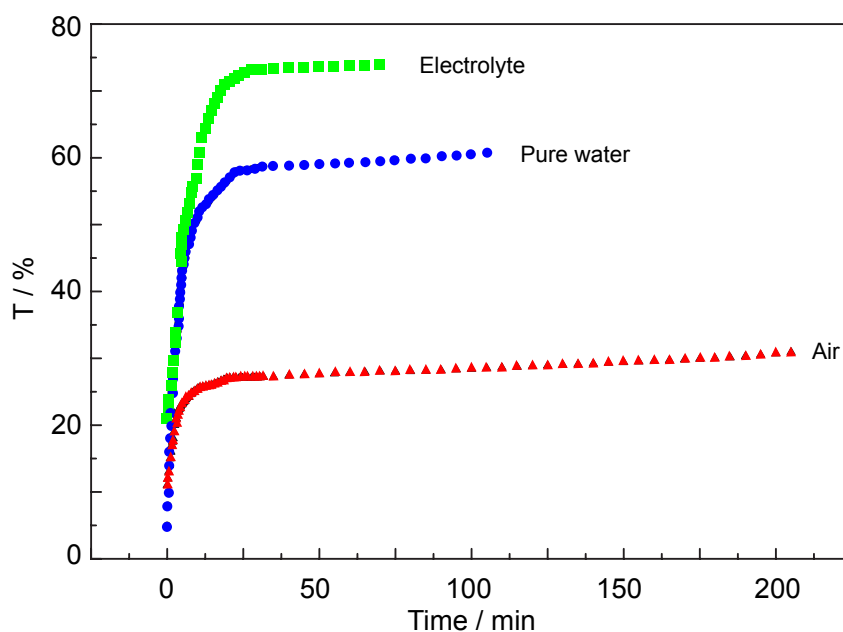
Figure 3.38: Self-bleaching of colored tungsten trioxide inside different surrounding media (adapted from [29]).

Amorphous electron-beam evaporated and sputtered samples, presented in this work, also exhibit quicker self-bleaching than their crystalline counterparts. Amorphous thin films reach 50% of their initial transmission value 1 h earlier than crystalline thin films. The presented electron-beam deposited and sputtered thin films reach their initial transmission value after about 10 h of self-bleaching. This means that they exhibit open circuit memory of about a factor 100 larger than those presented by Kamal et al. However, a comparison remains difficult as the samples studied by Kamal et al. had a much higher coloration state with transmission values of about 10 %. The higher coloration state might be due to a higher coloration efficiency or due to a larger film thickness (270 nm) about a factor of 2 thicker than those presented in this thesis.

As alternative to the mechanism described above (equation 3.6) reactions at the WO_3/electrolyte interface can take place also leading to self-bleaching of the thin film:

$$H_xWO_3 + \frac{x}{4}O_2 \longrightarrow \frac{x}{2}H_2O + WO_3 \tag{3.8}$$
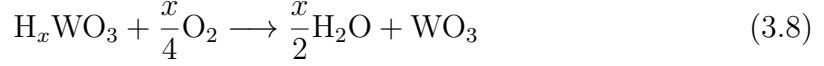
oxygen is reduced and forms H_2O. In a similar way a self-bleaching reaction for Li_xWO_3 is possible:

$$Li_xWO_3 + \frac{x}{2}O_2 \longrightarrow WO_3 + Li_2O_2 \tag{3.9}$$
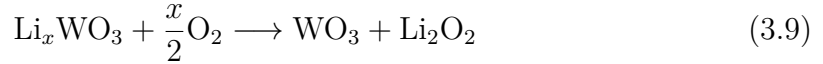
The self-bleaching experiment for Li_xWO_3 was carried out outside the glove box and thus oxygen might have diffused into the cell due to leakages. Oxygen is reduced and forms lithium peroxide:

$$2Li + O_2 \longrightarrow Li_2O_2 \tag{3.10}$$

This reaction can take place for electrode potentials $E < 2.96\,\text{V}$ vs. Li/Li^+ [75, 76], which is the case for all lithium insertion experiments presented in this work. Another possibility is the formation of Li_2O.

The processes described by equations 3.8 and 3.9 may be more likely as those presented by Zhang et al. for the following reason. They can be considered as chemical de-insertion (extraction) process. H^+ or Li^+ diffuse to the WO_3 surface and react with O_2 to form Li_2O_2, Li_2O or H_2O. Zhang et al. on the other hand propose that oxygen fills vacancies in a WO_{3-x} crystal, leading to bleaching of the material. This, however, in the end requires insertion and transport of the oxygen ion (O^{2-}) within the solid state, which at room temperature is a very slow process and hence is much more unlikely than transport of Li^+ or H^+ towards the surface.

3.4 Spatially and temporally resolved studies of hydrogen transport in WO_3

Time resolved in situ transmission spectroscopy during electrochemical ion insertion experiments, that were possible with the introduced setup, were presented in the former section. Now another possible application of the setup, temporally and spatially resolved transmission experiments, are presented and used to study diffusion of hydrogen inside WO_3.

In order to conduct spatially resolved experiments of ion diffusion, either the WO_3 thin film itself or the transparent conductive oxide (TCO) substrate needs to be patterned to force a motion of charge carriers parallel to the substrate surface and thus over distances of several µm and longer. Both approaches will be presented in the following.

3.4.1 Substrate patterning for forcing a concentration/color gradient

One way to prepare samples for spatially resolved studies of the coloration process in WO₃ is based on patterning the TCO electrode on the glass substrate by photolithography. The resulting $50\,\mu m$ photo resist line structure was used as etching mask. After etching in aqua regia the uncovered parts of the substrate were free from the ITO layer. Lift-off in acetone removed the resist lines and a glass-ITO line structure remained. Afterwards a WO₃ thin film was deposited on top of that pattern by dip-coating, as described in section 2.2. The sample was mounted inside the electrochemical hydrogen cell as usual. The idea was that only WO₃ areas on top of ITO lines (current collectors) would be colored in the first place when an external electric potential is applied. The goal was then to image the diffusion from the colored lines into the neighboring transparent WO₃ areas on top of the insulating glass lines. Figure 3.39 shows the image of a glass-ITO line pattern covered with
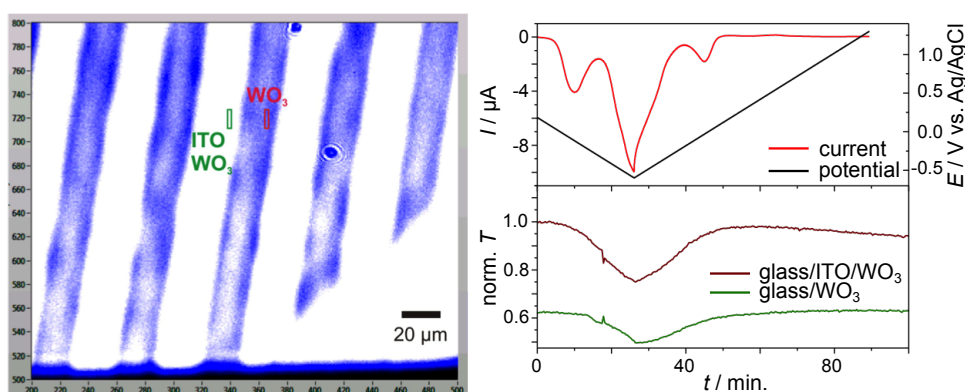
Figure 3.39: Left: Transmission image of WO₃ on top of a glass-ITO pattern. Right: Transmission curve during hydrogen insertion into WO₃ for areas of ITO and glass underneath the thin film.

a H_xWO₃ (hydrogen inserted WO₃) thin film (displayed miscolored). On the right hand side the applied electric potential and the corresponding current is displayed as a function of time. The bottom graph shows the resulting transmission curve for a WO₃/ITO/glass line and a WO₃/glass line area. When a negative current flows, i.e. ions are inserted into the thin film, the transmission drops in both areas. The transmission of areas that are free from the ITO layer start coloring delayed in time and not as deeply as the ITO/WO₃ areas. The reason for coloration of all areas, is the electric conductivity of WO₃, which increases with the amount of inserted ions [68, 77]. The WO₃ layer then functions as electrode itself and electrons can move freely inside the thin film. Figure 3.40 (a) shows an illustration of the insertion process: ions (M^+) from the electrolyte enter the thin film, which is deposited on top

of the ITO layer. When some of the ions have diffused into the ITO-free WO_3 areas, the local electronic conductivity there is increased and electrons can move more freely inside that region. As a consequence, the formerly insulating WO_3/glass areas allow ion insertion directly from the electrolyte. For this reason patterning of the TCO substrate only introduces lateral motion of electrons, but cannot be employed to introduce a lateral motion of ions.

(a) Glass-ITO pattern
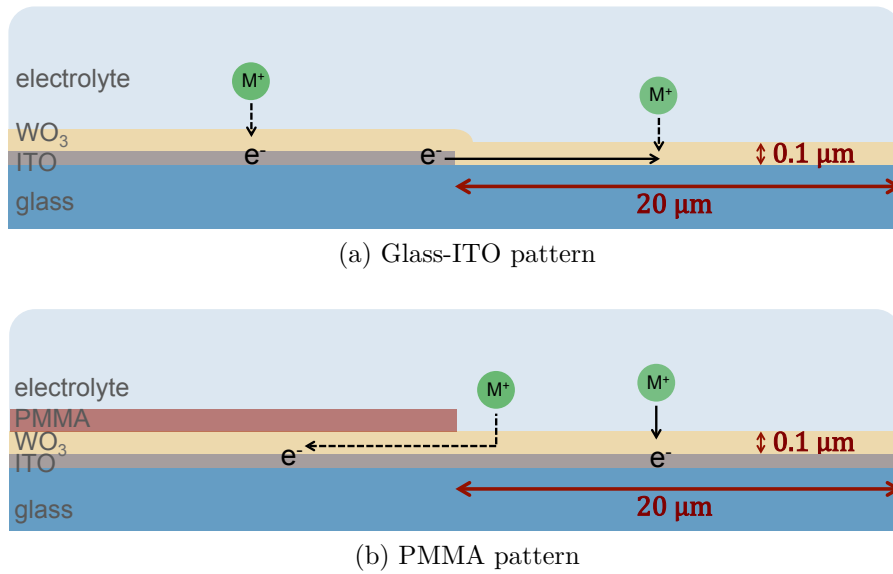
(b) PMMA pattern

Figure 3.40: Illustration of ion transport for (a) a glass-ITO pattern covered with a WO_3 thin film and (b) a with PMMA partially covered WO_3 thin film.

A more suitable approach is the deposition of a transparent pattern of both, an electronic and an ionic insulator on top of the WO_3 thin film, which is depicted schematically in figure 3.40 (b). Ions from the electrolyte solution can only enter areas of the thin film, which are not covered by the transparent protection layer. Ions enter the thin film in the areas of uncovered WO_3. Due to diffusion of the ions inside the thin film, areas which are covered will successively be colored as well. In this work different materials such as polymers (PMMA) or oxides (MgO, Al_2O_3) were tested. Major challenges are a full and crack free coverage of WO_3, as well as a sufficient inertness of the cover material against the acidic electrolyte. Results with PMMA (Poly(methyl methacrylate)) will be presented in the following.

3.4.2 Thin film patterning for forcing a concentration/color gradient

A pattern made of a transparent substance on top of the electrochromic thin film may help to obtain spatial information of the electrochromic coloration process. PMMA, a transparent electron-beam resist, can be employed to pattern the sample of interest. A WO$_3$ thin film completely covered by PMMA except for a $50\,\mu\mathrm{m}\times50\,\mu\mathrm{m}$ rectangle in its center was tested in the hydrogen cell. A constant external potential is applied to the sample by ramping the external electric voltage to a value of -0.3 V vs. Ag/AgCl with a rate of $1\,\mathrm{mV/s}$ and then holding this value. Only the area with direct contact to the electrolyte solution, i.e. the rectangle shaped area, is initially colored.
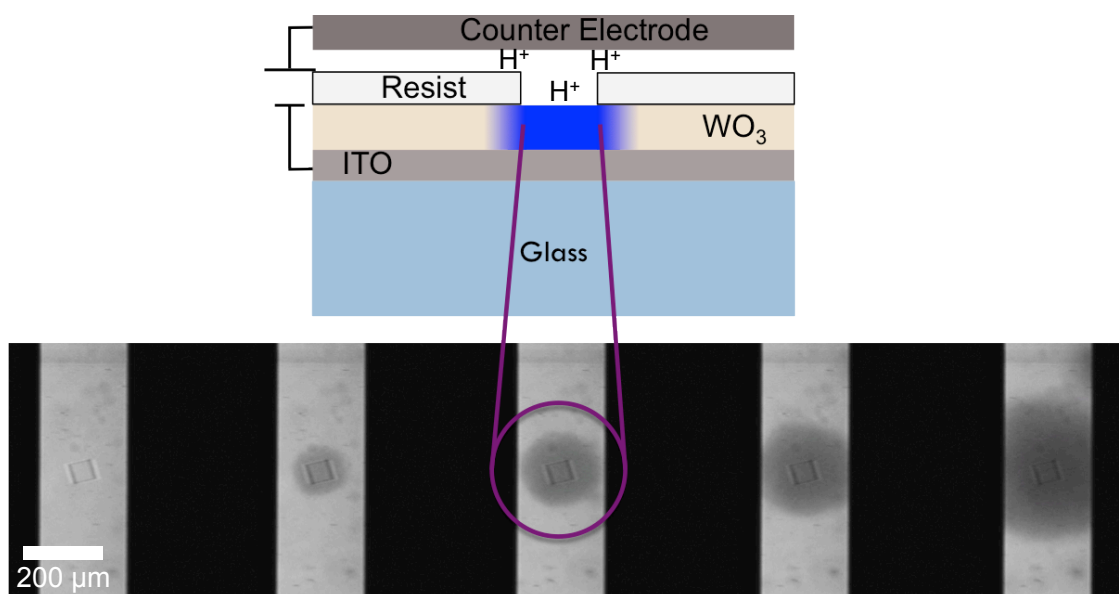
Figure 3.41: Schematic illustration of the patterned WO$_3$ thin film inside an electrochemical cell and CCD images of a PMMA covered WO$_3$ thin film in the hydrogen cell during a diffusion experiments for different points in time.

Figure 3.41 shows a schematic drawing of the patterned film inside the cell and the CCD images for different points in time. The first image shows the sample before the insertion process. A rectangle in the center of the image, which exhibits little contrast to the rest of the sample can hardly be distinguished since WO$_3$ and PMMA are both transparent. After some time a circular dark spot, due to the hydrogen insertion, surrounding the rectangle, becomes visible. Successive coloration outside the rectangle is caused by ion diffusion from the rectangle through the WO$_3$ film.

Lateral ion diffusion in electron-beam evaporated WO$_3$

In order to create quasi one dimensional conditions for the diffusion experiment, a line pattern was transferred onto the thin film instead of a rectangle for the experiment described in the following. Each sample was covered by PMMA except for a 50 μm line and inserted into the hydrogen cell as described above. An illustration of the direction of diffusion starting at the edge of the line opening is depicted in figure 3.42. Figure 3.43 (a) and (b) show the series of transmission curves locally obtained at various distances from the edge of the line opening for amorphous and crystalline WO$_3$, respectively. Colored curves are smoothed data, raw data is depicted by black lines. As a reference the transmission of the areas inside the line opening corresponding to $x = 0$ are shown as black curves.
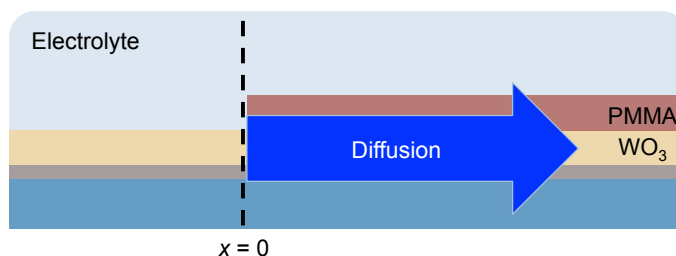
Figure 3.42: Illustration of the direction of diffusion starting at the edge of the line opening.

The transmission of an area of the amorphous sample close to the line (orange curve) decreases exponentially. With increasing distance from the line the shape of the curve becomes shallower. The transmission of the outermost area of the sample, at 75 μm from the line (depicted by the yellow curve), starts decreasing 40 min after the external potential was applied to the sample. 200 min later the transmission is decreased by merely 10% while the transmission of an area close to the line is already decreased by 35%.

The shape of the transmission curves of the crystalline and amorphous sample for areas close to the line are very similar. However, for areas at a larger distance from the line the transmission curves of the crystalline sample are clearly shifted on the time axis. For example, the transmission of an area 55 μm away from the line (purple curve) remains 100% for the first hour and then rapidly decreases when the ions have diffused into that area.

The reference transmission curve of the amorphous sample drops rapidly to an almost constant level. Provided that Lambert Beer's law is valid, this corresponds to a constant surface concentration of a diffusion problem. The slight increase of transmission of the amorphous sample starting at 90 min is probably due to the degradation of the thin film due to the oxidative environment discussed earlier. The assumption of a constant concentration source, however, may still be applied.
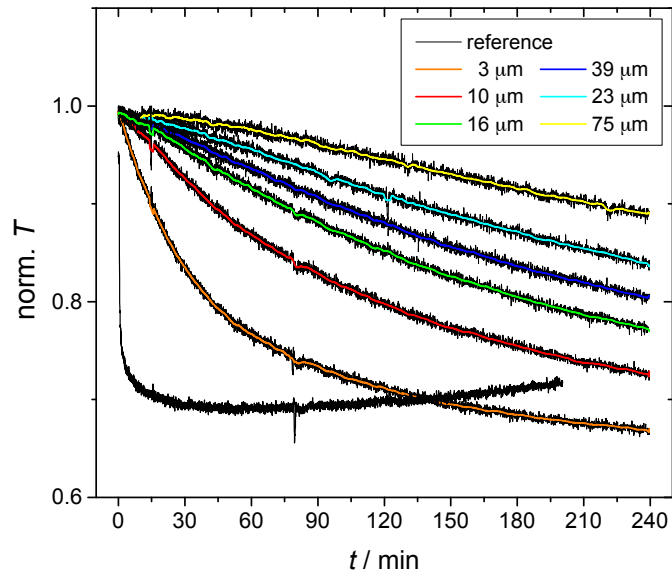
(a)
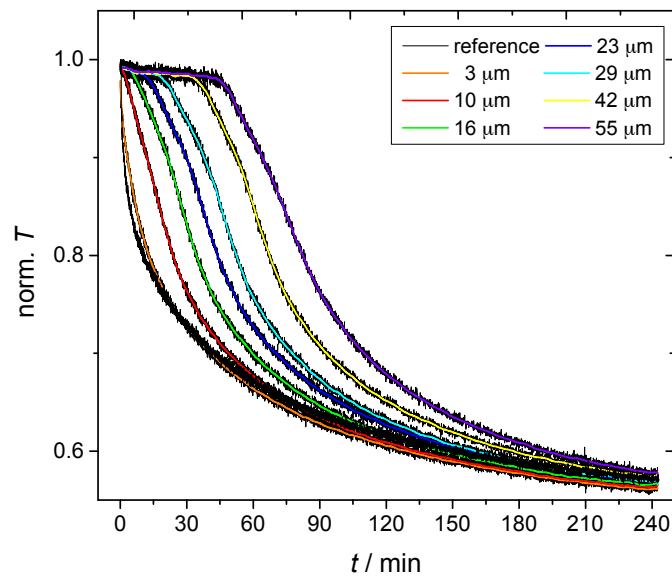
(b)

Figure 3.43: Transmission as a function of time for different distances from the patterned line for (a) amorphous and (b) crystalline electron-beam evaporated WO$_3$ thin films.

In the case of crystalline WO$_3$, the situation is different. The transmission at $x = 0$ only decreases slowly in time and does not attain a constant value within the considered time span of 4 h. Thus the assumption of a constant surface concentration, c_s, of hydrogen as a boundary condition for this diffusion problem is not valid.

A solution of the diffusion equation for amorphous WO_3 is given by the complementary error function below [38].

$$c(x) = c_s \mathrm{erfc}\left(\frac{x}{2\sqrt{Dt}}\right).$$ (3.11)

Equation 3.11 describes diffusion with a constant surface concentration c_s, which is assumed for the presented experiment. The normalized function for the concentration as a function of spatial coordinate x and time t for different diffusion lengths $\sqrt{Dt}$, where D is the diffusion coefficient is given by:

$$\frac{c(x)}{c_s} = \mathrm{erfc}\left(\frac{x}{2\sqrt{Dt}}\right)$$ (3.12)

Coloration in WO_3 is dependent on the number of reduced tungsten atoms. Lambert-Beer's law is employed to describe the attenuation of light when entering the WO_3 film. Assuming the absorption coefficient is proportional to the concentration $c(x)$, the absorbance A of a medium is given by:

$$A(x) = -\ln\frac{I(x,d)}{I_0} = -k \cdot c(x) \cdot d$$ (3.13)

where k is a proportionality constant, d is the thickness of the sample and $c(x)$ the concentration of the absorbing species at lateral position x (see figure 3.44).
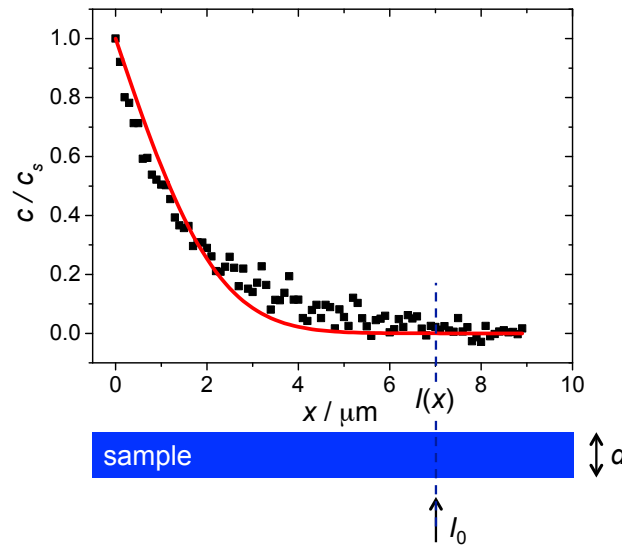
Figure 3.44: Illustration of the light attenuation after passing through a sample with thickness d and normalized concentration $c(x)/c_s$ at lateral location x on the sample surface.

Equation 3.14 is Lambert-Beer's law considering the surface concentration c_s.

$$A(x) = -\ln\left(\frac{I_s}{I_0}\right) = -k \cdot c_s \cdot d \tag{3.14}$$

Using this equation, a relationship between the transmission determined by the experiment and the concentration of species responsible for coloration, which is needed for a theoretical description (eq. 3.12), can be made. Combining equation 3.13 and 3.14, the following equation is easily derived:

$$\frac{c(x)}{c_s} = \frac{-\ln\left((I(x,d)/(I_0)\right)}{-\ln\left((I_s)/(I_0)\right)} = \frac{\ln(I(x,d)) - \ln(I_0)}{\ln(I_s) - \ln(I_0)}. \tag{3.15}$$

The normalized concentration of species responsible for coloration in WO$_3$ derived from the transmission curves based on the assumption that eq. 3.13 and 3.14 are valid, and the corresponding fits, using eq. 3.12, are presented for amorphous WO$_3$ in the next section.

Analysis of lateral hydrogen diffusion inside an electron-beam evaporated WO$_3$ thin film
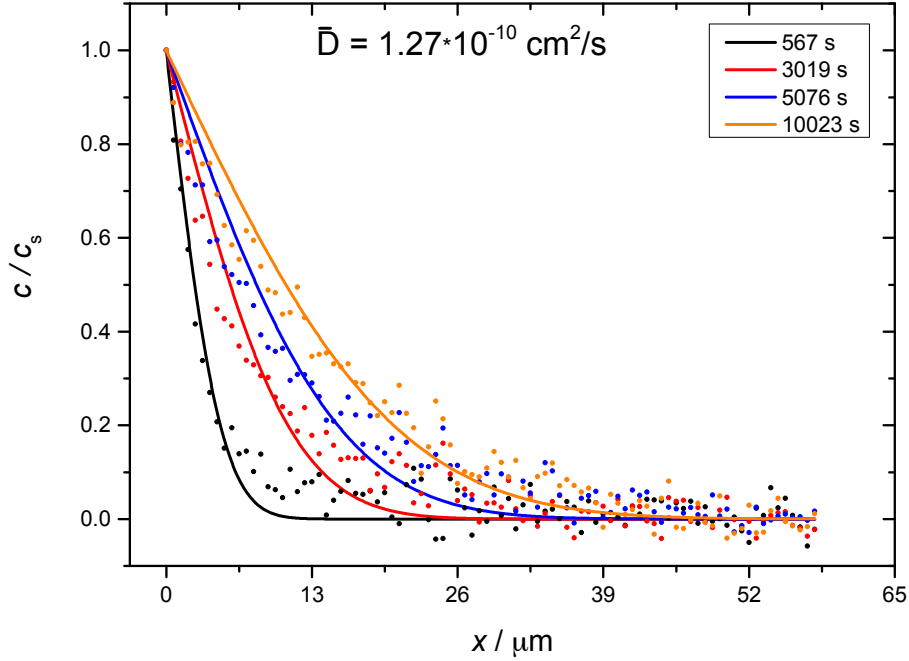
Figure 3.45: Experimental $c(x)/(c_s)$ curves of amorphous electron-beam evaporated WO$_3$ for four different values of diffusion time (dots) and the corresponding fit (solid lines).

In the following $c(x)/c_s$ is calculated using equation 3.15 with I_s and I_0 determined individually for each image taken. Figure 3.45 shows $c(x)/c_s$ of amorphous WO$_3$ as a function of spatial coordinate x at four different moments in time together with the corresponding fits by eq. 3.12. With increasing time the species responsible for coloration propagate through the WO$_3$ film. All curves have a normalized concentration value of 1 for $x = 0$ and drop down to zero at sufficiently large distance from the line. The curve for $t = 564\,\mathrm{s}$ (black curve), a time shortly after the external potential was applied to the sample, is very steep, i.e. the curve drops down to a value of zero within the first $10\,\mu\mathrm{m}$ away from the line. With increasing time the curves become more shallow. At $t = 10023\,\mathrm{s}$ (orange curve) a concentration value of zero, i.e. the detection limit, is observed at $x = 45\,\mu\mathrm{m}$. Diffusion coefficients for hydrogen inside amorphous WO$_3$ obtained from the fits are:

- $D(567\,\mathrm{s}) = 1.3 \cdot 10^{-10}\,\mathrm{cm^2/s}$

- $D(3019\,\mathrm{s}) = 1.2 \cdot 10^{-10}\,\mathrm{cm^2/s}$

- $D(5076\,\mathrm{s}) = 1.4 \cdot 10^{-10}\,\mathrm{cm^2/s}$

- $D(10023\,\mathrm{s}) = 1.3 \cdot 10^{-10}\,\mathrm{cm^2/s}$,

which is in good agreement with values found in literature ($10^{-10}\,\mathrm{cm^2/s}$ to $10^{-8}\,\mathrm{cm^2/s}$ [44, 45, 46]). The mean value of all four diffusion coefficients is $D = 1.3 \cdot 10^{-10}\,\mathrm{cm^2/s}$ $\pm\ 0.1 \cdot 10^{-10}\,\mathrm{cm^2/s}$. Experimental curves and theoretical curves for a fixed value of $D = 1.3 \cdot 10^{-10}\,\mathrm{cm^2/s}$ are shown in figure 3.46. Experimental and theoretical curves are in good agreement.
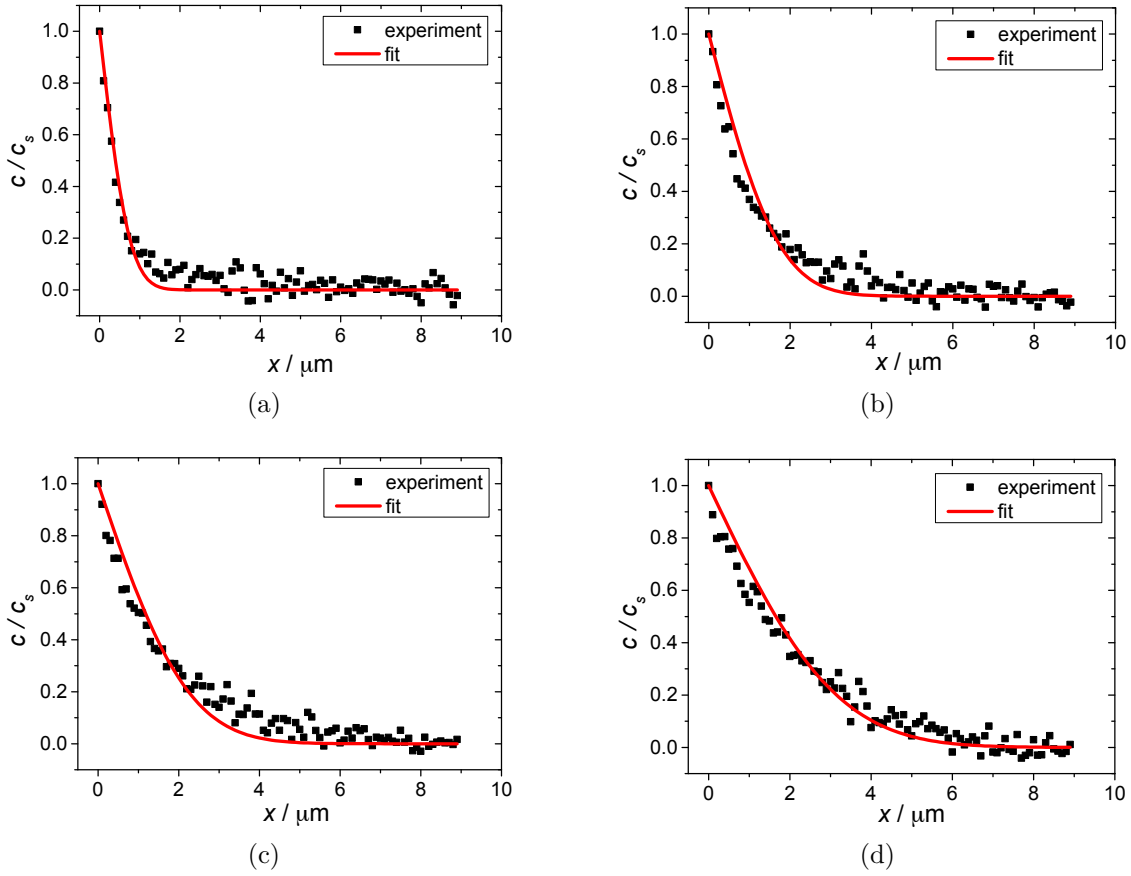
Figure 3.46: Experimental $c(x)/(c_s)$ curves of amorphous electron-beam evaporated WO$_3$ at four different moments in time and the corresponding theoretical curves with a fixed value of the mean value of the experimentally obtained diffusion coefficients $D = 1.3 \cdot 10^{-10}\,\mathrm{cm^2/s}$. (a) $t = 567\,\mathrm{s}$; (b) $t = 3019\,\mathrm{s}$; (c) $t = 5076\,\mathrm{s}$; (d) $t = 10023\,\mathrm{s}$.

To further illustrate the good agreement, the concentration curves are shown in a logarithmic representation in figure 3.47. Experimental and theoretical curves are still in accordance on this scale and agree well over an order of magnitude in concentration c. However, for t close to zero (the time when the external potential

was applied), theoretical and experimental curves are only in very good agreement for small values of x (close to the line). With increasing time the spatial range where both curves are in very good accordance increases. While for $t = 567\,\mathrm{s}$ the fit is in good agreement with the experimental curve for $x < 5\,\mu\mathrm{m}$, the fit for $t = 10023\,\mathrm{s}$ shows good accordance for $x < 30\,\mu\mathrm{m}$.
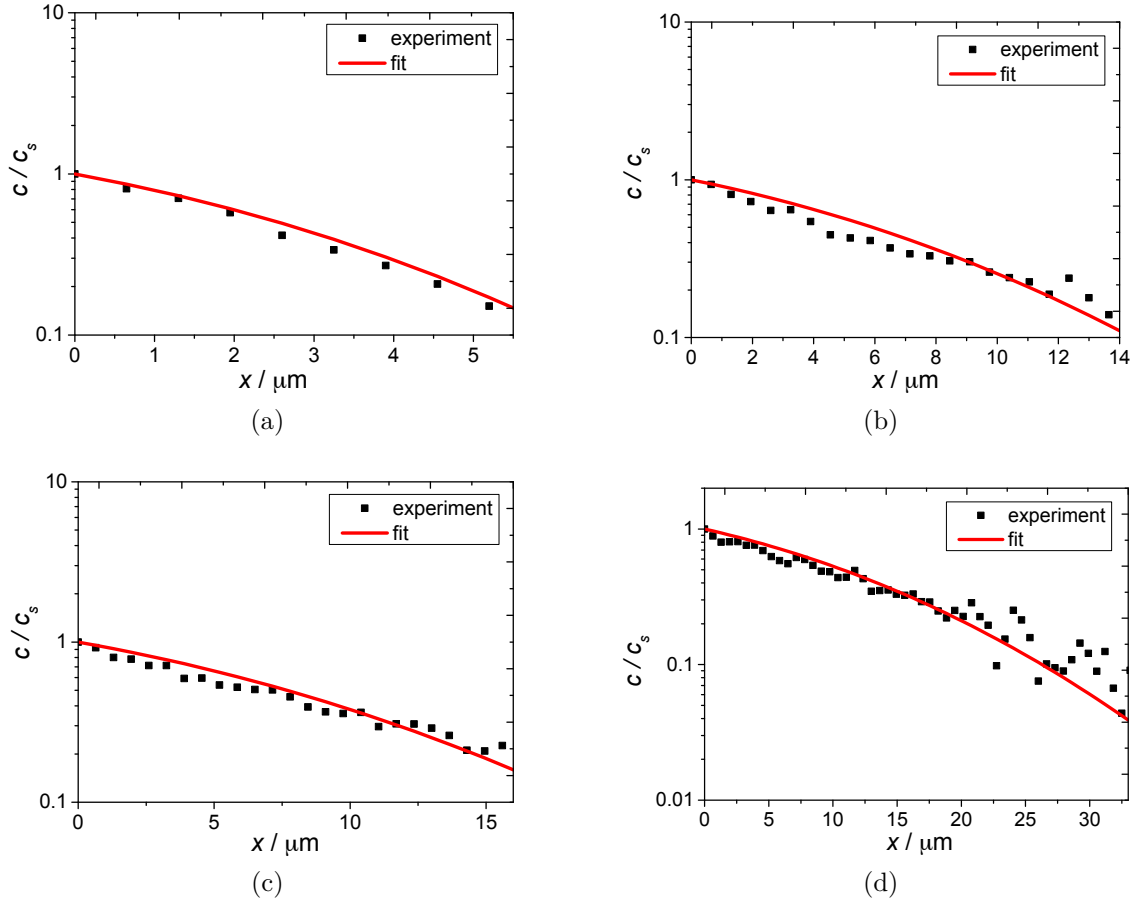
Figure 3.47: Logarithmic representation of experimental $c(x)/(c_s)$ curves of amorphous electron-beam evaporated WO_3 for four different values of diffusion times and the corresponding theoretical curves with a fixed value of of the arithmetic mean of the experimentally obtained diffusion coefficients $D = 1.3 \cdot 10^{-10}\,\mathrm{cm}^2/\mathrm{s}$. (a) $t = 567\,\mathrm{s}$; (b) $t = 3019\,\mathrm{s}$; (c) $t = 5076\,\mathrm{s}$; (d) $t = 10023\,\mathrm{s}$.

The determination of a diffusion coefficient inside crystalline WO$_3$ is not as straight forward as for amorphous WO$_3$. As shown in fig. 3.43(b) the assumption of a constant surface concentration (coloration inside the line not covered by PMMA) is not valid. The transmission decreases slowly in time and thus, assuming that Lambert-Beer's law is valid, the concentration increases with increasing time. Solutions of Fick's second law usually describe concentration sources that decrease in time, thus in order to find a solution for an increasing concentration source, a standard solution should be modified in order to fit this condition. Assuming that a fixed amount of ions is distributed throughout the area of the uncovered line pattern at $t = 0$, then in time these ions would diffuse into areas of the covered WO$_3$ sample and the concentration inside the line would decrease in time. However, with a constant potential applied to the sample, this situation is constantly repeated: the area of the line is inserted with ions which again diffuse throughout the sample. In order to create a solution that includes an increasing instead of a decreasing concentration source, the process of ion insertion into the area of the line structure should be included as a sum over time:

$$c(x) = \sum_{i=1}^{N} c^*(x, t - t_i), \tag{3.16}$$

where $c(x)$ is the resulting concentration profile consisting of concentration profiles $c^*(x, t - t_i)$ of an extended two-dimensional initial concentration distribution (area of the line inserted with ions) [78]:

$$c^*(x, t - t_i) = \frac{1}{2} \, n_i \, \mathrm{erf}\left(\frac{h - x}{2\sqrt{D(t - t_i)}}\right) + \mathrm{erf}\left(\frac{x + h}{2\sqrt{D(t - t_i)}}\right), t > t_i \tag{3.17}$$

with $c^*(x, t - t_i) = 0$ for $t < t_i$. c^* is an analytical solution of Fick's second law describing n_i particles starting to diffuse at $t = t_i$ and $c^*(x, t - t_i) = 0$ for $t < t_i$. n_i is set to be the difference of concentration c_i existing at time $t = t_i$ inside the uncovered line and the sum of all previous concentration profiles up to c^*_{i-1} at time $t = t_i$ and location $x = 0$:

$$n_i = c_i - \sum_{k=1}^{i-1} c^*_{i-k}(0, t_i - t_{i-k}) \tag{3.18}$$

Each summand c^*_{i-k} describes a concentration profile due to the insertion of ions into the uncovered line area of the sample and $c^*_{i-k}(0, t_i - t_{i-k})$ the concentration profile at time $t = t_i$.
With equations 3.16 to 3.18 it is possible to interpolate the measured concentration profile which can be converted into intensity profiles by using Lambert-Beer's law. For each measured intensity a value of c_i can be assigned, and together with prescribing a value for D one obtains the corresponding n_i. However, it should be

mentioned that one set of parameters D and n_i, that lead to a fit of $c(0,t)$, is not unique. A decent value of the diffusion coefficient D can only be obtained if the entire set of curves $c(x,t)$ can be fitted simultaneously.

Limitations of the experimental setup especially the detection system, which could cause errors in the experiment, are discussed exemplarily in the following.

A CCD image sensor is among others characterized by its quantum efficiency which describes the ratio of incident photons and the number of photons that are converted into corresponding electrons; its dynamic range which describes the ability to measure light/dark differences or in other words indicates the resolution of the intensity; and its linearity which describes the linearity of the ratio of incoming light and the corresponding signal output for different exposure times.

The quantum efficiency is a function of wavelength of the incoming light. However, all measurements were carried out at the same fixed band pass with the central wavelength at $\lambda_0 = 633\,\mathrm{nm}$, where the quantum efficiency of the CCD has a value of about 40%. The non-linearity of the sensor is indicated with a value <1% which is very good so that an error due to non-linearity is negligible as well. The dynamic range of 68 dB is also a very good value, however, in the measurements the intensity of the light that enters the CCD is very low. The source light is multiply decreased by several elements of the setup (optical fiber, electrochemical cell, mirrors and gratings etc.) until it enters the CCD. In order to better resolve the intensity of the light, the exposure time could be increased, a binning could be applied, or a more powerful light source could be employed in future experiments. Another improvement of the setup for the diffusion experiment maybe the use of a 633 nm laser to avoid the spectrometer.

Time resolved visualization of ion diffusion inside an electrochromic thin film was realized with the presented setup. Constraining the ion insertion to a restricted area with the help of a transparent resist allows for selective coloration related to diffusion of specific species. Analysis of the experimental data gained by the lateral diffusion experiments yielded a diffusion coefficient for hydrogen inside amorphous WO_3 thin films. The diffusion coefficient found for amorphous WO_3 with a value of $D = 1.3 \cdot 10^{-10}\,\mathrm{cm}^2/\mathrm{s}$ is in good agreement with values found in literature.

So far experiments usually employed for determining diffusion coefficients, e.g. impedance spectroscopy, give only indirect information about the transport processes inside solids. With the presented setup experiments could be conducted, which give direct information about the diffusion of the species responsible for coloration.

4 Conclusions and Outlook

The aim of this work was to design and build an experimental setup which combines electrochemical measurements with both, temporally and spatially resolved transmission spectroscopy. For this purpose, an optical microscope was combined with a subtractive double spectrometer, which acts as an optical bandpass, and a charge coupled device (CCD) camera, which allows one to obtain magnified images of the sample studied. The system was designed and successfully put into operation. Moreover, compact electrochemical cells for the spectro-electrochemical microscope were designed, constructed and used in the experiment. The combination of electrochemical cell and microscope system yields the possibility to conduct in situ transmission measurements during ion insertion into the thin film samples, which allow one to form a physical and an electrochemical analysis simultaneously. Finally, as a model system for electrochromic experiments WO_3 thin film electrodes were prepared and investigated. The main results of this Ph.D. thesis are depicted graphically in figure 4.1 and can be summarized as follows:

(a) Time resolved transmission experiments revealed that coloration is quicker than bleaching in amorphous WO_3. Coloration and bleaching in crystalline WO_3 is slower than in amorphous WO_3. The coloration of crystalline WO_3 efficiently takes place in a narrow region of electrode potential only, while coloration of amorphous WO_3 is efficient over a wide range of electrode potential. Another important difference of the crystalline samples compared to the amorphous films is the appearance of current peaks in cyclic voltammograms that correlate with the coloration efficiency of the thin film and only occur in crystalline samples.

(b) In a case study of nanocrystalline dip-coated WO_3 the correlation between the oxidation states of tungsten and its coloration efficiency was analyzed. Pristine WO_3 exhibits a tetragonal crystal structure and solely tungsten in a 6+ oxidation state. During coloration tungsten is electrochemically reduced, and the formation of W^{5+} can be proven and related to a first peak (at higher electrode potentials) in both, the CV and the differential capacity, dQ/dE, of a galvanostatic discharge curve. However, only the formation of W^{4+}, which takes place at the second reduction potential (at lower electrode potentials), comes along with a strong coloration. After the formation of W^{4+}, Li_xWO_3 exhibits a cubic crystal structure. Combining the spectro-electrochemical and

XPS analysis it was possible to show that both W^{5+} and W^{4+} are formed at different electrode potentials and that both species play a different role in the coloration process. In literature often either W^{5+} or W^{4+} is considered being responsible for the coloration.

(c) By patterning a transparent and insulating layer deposited on top of the WO_3 thin film, local insertion of hydrogen into the thin film was achieved and ion transport in the plane of the WO_3 film could be studied spatially resolved. Via the small area of the sample, which is not covered by the transparent layer, hydrogen may locally diffuse into the layer driven by the hydrogen concentration gradient. By temporally resolved imaging of the patterned WO_3 film, the diffusion profiles could be visualized as a function of time and spatial coordinate. This experiment is special in the sense that usually in diffusion experiments the concentration of the diffusant is measured either as a function of diffusion distance for a fixed time or as a function of time without spatial resolution. The combined analysis of the temporally and spatially resolved hydrogen diffusion yielded a diffusion coefficient for hydrogen in amorphous WO_3 thin films with a value of $D = 1.3 \cdot 10^{-10}\,\text{cm}^2/\text{s} \pm 0.3 \cdot 10^{-10}\,\text{cm}^2/\text{s}$.

The same experiment carried out on crystalline WO_3 shows a very different behavior, which makes the analysis for determining a diffusion coefficient more difficult. Still, it is important to note that this kind of lateral diffusion experiment reveals considerably more information than conventional transmission studies which can only yield integral values of transmission, i.e. it is averaged over regions of the sample containing different concentrations of ions. With the presented setup essentially each area on a sample inserted with ions can be studied separately.

In future experiments particularly, spatially resolved transmission experiments should be further pursued in the future, since to my knowledge, diffusion coefficients of ions inside solid WO_3 have never been directly determined. Merely indirect approaches, such as electrochemical impedance spectroscopy or galvanostatic intermittent titration, were employed to indirectly determine a diffusion coefficient by analyzing the electric responses of the system.

The presented setup is not only a powerful tool for investigating WO_3 thin films. Many substances employed for lithium batteries, such as LTO or LCO, exhibit electrochromic behavior and can be investigated by this novel approach in order to obtain a better understanding of their transport properties. In addition it would be highly desirable to follow in operando both optical and structural changes (e.g. by XRD or Raman) during electrochemical experiments. It may also be of interest to perform in situ XPS studies with electrochemical lithiation of WO_3 using solid or ionic liquid based electrolytes.

(a) Time resolved spectro-electrochemistry

amorphous   crystalline

CV   CV

dT/dE

electrode potential

(b) Coloration efficiency, oxidation state and crystal structure

electrode potential

differentielle capacity

C

T

T

$W^{5+} \longleftarrow W^{6+}$

$W^{4+} \longleftarrow W^{x+}$

(c) Spatially resolved hydrogen diffusion in WO$_3$

time

$D = 1.3 \cdot 10^{-8}$ cm^2/s

concentration

distance
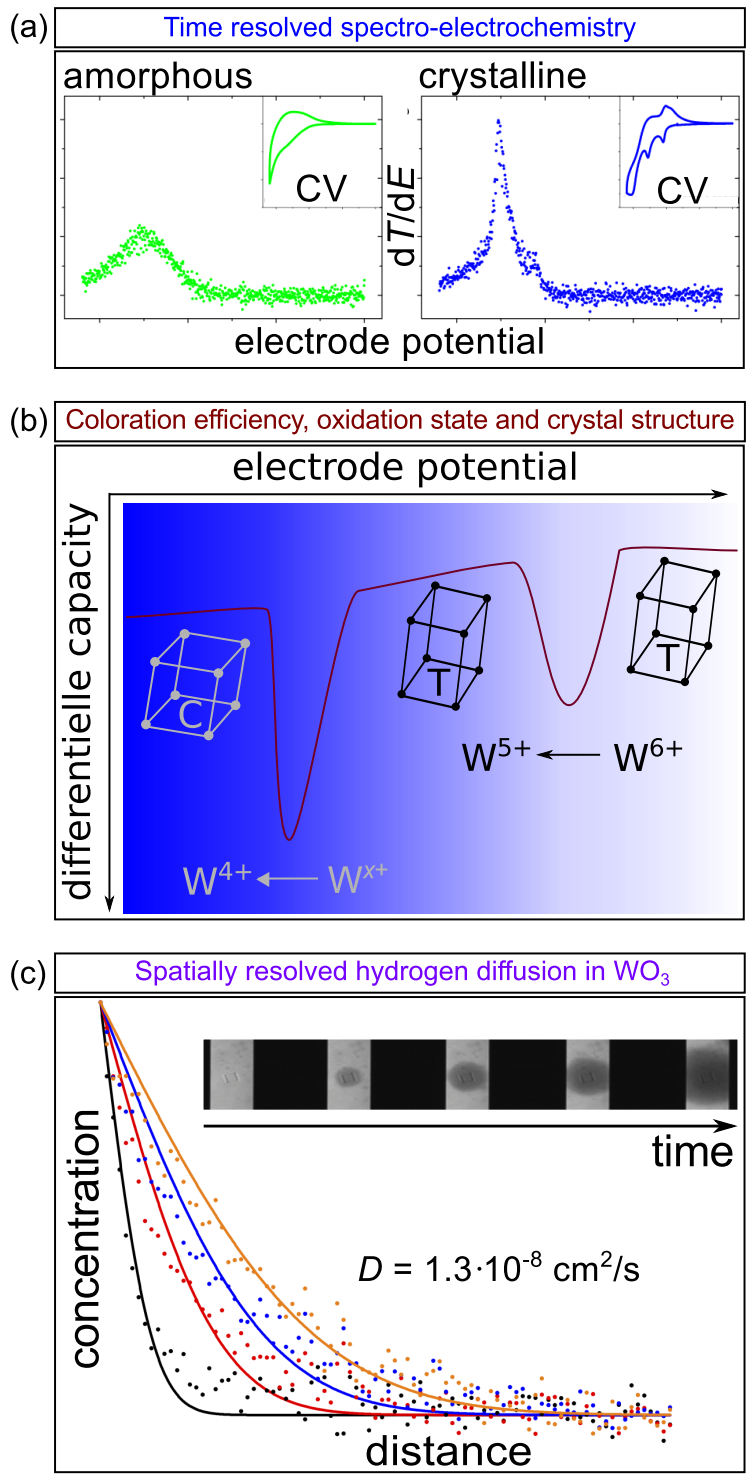
Figure 4.1: Main results obtained with the experimental setup developed in this thesis: (a) time resolved ion insertion, (b) correlation of tungsten oxidation states with the coloration efficiency, and (c) spatially resolved ion diffusion.

Bibliography

[1] G. A. Niklasson, L. Berggren, and A.-L. Larsson. Electrochromic tungsten oxide: the role of defects. *Sol. Energ. Mat. Sol. C.*, 84(1–4):315 – 328, 2004.

[2] K. Bange. Colouration of tungsten oxide films: A model for optically active coatings. *Sol. Energ. Mat. Sol. C.*, 58(1):1 – 131, 1999.

[3] C. G. Granqvist. Oxide electrochromics: An introduction to devices and materials. *Sol. Energ. Mat. Sol. C.*, 99:1 – 13, 2012.

[4] S. K. Deb. A novel electrophotographic system. *Appl. Optics Suppl.*, 3:192 – 195, 1969.

[5] C. M. Lampert. Electrochromic materials and devices for energy efficient windows. *Sol. Energ. Mater.*, 11(1–2):1 – 27, 1984.

[6] J. S. E. M. Svensson and C. G. Granqvist. Electrochromic tungsten oxide films for energy efficient windows. *Sol. Energ. Mater.*, 11(1–2):29 – 34, 1984.

[7] C. G. Granqvist. Electrochromic tungsten oxide films: Review of progress 1993–1998. *Sol. Energ. Mat. Sol. C.*, 60(3):201 – 262, 2000.

[8] P. M. S. Monk. Charge Movement through Electrochromic Thin-Film Tungsten Trioxide. *Crit. Rev. Solid State*, 24:193–226, 1999.

[9] C. G. Granqvist. *Handbook of Inorganic Electrochromic Materials.* Elsevier, 1995. ISBN 9780444899309.

[10] T. Tesfamichael, M. Arita, T. Bostrom, and J. Bell. Thin film deposition and characterization of pure and iron-doped electron-beam evaporated tungsten oxide for gas sensors. *Thin Solid Films*, 518(17):4791 – 4797, 2010.

[11] D. R. Rosseinsky and R. J. Mortimer. Electrochromic systems and the prospects for devices. *Adv. Mater.*, 13(11):783–793, 2001.

[12] D. T. Gillaspie, R. C. Tenent, and A. C. Dillon. Metal-oxide films for electrochromic applications: present technology and future directions. *J. Mater. Chem.*, 20:9585–9592, 2010.

[13] S. Tanisaki. Crystal structure of monoclinic tungsten trioxide at room temperature. *J. Phys. Soc. Jpn.*, 15(4):573–581, 1960.

[14] E. K. H. Salje, S. Rehmann, F. Pobell, D. Morris, K. S. Knight, T. Herrmannsdorfer, and M. T. Dove. Crystal structure and paramagnetic behaviour of ϵ WO_{3-x}. *J. Phys.-Condens. Mat.*, 9(31):6563, 1997.

[15] R. Diehl, G. Brandt, and E. Salje. The crystal structure of triclinic WO_3. *Acta Crystallogr. B*, 34:1105 – 1111, 1978.

[16] E. Salje. The orthorhombic phase of WO_3. *Acta Crystallogr. B*, 33(2):574 – 577, 1977.

[17] W. L. Kehl, R. G. Hay, and D. Wahl. The structure of tetragonal tungsten trioxide. *J. Appl. Phys.*, 23(2):212 – 215, 1952.

[18] A.F. Holleman, E. Wiberg, and N. Wiberg. *Lehrbuch der anorganischen Chemie*, volume 102. Walter de Gruyter, 2007. ISBN 9783110177701.

[19] Q. Zhong, J. R. Dahn, and K. Colbow. Lithium intercalation into WO_3 and the phase diagram of Li_xWO_3. *Phys. Rev. B*, 46:2554–2560, 1992.

[20] C.H. Hamann and W. Vielstich. *Elektrochemie*. Wiley-VCH-Verlag, 2005. ISBN 9783527310685.

[21] A. J. Bard and L. R. Faulkner. *Electrochemical Methods: Fundamentals and Applications*. Wiley, 2000. ISBN 9780471043720.

[22] R. A. Huggins. *Advanced Batteries: Materials Science Aspects*. Springer, 2008.

[23] P. M. S. Monk, R. J. Mortimer, and D. R. Rosseinsky. *Electrochromism: Fundamentals and Applications*. Wiley, 2008.

[24] O. F. Schirmer and E. Salje. The W^{5+} polaron in crystalline low temperature WO_3 ESR and optical absorption. *Solid State Commun.*, 33(3):333 – 336, 1980.

[25] S.-H. Lee, M. J. Seong, H. M. Cheong, E. Ozkan, E. C. Tracy, and S. K. Deb. Effect of crystallinity on electrochromic mechanism of Li_xWO_3 thin films. *Solid State Ionics*, 156(3-4):447 – 452, 2003.

[26] O. F. Schirmer, V. Wittwer, G. Baur, and G. Brandt. Dependence on wo₃ electrochromic absorption on crystallinity. *J. Electrochem. Soc.*, 124:749 – 753, 1977.

[27] A.-L. Larsson, B. E. Sernelius, and G. A. Niklasson. Optical absorption of li-intercalated polycrystalline tungsten oxide films: comparison to large polaron theory. *Solid State Ionics*, 165(1–4):35 – 41, 2003.

[28] F. Wooten. *Optical Properties of Solids*. Academic Press: New York and London, 2013. ISBN 9781483220765.

[29] H. Kamal, A. A. Akl, and K. Abdel-Hady. Influence of proton insertion on the conductivity, structural and optical properties of amorphous and crystalline electrochromic WO_3 films. *Physica B*, 349(1–4):192 – 205, 2004.

[30] E. Gerlach. Carrier scattering and transport in semiconductors treated by the energy-loss method. *J. Phys. Part C Solid*, 19(24):4585, 1986.

[31] J.-G. Zhang, D. K. Benson, C. E. Tracy, S. K. Deb, A. W. Czanderna, and C. Bechinger. Chromic mechanism in amorphous wo_3 films. *J. Electrochem. Soc.*, 144(6):2022 – 2026, 1997.

[32] O. F. Schirmer and E. Salje. Conduction bipolarons in low-temperature crystalline wo_{3-x}. *J. Phys. C: Solid St. Phys.*, 13:L1067–72, 1980.

[33] E. Broclawik, A. Gora, P. Liguzinski, P. Petelenz, and H. A. Witek. Quantum chemical modeling of electrochromism of tungsten oxide films. *J. Chem. Phys*, 124(5), 2006.

[34] M. V. Limaye, J. S. Chen, S. B. Singh, Y. C. Shao, Y. F. Wang, C. W. Pao, H. M. Tsai, J. F. Lee, H. J. Lin, J. W. Chiou, M. C. Yang, W. T. Wu, J. S. Chen, J. J. Wu, M. H. Tsai, and W. F. Pong. Correlation between electrochromism and electronic structures of tungsten oxide films. *RSC Adv.*, 4:5036–5045, 2014.

[35] G. Grimvall. On rigid bands and mass enhancements in noble metal alloys. *Phys. Kondens. Mater.*, 14(2):101–104, 1972.

[36] B. Chen, J. Laverock, L. F. J Piper, A. R. H. Preston, S. W. Cho, A. DeMasi, K. E. Smith, D. O Scanlon, G. W. Watson, R. G. Egdell, P.-A. Glans, and J.-H. Guo. The band structure of WO_3 and non-rigid-band behaviour in $Na_{0.67}$ WO_3 derived from soft x-ray spectroscopy and density functional theory. *J. Phys.-Condens. Mat.*, 25(16):165501, 2013.

[37] R. J. D. Tilley. *Defects in Solids*. Special Topics in Inorganic Chemistry. Wiley, 2008.

[38] H. Mehrer. *Diffusion in Solids: Fundamentals, Methods, Materials, Diffusion Controlled Processes*. Springer Series in Solid-State Sciences. Springer, 2007.

[39] A. Fick. Über Diffusion. *Ann. Phys. und Chem.*, 94:59, 1855.

[40] M. S. Mattsson. Li insertion into WO_3: introduction of a new electrochemical analysis method and comparison with impedance spectroscopy and the galvanostatic intermittent titration technique. *Solid State Ionics*, 131:261 – 273, 2000.

[41] C. Ho, I. D. Raistrick, and R. A. Huggins. Application of ac techniques to the study of lithium diffusion in tungsten trioxide thin films. *J. Electrochem. Soc.*, 127(2):343 – 350, 1980.

[42] W. Weppner and R. A. Huggins. Electrochemical method for determining both kinetic and thermodynamic properties of mixed conducting solids with high diffusion rates. *J. Electrochemical Soc.*, 124:1569, 1977.

[43] C. J. Wen and Robert A. Huggins. Electrochemical investigation of the lithium gallium system. *J. Electrochem. Soc.*, 128(8):1636 – 1641, 1981.

[44] J.-P. Randin and R. Viennet. Proton diffusion in tungsten trioxide thin films. *J. Electrochem. Soc.*, 129(10):2349 – 2354, 1982.

[45] B. Reichman, A. J. Bard, and D. Laser. A Digital Simulation Model for Electrochromic Processes at WO_3 Electrodes. *J. Electrochem. Soc.*, 127(3):647 – 654, 1980.

[46] O. Bohnke, M. Rezrazi, B. Vuillemin, C. Bohnke, P.A. Gillet, and C. Rousselot. In situ optical electrochemical characterization of electrochromic phenomena into tungsten trioxide thin films. *Sol. Energ. Mat. Sol. C.*, 25(3–4):361 – 374, 1992.

[47] F: Berkemeier, T. Stockhoff, T. Gallasch, and G. Schmitz. Volume diffusion and interface transport in $LiCoO_2$ measured by electrochromic absorption. *Acta Mater.*, 80:132 – 140, 2014.

[48] B. Speiser. Elektroanalytische methoden ii: Cyclische voltammetrie. *Chemie unserer Zeit*, 15(2), 1981.

[49] M. D. Levi, G. Salitra, B. Markovsky, H. Teller, D. Aurbach, U. Heider, and L. Heider. Solid-State Electrochemical Kinetics of Li-Ion Intercalation into $Li_{1-x}CoO_2$: Simultaneous Application of Electroanalytical Techniques SSCV, PITT, and EIS. *J. Electrochem. Soc.*, 146(4):1279 – 1289, 1999.

[50] L. Smart and E. Moore. *Einführung in die Festkörperchemie*. Vieweg, 1997.

[51] J. Livage and D. Ganguli. Sol-gel electrochromic coatings and devices: A review. *Sol. Energ. Mat. Sol. C.*, 68(3–4):365 – 381, 2001.

[52] J. Wallys, J. Teubert, F. Furtmayr, D. M. Hofmann, and M. Eickhoff. Bias-Enhanced Optical pH Response of Group III-Nitride Nanowires. *Nano Lett.*, 12(12):6180 – 6186, 2012.

[53] URL `www.pineinst.com`.

[54] URL `www.renishaw.de`.

[55] R. Chatten, A. V. Chadwick, A. Rougier, and P. J. D. Lindan. The Oxygen Vacancy in Crystal Phases of WO_3. *J. Phys. Chem. B*, 109(8):3146 – 3156, 2005.

[56] R. Sivakumar, R. Gopalakrishnan, M. Jayachandran, and C. Sanjeeviraja. Preparation and characterization of electron beam evaporated WO_3 thin films. *Opt. Mater.*, 29(6):679 – 687, 2007.

[57] M. G. Hutchins, O. Abu-Alkhair, M. M. El-Nahass, and K. Abd El-Hady. Structural and optical characterisation of thermally evaporated tungsten trioxide (WO_3) thin films. *Mater. Chem. Phys.*, 98(2–3):401 – 405, 2006.

[58] B. O. Loopstra and H. M. Rietveld. Further refinement of the structure of WO_3. *Acta Crystallogr. B*, 25(7):1420 – 1421, 1969.

[59] P. Hartmann, T. Leichtweiss, M. R. Busche, M. Schneider, M. Reich, J. Sann, P Adelhelm, and J Janek. Degradation of NASICON-Type Materials in Contact with Lithium Metal: Formation of Mixed Conducting Interphases (MCI) on Solid Electrolytes. *J. Phys. Chem. C*, 117(41):21064 – 21074, 2013.

[60] S. Wenzel, T. Leichtweiss, D. Krüger, J. Sann, and J. Janek. Interphase formation on lithium solid electrolytes – An in situ approach to study interfacial reactions by photoelectron spectroscopy. *ACS Appl. Mater. Interfaces*, submitted.

[61] F.Y. Xie, L. Gong, X. Liu, Y.T. Tao, W.H. Zhang, S.H. Chen, H. Meng, and J. Chen. XPS studies on surface reduction of tungsten oxide nanowire film by Ar^+ bombardment. *J. Electron Spectroscop.*, 185(3–4):112 – 118, 2012.

[62] J. C. Dupin, D. Gonbeau, I Martin-Litas, P. Vinatier, and A. Levasseur. Lithium intercalation/deintercalation in transition metal oxides investigated by x-ray photoelectron spectroscopy. *J. Electron Spectroscop.*, 120(1-3):55 – 65, 2001.

[63] A: Romanyuk and P. Oelhafen. Evidence of different oxygen states during thermal coloration of tungsten oxide. *Sol. Energ. Mat. Sol. C.*, 90(13):1945 – 1950, 2006.

[64] M. Stolze, B. Camin, F. Galbert, U. Reinholz, and L. K. Thomas. Nature of substoichiometry in reactively dc-sputtered tungsten oxide thin films and its effect on the maximum obtainable colouration by gases. *Thin Solid Films*, 409 (2):254 – 264, 2002.

[65] L. Su and Z. Lu. All solid state smart window of electrodeposited WO_3 and TiO_2 particulate film with PTREFG gel electrolyte. *J. Phys. and Chem. Solids*, 59(8):1175 – 1180, 1998.

[66] A. Henningsson, A. Stashans, A. Sandell, H. Rensmo, S. Södergren, H. Lindström, L. Vayssieres, A. Hagfeldt, S. Lunell, and H. Siegbahn. Proton Insertion in Polycrystalline WO_3 Studied with Electron Spectroscopy and Semi-empirical Calculations. 47:23 – 36, 2004.

[67] A. Siokou, S. Ntais, S. Papaefthimiou, G. Leftheriotis, and P. Yianoulis. Influence of the substrate on the electrochromic characteristics of lithiated α-wo$_3$ layers. *Surf. Sci.*, 566–568, Part 2(0):1168 – 1173, 2004.

[68] V. Wittwer, O.F. Schirmer, and P. Schlotter. Disorder dependence and optical detection of the Anderson transition in amorphous $H_x WO_3$ bronzes. *Solid State Commun.*, 25(12):977 – 980, 1978.

[69] S. K. Deb. Opportunities and challenges in science and technology of wo$_3$ for electrochromic and related applications. *Solar Energy Materials and Solar Cells*, 92(2):245 – 258, 2008.

[70] S.-H. Lee, H. M. Cheong, E. C. Tracy, A. Mascarenhas, A. W. Czanderna, and S. K. Deb. Electrochromic coloration efficiency of a-WO_{3-y} thin films as a function of oxygen deficiency. *Appl. Phys. Lett.*, 75(11):1541–1543, 1999.

[71] T. Brezesinski, D. Fattakhova Rohlfing, S. Sallard, M. Antoniettie, and B. M. Smarsly. Highly Crystalline WO_3 Thin Films with Ordered 3D Mesoporosity and Improved Electrochromic Performance. *Small*, 2(10):1203–1211, 2006.

[72] P. Baudry, M. A. Aegerter, D. Derod, and B. Valla. Electrochromic window with lithium conductive polymer electrolyte. *J. Electrochem. Soc.*, 138(2):460 – 465, 1991.

[73] S.-H. Lee, J.-G. Zhang H. M. Cheong, A. Mascarenhas, D. K. Benson, and S. K. Deb. Electrochromic mechanism in a-WO_{3-y} thin films. *J. Appl. Phys.*, 74(2): 242 – 244, 1999.

[74] Se-Hee Lee, Hyeonsik M Cheong, C.Edwin Tracy, Angelo Mascarenhas, David K Benson, and Satyen K Deb. Raman spectroscopic studies of electrochromic a-WO_3. *Electrochim. Acta*, 44(18):3111 – 3115, 1999.

[75] G. Girishkumar, B. McCloskey, A. C. Luntz, S. Swanson, and W. Wilcke. Lithium-air battery: Promise and challenges. *J. Phys. Chem. Lett.*, 1(14): 2193 – 2203, 2010.

[76] Y.-C. Lu, E. J. Crumlin, G. M. Veith, J. R. Harding, E. Mutoro, L. Baggetto, N. J. Dudney, Z. Liu, and Y. Shao-Horn. In Situ Ambient Pressure X-ray Photoelectron Spectroscopy Studies of Lithium-Oxygen Redox Reactions. *Sci. Reports*, 2, 2012.

[77] R. S. Crandall and B. W. Faughnan. Electronic Transport in Amorphous H_xWO_3. *Phys. Rev. Lett.*, 39:232–235, 1977.

[78] J. Crank. *The Mathematics of Diffusion.* Oxford University Press, 1975.

Declaration

Ich erkläre: Ich habe die vorgelegte Dissertation selbständig und ohne unerlaubte fremde Hilfe und nur mit den Hilfen angefertigt, die ich in der Dissertation angegeben habe. Alle Textstellen, die wörtlich oder sinngemäß aus veröffentlichten Schriften entnommen sind, und alle Angaben, die auf mündlichen Auskünften beruhen, sind als solche kenntlich gemacht. Bei den von mir durchgeführten und in der Dissertation erwähnten Untersuchungen habe ich die Grundsätze guter wissenschaftlicher Praxis, wie sie in der „Satzung der Justus-Liebig-Universität Gießen zur Sicherung guter wissenschaftlicher Praxis" niedergelegt sind, eingehalten.

Gießen, 28. Juli 2015

....
Sabrina Darmawi